

UNIVERSITY OF PUERTO RICO  
RIO PIEDRAS CAMPUS  
COLLEGE OF NATURAL SCIENCES, CHEMISTRY DEPARTMENT

**THE POTENTIAL OF NATURAL POLYSACCHARIDES: CHEMICAL  
APPROACHES FOR BONE TISSUE REGENERATION**

By: Simara Laboy López

A thesis submitted to complete the requirements for the  
degree of Doctor of Philosophy, Ph.D

November 16 , 2021

**Accepted by the Faculty of the Department of Chemistry of the  
University of Puerto Rico – Río Piedras Campus, in Partial Fulfillment  
of the Requirements for the Degree of Ph.D. in Chemistry**

Examining Committee Members

Eduardo Nicolau López, Ph.D.

Professor of Chemistry

University of Puerto Rico, Río Piedras \_\_\_\_\_

Thesis Advisor

Liz Díaz, Ph.D.

Professor of Chemistry

University of Puerto Rico, Río Piedras \_\_\_\_\_

Thesis Committee Member

Kai Griebenow, Ph.D.

Professor of Chemistry

University of Puerto Rico, Río Piedras \_\_\_\_\_

Thesis Committee Member

Marvin Bayro, Ph.D.

Associate Professor of Chemistry

University of Puerto Rico, Río Piedras \_\_\_\_\_

Thesis Committee Member

*To my mom:*

*This was inspired, pursued, and achieved thanks to you*

*To my future self:*

*It took you too long to understand that doing everything alone  
will not necessarily bring you a sense of accomplishment.  
Don't be afraid to encounter setbacks in your future; problems  
exist to create courage and increase wisdom. You can do  
everything you set your mind to, just not all at once.*

*Remember goals are dreams with deadlines that can be  
achieved by breaking up Specific Aims into individual tasks.*

## AKNOWLEDGEMENTS

There are many people in my surroundings who helped me make this achievement possible. In the first place, I must thank my parents Norma López and Rafael Rivera, for simply being there, providing me their guidance and caring for my wellbeing; they both kept pushing me and motivating me every time I felt like quitting by reminding me that it would be worth it. My mom played a big role in this pursuit by being an inspiration to me as, she too, pursued a scientific PhD in a time where access to information was limited; and, in a country whose language was not native to her.

I wish to thank undergraduate students Claudia Herdocia, Cristina Rivera, Jorge Padilla and specifically Pedro Mendez with whom I worked with for many years. My no longer colleagues, but friends, Dr. Camila Morales-Navas, Dr. Annelis Sánchez, Dr. Perla Cruz-Tato, Dr. Luis Betancourt, and Keila Rentas-Centeno, Pharm.D. were crucial in my career pursuit and in helping me see that, even if I didn't recognize it or believe it, I had the potential to become a doctor in Science; I wouldn't have come this far without their support and advice. I want to thank the female role models who played a part in helping me feel like I was welcome and belonged in the Chemistry Graduate Program such as Dr. Liz Diaz, Dr. Dalice Piñero, Dr. Giovanna Guerrero and Dr. Monica Feliú.

Most importantly, I want to thank Dr. Eduardo Nicolau for allowing me to become part of his research team while lacking previous research experience and not being aware at that time what I had gotten myself into. I wish to thank him for his patience in dealing with such an atypical student who didn't fit within the academic graduate student stereotype that is usually expected in this field. He has served me as an excellent example of professionalism approaching difficult or complicated situations. As I kept learning about

different topics, with which I could easily become excited and imagine changing the world in some possible way, he never discouraged me from discarding an idea and always expressed a positive attitude towards branching out and accumulating more knowledge from different fields. For that and much more, I am incredibly grateful.

I wish to thank the Materials Characterization Center (MCC) for their friendliness and availability to provide us with services involving the use of the Scanning Electron Microscope and Attenuated Total Diffraction Fourier Transform Infrared Spectrometer. Also, I wish to thank Lic. Bismark Madera for his disposition and confocal microscopy services received from the Neuroimaging and Electrophysiology Facility (NIEF). I wish to acknowledge the services received from Dr. José Hernandez regarding the X-Ray Photoelectron Spectroscopy measurements and his training regarding the use of several equipments.

## ABSTRACT

There are approximately 44 million people in the United States alone who suffer from diseases that cause bone density loss; and as life expectancy increases, so do the probabilities of being inflicted with such diseases. In the last decades, cell-based approaches for bone tissue engineering, have relied on using models that fail to reproduce either the complexity of the bone 3D microenvironment or the nanoscale characteristics of mineralized bone collagen. In this work three different biopolymers, fabricated with distinct methodologies are evaluated as potential scaffolds to aid in bone tissue regeneration (BTR) were explored.

First, an organic - inorganic coordination approach was realized using Sodium Alginate (NaAlg) and Iron III. Second, an organic - biological approach was achieved using Cellulose Acetate (CA) and bioactive peptides. And third, an inorganic - organic approach was performed using Hydroxyapatite (HAp) and Cellulose Nanocrystal (CNC) biopolymer. The first and second approaches were completed using the electrospinning (ES) technique while the third approach was done using a sol-gel technique. The biomaterials created were characterized using Atomic Force Microscopy (AFM), Scanning Electron Microscopy (SEM), Fourier Transform Infrared Spectroscopy (FTIR), X-Ray Photoelectron Spectroscopy (XPS), X-Ray Diffraction (XRD), Thermogravimetric Analysis (TGA), Dynamic Light Scattering (DLS) and Zeta Potential. The biological evaluation of the prepared scaffolds was assessed using Immunocytochemical (ICC) and Viability assays. Between the three explored approaches, the organic-biological approach showed the most potential to favor natural osteoblastic responses required for osseointegration.

## TABLE OF CONTENTS

<b>LIST OF FIGURES</b> .....	viii
<b>LIST OF SCHEMES</b> .....	xii
<b>LIST OF TABLES</b> .....	xiii
<b>LIST OF ABBREVIATIONS</b> .....	xiv
<b>BIOGRAPHICAL SKETCH</b> .....	xvi
<b>CHAPTER 1:INTRODUCTION</b> .....	1
1.1. Bone Chemical Composition .....	1
1.2. Bone Remodeling and Regulation Mechanism .....	1
1.3. Treatments for Bone Disorders .....	3
1.3.1. Autograft .....	4
1.3.2. Allograft .....	4
1.3.3. Xenograft .....	5
1.3.4. Cellular-based Graft .....	5
1.4. Scaffolds .....	5
1.4.1. Adhesion .....	6
1.4.2. Biopolymers in Scaffold Development .....	7
1.5. Hypothesis .....	10
1.6. Other Biopolymer Applications .....	10
<b>CHAPTER 2: METHODOLOGY AND TECHNIQUES</b>	

2.1.	Atomic Force Microscopy (AFM) . . . . .	12
2.2.	Electrospinning . . . . .	12
2.3.	Fourier Transform Infrared Spectroscopy (FTIR) . . . . .	12
2.4.	Ultraviolet Visible Spectroscopy (UV) . . . . .	13
2.5.	Freeze Dryer . . . . .	13
2.6.	X-ray Photoelectron Spectroscopy (XPS). . . . .	14
2.7.	X-Ray Diffraction (XRD). . . . .	14
2.8.	Thermogravimetric Analysis (TGA) . . . . .	14
2.9.	Cell Culture. . . . .	15
2.10.	Cell Immunocytochemical Assays . . . . .	15
2.11.	Cell Dehydration for SEM . . . . .	15
2.12.	Viability Assays . . . . .	16
 <b>CHAPTER 3: ALGINATE MEMBRANES FOR POLYPHENOL RECOVERY . .</b>		<b>17</b>
3.1.	Alginate-PEG Membranes by Casting Procedure . . . . .	20
3.1.1.	Atomic Force Microscopy (AFM) . . . . .	21
3.1.2.	Scanning Electron Microscopy (SEM) . . . . .	21
3.2.	Alginate-PEO Membranes by Electrospinning . . . . .	23
3.2.1.	Catechol Adsorption . . . . .	24
3.2.2.	Physical Characterization . . . . .	25
3.2.3.	Chemical Characterization . . . . .	27
3.2.4.	GC-MS Analysis of Environmental Samples . . . . .	29
3.2.5.	Catechol Bioactivity . . . . .	31



<b>CHAPTER 4: PEPTIDE COUPLED CELLULOSE ACETATE MATS AS BIOACTIVE SCAFFOLDS</b> .....	<b>38</b>
4.1. Synthesis of Cellulose Acetate Electrospun Fiber Mat .....	41
4.2. Functionalization of Cellulose Acetate Electrospun Membrane .....	41
4.2.1. Deacetylation .....	41
4.2.2. TEMPO Mediated Oxidation .....	42
4.2.3. Carbodiimide Crosslinking Chemistry .....	45
4.3. Characterization .....	46
4.3.1. Fourier Transform Infrared Spectroscopy (FTIR) .....	46
4.3.2. Scanning Electron Microscopy (SEM) .....	48
4.3.3. Thermogravimetric Analysis .....	50
4.4. Biological Assays .....	51
4.4.1. Expression of $\alpha_v\beta_3$ integrin receptor .....	51
4.4.1.1. Flow Cytometry (FC) .....	51
4.4.1.2. Microscopy Images of the $\alpha_v\beta_3$ Integrin Receptor .....	54
4.4.2. BrdU Proliferation Assessment .....	60
4.4.3. Maturation Assessments .....	63
4.4.3.1. Collagen Expression .....	63
4.4.3.2. Bone Sialoprotein (BSP) .....	64
4.4.4. Cellular Morphologic Assessment .....	68
<b>CHAPTER 5: CELLULOSE NANOCRYSTALS AS HAp MATRIX</b> .....	<b>74</b>
5.1. Composite Fabrication .....	77
5.1.1. TGA .....	78

5.1.2.	X-Ray Diffraction (XRD) . . . . .	79
5.1.3.	Fourier Transform Infrared Spectroscopy (FT-IR) . . . . .	80
5.1.4.	Dynamic Light Scattering (DLS) . . . . .	81
5.1.5.	SEM . . . . .	82
5.2.	Inclusion of BMP-2 to nHAp . . . . .	83
5.2.1.	DLS . . . . .	83
5.2.2.	Zeta Potential . . . . .	84
5.2.3.	Biocompatibility of Composites with Bone Progenitor Cells . . . . .	85
5.3.	CNC biopolymer potential . . . . .	86
5.3.1.	SEM . . . . .	86
5.3.2.	BrdU Proliferation Assay . . . . .	88
5.3.3.	MTS Cell Viability Assay . . . . .	91
	<b>CHAPTER 6: GENERAL CONCLUSIONS . . . . .</b>	<b>94</b>
	<b>APPENDIX I: SCIENCE COMMUNICATION . . . . .</b>	<b>97</b>
	<b>REFERENCES . . . . .</b>	<b>100</b>

## LIST OF FIGURES

**Figure 3.1** AFM image of Sodium Alginate Membrane prepared with PEG (a) 400 Mw and (b) 6000 Mw

**Figure 3.2** SEM Images of CaCl<sub>2</sub> Crosslinked Sodium Alginate Membrane Using (a) 1.5% and (b) 2.5% (w/v)

**Figure 3.3.** Pictures of the Alginate Formulations and Effect on Catechol Solution

**Figure 3.4** Calculated Catechol Concentration from Measured Absorbance at 275.5 nm before and after Incubation Periods of 4 and 24 hours.

**Figure 3.5** AFM Images of Electrospun Alg:PEO Membranes

**Figure 3.6** SEM Images of Top Membrane Surface and Internal Morphology of Alg and its Subsequent Reactions

**Figure 3.7** EDS Spectrum of AlgFeCat Surface Sphere

**Figure 3.8** FTIR of Alg (black), AlgFe (orange) and AlgFeCat (turquoise) Membranes

**Figure 3.9** XPS Spectrums for Alg Membranes After Reactions

**Figure 3.10** Gas Chromatogram of Field Water Samples Collected

**Figure 3.11** Vinculin Expression of hFOB 1.19 in Alginate Membranes. Scale Bar represents 50 μm.

**Figure 3.12** MTT Assay of Catechol Cytotoxicity. Statistically Accepted Values Between Asterisk Bracket

**Figure 4.1** FTIR of CA Fiber Mat (black) Deacetylation (red) and Oxidation (blue) Modifications

**Figure 4.2** SEM Images and Fiber Size Histograms of CA with Deacetylated and Oxidized Modifications

**Figure 4.3** FTIR spectra comparison of the (A) Individual Peptide Couplings KRSR (pink), RGD (olive), BMP-2 (orange) and d) Multipetide Coupling (dark yellow); and (B) Deconvoluted amide (purple) peaks using a Gaussian curve fitting function for CA-KRSR (pink), CA-RGD (olive) and CA-BMP-2 (orange).

**Figure 4.4** a) SEM Images and b) Fiber Size Histograms of Peptide Couplings

**Figure 4.5** a) TGA and b) DSC of CA (black) Deacetylated CA (red), Oxidized CA (blue), CA-KRSR (pink), CA-RGD (olive) and CA-BMP-2 (orange)

**Figure 4.6** Flow Cytometry of hFOB 1.19 a) Population Chosen, b) Control Fluorescence, c) Antibody Fluorescence, d) Untreated Control, e) Secondary Only Control and f) Antibody Treated Cells

**Figure 4.7**  $\alpha_v\beta_3$  integrin expression (green) in hFOB 1.19 (blue nuclei) across each CA electrospun mat (a) CA Fiber Mat, (b) CA-KRSR, (c) CA-RGD, (d) CA-BMP-2, and (e) CA-MP. Scale bar represents 50  $\mu\text{m}$ .

**Figure 4.8** Fluorescence Intensity Across Fiber Mat Treatments Normalized by the Total Cells Displayed Over Each Column Respectively.

**Figure 4.9** hFOB 1.19 BrdU cell proliferation assay against each CA electrospun mat. Blue nuclei represent total cells and orange overlaps represents the BrdU incorporated nuclei in

(a) CA Fiber Mat, (b) CA - KRSR, (c) CA - RGD, (d) CA –BMP-2and (e) CA-MP. Scale bar represents 50  $\mu\text{m}$ .

**Figure 4.10** a) Percentage of BrdU Positive Cells in each Fiber Mat Treatment and b) Total Number of Cells Present in each Fiber Mat Treatment

**Figure 4.11** Collagen I (green) assay for hFOB 1.19 (blue nuclei) across each CA electrospun mat (a) CA Fiber Mat, (b) CA - KRSR, (c) CA - RGD, (d) CA – BMP-2. Scale Bar Represents 50  $\mu\text{m}$ .

**Figure 4.12** hFOB 1.19 Expression of Collagen I (green) in a) Positive Disc Control, b) CA + KRSR, c) CA + RGD, d) CA + BMP-2 and e) CA + MP in DMEM. Scale bar represents 50  $\mu\text{m}$

**Figure 4.13** Alexa Fluor 488 Fluorescence Intensity plot normalized by the number of cells for collagen expression. Error bars represent the standard error of the mean.

**Figure 4.14** Microscopy Images for Bone Sialoprotein (BSP) Expression (green) across Fiber Mat treatments. Scale Bar Represents (50  $\mu\text{m}$ ) .

**Figure 4.15** Bone Sialoprotein (green) assay for hFOB 1.19 (blue nuclei) across each CA electrospun mats (a) CA Fiber Mat, (b) CA - KRSR, (c) CA - RGD, (d) CA – BMP-2 and (e) CA-MP. Scale Bar Represents 50  $\mu\text{m}$

**Figure 4.16** Alexa Fluor 488 Fluorescence Intensity Plot for BSP Expression Normalized by the Total Cells. Error Bars Represent the Standard Error of the Mean.

**Figure 4.17** Phalloidin Stained hFOB 1.19 Cytoskeleton at 14 days from BSP Assay. Scale Bar Represents 50  $\mu\text{m}$ .

**Figure 4.18** Phalloidin Stained hFOB 1.19 Cytoskeleton at 14 days from Collagen Assay.  
Scale Bar Represents 50  $\mu\text{m}$ .

**Figure 4.19** SEM Images of hFOB 1.19 on a) CA and b) CA-MP Fiber Mats after 14 Days  
of Incubation

**Figure 4.20** EDS of hFOB 1.19 Seeded on a) CA and b) CA-MP Fiber Mats

**Figure 5.1** TGA and DSC Analysis of nHAp>CNC (red), nHAp=CNC (black),  
nHAp<CNC (blue)

**Figure 5.2** Powder XRD Patterns of nHAp>CNC (red), nHAp=CNC (black), nHAp<CNC  
(blue)

**Figure 5.3** FTIR of nHAp>CNC (red), nHAp=CNC (black), nHAp<CNC (blue)

**Figure 5.4** SEM Images of Varying Ratios of nHAp:CNC Composites

**Figure 5.5** Cell Viability Against nHAp:CNC Composites

**Figure 5.6** SEM Images of hFOB 1.19 Morphology at a) control, b)HAp, c) CNC, d) HAp-  
CNC (3%), e) HAp-CNC (6%) and f) HAp-CNC (9%)

**Figure 5.7** BrdU Images for HAp-CNC Samples

**Figure 5.8** BrdU Positive Cells Expressed as Percentages with Total Number of Cells over  
each Sample

**Figure 5.9** Cell Viability Assay of hFOBs 1.19 Against HAp-CNC (3, 6, 9)% and with  
BMP-2 Inclusion

## **LIST OF SCHEMES**

**Scheme 1.1** Simplified Representation of Bone Cell Signaling During Remodeling 8

**Scheme 1.2** Representation of Osteoblastic Cell Adhesion to a Surface (i.e. biomaterial, extracellular matrix)

**Scheme 3.1** Preparation of Calcium Crosslinked Alginate Membrane

**Scheme 3.2** Catechol Redox Chemistry

**Scheme 4.1** CA Modifications: (a) deacetylation, (b) oxidation and (c) peptide coupling

**Scheme 4.2** Hypothesized Peptide Interactions and Effect on Cellular Attachment Preference

**Scheme 5.1** Representation of the Interaction between CNC and HAp in the Composite

## LIST OF TABLES

**Table 3.1** Phenols Detected by GC-MS in Water Samples from Las Cucharillas Sampling Sites

**Table 4.1** CA Coupled Peptide Structures

**Table 5.1** DLS analyses for HAp, CNC and nHAp-CNC at a 1% w/v

**Table 5.2** DLS analyses for BMP-2, nHAp>CNC and nHAp=CNC composites with protein at 1% w/v

**Table 5.3** Zeta Potential measurements of nHAp>CNC and nHAp=CNC with BMP-2



## LIST OF ABBREVIATIONS

Alg	Sodium Alginate
PEO	Poly(ethylene oxide)
PEG	Poly(ethylene glycol)
ES	Electrospinning
Catechol	1,2-Dihydroxybenzene
DOPA	3,4-Dihydroxy-L-phenylalanine
G	Guluronate
M	Mannuronate
Mw	Molecular Weight
AFM	Atomic Force Microscopy
SEM	Scanning Electron Microscopy
UV-Vis	Ultraviolet Visible Spectroscopy
SRT	Standard Reduction Potential
EtOH	Ethanol
MetOH	Methanol
EDS	Energy Dispersive Spectrometry
FTIR	Fourier Transform Infrared Spectroscopy
XPS	X-Ray Photoelectron Spectroscopy
HPLC	High Performance Liquid Chromatography
HCl	Hydrochloric Acid
GC-MS	Gas Chromatography coupled to a Mass Spectrometry detector
ACN	Acetonitrile
EA	Ethyl Acetate
HP-5MS	(5%-phenyl) – methylpolysiloxane Column
ICC	Immunocytochemistry
DMEM	Dulbecco's Modified Eagle Medium
PBS	Phosphate Buffered Saline

ECM	Extracellular Matrix
MTT	3-(4,5-Dimethylthiazol-2-yl)-2,5-Diphenyltetrazolium Bromide
ATP	Adenosine triphosphate
ADP	Adenosine diphosphate
CA	Cellulose Acetate
HS	Heparan Sulfate
BMP-2	Bone Morphogenetic Protein 2
SBF	Simulated Body Fluid
CCl <sub>4</sub>	Chloroform
DAPI	4', 6-diamidino-2-phenylindole
NaOH	Sodium Hydroxide
TEMPO	2,2,6,6-Tetramethylpiperidinyloxy
EDC	1-Ethyl-3-(3-dimethylaminopropyl)carbodiimide
Sulfo-NHS	sulfo-N-hydroxysuccinimide
NaOCl	Sodium Hypochlorite
HAp	Hydroxyapatite
BCP	Basic Calcium Phosphate Crystals
CNC	Cellulose Nanocrystals
HAc	Acetic Acid
MTS	[3-(4,5-dimethylthiazol-2-yl)-5-(3-carboxymethoxyphenyl)-2-(4-sulfophenyl)-2H-tetrazolium]

## **BIOGRAPHICAL SKETCH**

Simara Laboy López was born in September 30, 1993 in the city of San Juan, Puerto Rico to parents Norma I. López Ramirez and Eddie N. Laboy Nieves. Raised by her mother and her husband Rafael Rivera, half of her childhood was lived in the city and at the age of 9 moved to the town of Fajardo. Upon obtaining her high school diploma from Colegio San Antonio Abad in Humacao, she enrolled in the Interamerican University of Puerto Rico, Metropolitan Campus in 2011. There she graduated Magna Cum Laude with a Bachelor of Science in Chemistry and a minor in Biology in 2014.

That year she enrolled as a graduate student in Chemistry at the University of Puerto Rico, Rio Piedras Campus and began her research work under the guidance of Dr. Eduardo Nicolau. By his suggestion, she competed in Singularity University's Global Impact Competition Puerto Rico in 2016 and won a chair to participate of Global Solutions Program in NASA Ames Research Center, Mountainview, CA. That opportunity led her to learn about exponential technologies and how to leverage them to solve the world's greatest challenges in a Start-up Based environment. Upon her return, she took up a chemical consultant role with a local start up and was also part of the Yale Ciencia Academy 2017 Cohort. Afterwards she became a fellow of the Center for Innovation and Environmental Education in Nanotechnology (CIRE<sup>2</sup>N) where she has done numerous outreach activities and developed products for science communication. She obtained a Biotechnology certification based on her scientific interests and became a member of Puerto Rico Science Policy Action Network (PR-SPAN) in February 2019 with whom she has been active and performing different duties regarding Science Advocacy. In 2021, she resiliently finalized the requirements for the degree of Ph.D. in Chemistry with the completion of this thesis.

## CHAPTER 1: INTRODUCTION

Bones are essential components of the human body. They provide support, allow movement, protect organs, produce blood cells, and store minerals. Many individuals, upon aging begin to experience a gradual loss of bone mass and density resulting in a parallel gradual loss of their quality of life; and thus, the importance of this work.

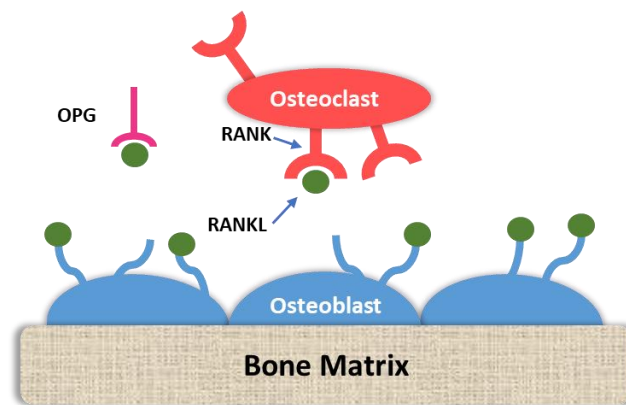
### 1.1. Bone Chemical Composition

Bone is composed of an organic (25%) and a mineral (60%) matrix with water occupying the resting 15%. The organic matrix is primarily composed of Type I Collagen (95%) and 5% is composed of proteoglycans and numerous non-collagenous proteins such as: Glycosaminoglycans, Osteocalcin, Osteopontin, Bone Sialoprotein, Osteonectin and cell attachment factors. This organic matrix is strengthened by deposits of calcium salts which nucleate with phosphates to form Hydroxyapatite,  $\text{Ca}_{10}(\text{PO}_4)_6(\text{OH})_2$ , (HAp) crystals who form the mineral matrix.<sup>1</sup> Together with collagen, the non-collagenous matrix proteins form a scaffold for hydroxyapatite deposition and it is this association that is responsible for the typical stiffness and resistance of bone tissue.<sup>2</sup>

### 1.2. Bone Remodeling and Regulation Mechanism

Bones are dynamic tissues that are involved in a constant state of remodeling upon reaching adulthood. Bone remodeling is a process that regulates the balance between the rates of bone formation and bone resorption. There are two major cells involved in the remodeling process: the osteoblasts, responsible for bone formation, and osteoclasts, multinucleated cells responsible for bone resorption.

The resorption process is initiated when an osteoprogenitor cell matures and differentiates into an osteoblast. Osteoblasts secrete a protein called the receptor activator of nuclear factor kappa B (RANK) which binds to the RANK ligand (RANKL) on osteoclast precursors. The RANK binding causes the osteoclast precursor to differentiate and become mature osteoclasts. When this occurs, osteoclasts anchor themselves to the surface of bone and release  $H^+$  ions to create an acidic microenvironment called the "clear, or sealed, zone". In this zone, the acidic conditions increase the solubility of the bone's mineral content and upon release of collagenase, cathepsin K and other enzymes, the remaining collagenous and decalcified matrix are digested.<sup>3</sup> It is after, that osteoblasts migrate into the space and begin depositing the organic matrix called osteoid; made predominately of collagen, where HAp forms afterwards.



*Scheme 1.1 Simplified Schematic Representation of Bone Cell Signaling During Remodeling*

This remodeling process plays an important role during bone development by optimizing the growing structure. When we are born, remodeling is dominated by bone formation until reaching the age of 30 where there is a remodeling plateau lasting until middle age where there is a decrease in the activity of osteoblasts compared to that of the osteoclasts and bone resorption begins dominating this

process. This process of bone remodeling is regulated by the secretion of osteoprotegerin (OPG) from the osteoblast, who is a decoy receptor to RANKL and blocks the binding of RANKL to RANK, thereby reducing osteoclast activity.<sup>4</sup> Various hormones regulate this balance between the secretion of RANKL and OPG; a misbalance in this regulation results in exceeded osteoclast activity which is the root cause of bone density related diseases. There are many factors that can result in this misbalance such as the intake of glucocorticoid (steroid hormones), traumatic injuries, human behavior such as poor nutrition, increases in workload, among others.

### 1.3. Treatments for Bone Disorders

Two major approaches exist to treat bone disorders: the pharmaceutical approach, and the tissue engineering approach. The most common approach is the pharmaceutical road that includes antiresorptive drugs and anabolic agents. Antiresorptive drugs, usually bisphosphonates, bind to bone mineral at the site of bone resorption and when taken up by mature osteoclasts, the cells lose their resorptive function therefore slowing down bone loss to allow natural bone production to catch up. And anabolic, such as antibodies, bind to RANKL and prevents its binding to RANK receptor on osteoclasts at any development stage resulting in an osteoblastic activation. Both drug alternatives present various risks to the patients ingesting them. In the case of the bisphosphonates there is an elevated risk of osteonecrosis of the jaw and unusual thigh fractures while in the case of the anabolic agents, can cause hypocalcemia (a decrease in calcium level).<sup>5</sup>

In Bone Tissue Engineering (BTE) approaches the goal is to engineer materials

that can promote migration, attachment, and growth of osteoblastic cells (osteoconduction), that can: stimulate differentiation of immature osteoprogenitor cells (osteoiduction), induce the formation of a direct chemical bond with surrounding tissue by eliciting a biological response at the interface (bioactivity) and form structural and functional connection between ordered living bone and a load-carrying implant surface (osteointegration).<sup>6</sup>

The BTE approaches include bone grafting procedures, bone implants and most recent has included the development of scaffolds. Bone grafting is a surgical procedure that replaces missing bone to repair complex bone fractures. Their downsides include limited availability, procurement morbidity, the requirement of a second surgery and can result in donor site pain, infection, fracture, or other complications. Grafting procedures are categorized by the source from which the new bone is coming from.

#### 1.3.1. Autografts

The most common bone grafting where fresh bone is transplanted from one site in the body to another from the same patient. Autogenous bones are osteoconductive, osteoinductive, and contain growth factors and osteogenic cells with no associated immune or infective-related risks.

#### 1.3.2. Allografts

These are bone substitutes derived from another living human or cadaver where demineralized bone matrix is transplanted from a donor tissue into the patient. They are osteoconductive; but because they have to be processed, lack important growth factors and proteins found in a healthy bone, presenting limited osteoinductivity.<sup>7</sup>

### 1.3.3. Xenografts

These are bone substitutes obtained from a non-human donor like bovine or porcine. They undergo many processing to remove the organic components of the bone to prevent antigen responses. They are osteoconductive; but not osteoinductive.

### 1.3.4. Cellular-based Grafts

These are allogenic or synthetic bone grafts that contain live mesenchymal stem cells (MSCs). These grafts are already osteoconductive and can promote osteogenesis so that the MSCs can differentiate into osteoblast cells.

## 1.4. Scaffolds

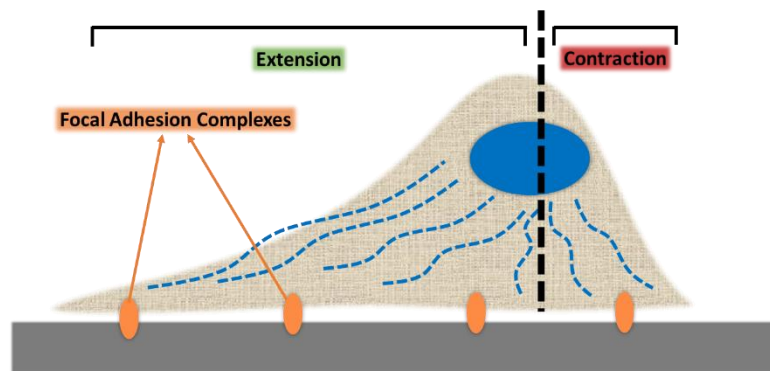
As previously described (1.3.1), the complex matrix embedding bone tissue specific cells consists of two components: the non-mineralized phase or the mineralized phase. Scaffolds are structures that bring support to the bone by mimicking the natural bone in the best way possible. A good scaffold must be both: biocompatible and bioactive. In terms of biocompatibility the scaffold must be made of materials that are not cytotoxic, and who have a good mechanical integrity with flexible void spaces because the bone is a porous structure with interconnected channels that allow the development of blood vessels and nerves. Besides pore interconnectivity, scaffolds should be three dimensional structures possessing high surface area and roughness; and, in the case of degradable scaffolds, that they do so at a controlled rate. The bioactivity of a scaffold can be attained by mimicking the components of the mineralized phase or the non-mineralized phase, or both. A scaffold's bioactivity is crucial because the scaffolds must be able to induce cellular



attachment, as it is the initial step in a cascade of cell–biomaterial interactions and crucial for processes such as proliferation, and differentiation. So, scaffold biocompatibility and bioactivity allow cell-biomaterial interactions that lead to adhesion and extracellular matrix (ECM) deposition for the development of mature osteoblasts that will form new collagen matrix and deposit HAp.<sup>8</sup>

#### 1.4.1. Adhesion

Cell adhesion (Scheme 2.2) is an essential determinant of this process and it is key to evaluate the potential of bone scaffolds. Cell adhesion has been studied in both synthetic and biopolymers, and it is in the latter, which most closely resembles the ECM, that cells are able to attach themselves with better ease and eventually grow tissue.<sup>9</sup> One of the properties that scaffolds must have are rough surfaces are one of the properties mentioned required for a scaffold because of the physiology of the osteoblast cells. Osteoblasts are anchorage dependent cells and the mechanical stimuli caused by rough surfaces causes the cells to develop the filopodia (protrusions from the membrane) that are responsible for the cell's movement and adhesion.<sup>10</sup> Attachment is a complex topic; but, in summary there are three mechanisms by which cellular attachment occurs.



*Scheme 1.2 Representation of Osteoblastic Cell Adhesion to a Surface (i.e. biomaterial, extracellular matrix)*

The membrane proteins in charge of attaching the bone cell's cytoskeleton to the extracellular matrix (ECM) are the integrins. Integrins are transmembrane heterodimeric receptors consisting of non-covalently associated alpha ( $\alpha$ ) and beta ( $\beta$ ) subunits.<sup>11</sup> Integrins recognize, interact with and are activated by extracellular matrix proteins, such as collagen, fibronectin, among others, to allow cell-cell contact and migration. A cell can have multiple-integrin receptor types expressed and they can all bind to the same ligand with different affinities. In osteoblast cells there are many types of integrin receptors as well; and a recent study by Olivares-Navarrete et al revealed the importance of  $\beta$ 1 subunit for roughness recognition and the  $\alpha$  subunits for chemical surface recognition.<sup>12</sup> This finding is highly relevant to predict to which materials can the osteoblast cells adhere to by means of physicochemical interactions to a substrate and their interactions with surrounding tissues. Each cellular system has their preferred adhesion mechanisms; but, for osteoblastic cells the bone related adhesive proteins are fibronectin, vitronectin, bone sialoprotein, thrombospondin, and osteopontin. In Chapter 5, osteoblastic adhesion is discussed with greater detail.

#### 1.4.2. Biopolymers in Scaffold Development

Biopolymers are recurring monomer units of either polynucleotides, polypeptides or polysaccharides) whose origins belonged to living matter.<sup>13</sup> Biopolymers can be fabricated in specific structures that can enhance their mechanical properties. Specifically, carbohydrate biopolymers like polysaccharides, have been used in the pharmaceutical industry and medicine fields because their production can be achieved at large scales and are relatively

economic. In the last century, life expectancy has increased thanks to scientific and medicinal advances; and with this increase, the need for tissue restoration has also appeared. Biopolymers are extensively used in the tissue regeneration field because cellular processes and responses are dictated by its microenvironmental surroundings that include the extracellular matrix (ECM), or scaffold, morphology, porosity, polymer composition, and bioactive factor release.<sup>14</sup> Biopolymers have found their way as membranes or composite materials in this field because they have shown to have potential and tunable characteristics to simulate the ECM of various systems including bone, cartilage, endothelial, cardiac, hepatic, neuronal, and other tissues.<sup>15</sup> Specifically biopolymeric membranes have been developed from several approaches like phase inversion, crosslinking, electrospinning, interfacial polymerization, surface deposition, among other techniques. Some biopolymers in BTE include Chitosan, Poly-l-Lactic Acid (PLLA), Gelatin, Dextran, among others. In this work we present the use of Alginate and Cellulose-based biopolymers.

Alginate is natural occurring polysaccharide that is abundant in nature as structural components in marine brown algae (Phaeophyceae) and as capsular polysaccharides in soil bacteria.<sup>16</sup> Alginates are unbranched polysaccharides composed of consecutive (1,4)-linked  $\alpha$ -L-guluronate (G),  $\beta$ -D-mannuronate (M) and alternating M and G residues. Due to the abundance of algae in water bodies, there is a large amount of alginate material present in nature. In this sense, alginate has been recognized as an important raw biomaterial to further tailor its intrinsic properties such as solubility, hydrophobicity, affinities among others.<sup>17</sup> The latter biopolymer, Cellulose, is a macromolecule, generally having a combination of

crystalline and amorphous regions and it is considered the most abundant natural organic polymer available in nature. It mainly originates from wood, plants or agricultural residues, tunicate marine animal, algae, and bacteria.<sup>18</sup> It has attractive features including biodegradability, chemical resistance, and thermal stability along with reactive surface functional groups.<sup>19</sup> For applications in BTE, cellulose has stood out because of its no cytotoxicity and chemical versatility made possible by the abundance of surface hydroxyl groups that can be modified to alter its intrinsic properties.<sup>20</sup> Among its structure, cellulose exhibits strong intermolecular hydrogen bonding and its crystalline structure make the linear homopolymer insoluble in majority of conventional solvents. The primary industrial use of cellulose has been the production of pulp and paper, and from these, through reactions with acetic acid and anhydride in the presence of sulfuric acid one can obtain the ester form of cellulose which would be the Cellulose Acetate (CA).<sup>21</sup> CA is used in a diversity of products including textiles, industrial uses like cigarettes and other filters for tobacco products, ink reservoirs for fiber tip pens, high-absorbency products such as diapers and surgical products, photography films, computer tapes, and LCDs.<sup>22</sup> And, the ordered crystalline regions of cellulose microfibrils (the molecule chains connected through hydrogen bonding with approximately 5-50 nm in diameter) are the cellulose nanocrystals (CNC).<sup>23-24</sup> CNCs can be attained using strong acids that can easily penetrate into the amorphous regions to hydrolyze them (hydrolysis) and leave the crystalline regions unaffected.<sup>25</sup> Among the properties of CNCs, they exhibit high specific strength and tensile modulus, high surface area, and unique liquid crystalline properties that have been useful in finding applications as

polymer-based nanocomposites ranging in high performance materials, in the field of electronics, catalysis, biomedical and to energy fields.<sup>26</sup>

#### 1.5. Hypothesis

It is of utmost importance to study the capability of biomaterials to induce biological responses that could favor bone cell osteoconduction and osteoinduction. Thus, it is hypothesized that *the combination of different biopolymer fabrication methods, along with diverse chemical interactions that simulate the bone matrix, will result in materials with the potential to aid as scaffolds for bone tissue regeneration.*

#### 1.6. Other Biopolymer Applications

Biopolymers have also been used in the field of membrane technology for water treatments. Membrane technology has been used for many years in desalination and wastewater treatment through the processes of reverse and forward osmosis. In the former process, the water to be treated is passed through a semi permeable membrane by means of pressure while the latter uses an osmotic pressure gradient to make water cross the membrane from what is called the feed solution (FS) into a draw solution (DS). In the last decades, membrane research has seen an increased growth because they brought a reduction in the size of equipment for water treatment, a decrease in energy requirements and low capital costs.<sup>27</sup> From an environmental standpoint, the separation process does not require additional chemicals, thereby minimizing secondary pollution, and they as can be chemically tailored to possess specificity for certain molecules making the membranes capable of being used for recovery applications.<sup>28</sup> The common choices for membrane materials include various hydrophobic polymers such as polysulfone (PSf), poly(ether sulfone) (PES), poly(vinylidene fluoride) (PVDF), among others who have the drawback of being prone to degradation and fouling during

filtration process.<sup>29</sup> And thus, some biopolymers such as chitin, tannins and previously discussed alginate and cellulose, among others, have been incorporated into membrane technology for wastewater treatments as well due to their hydrophilic properties.<sup>30</sup>

## CHAPTER 2: METHODOLOGY AND TECHNIQUES

### 2.1. Atomic Force Microscopy (AFM)

AFM is a high-resolution type of scanning probe microscopy (SPM). Consists of a sharp tip (10 to 20 nm in diameter) attached to a cantilever. The tip moves in response to tip–surface interactions, and this movement is measured by focusing a laser beam with a photodiode.<sup>31</sup>

### 2.2. Electrospinning

Electrospinning is a nanofabrication method used for the production of fibers in the micro or nanometer range. The principle of this technique is based on inducing an electrostatic potential to drive threads of polymer solutions from the bulk to a target. This occurs because the body of the bulk solution becomes charged and the electrostatic repulsion overcomes the surface tension making a droplet stretch until it protrudes from the needle or spinning tip it is contained. This technique has achieved interest due to the inherent properties of the electrospun fibers: large surface area to volume ratio, flexibility in surface characteristics and its scale up potential.<sup>32</sup>

### 2.3. Fourier Transform Infrared Spectroscopy (FTIR)

FTIR is a technique that uses the Fourier Transform (FT) mathematical operation to obtain a plot of intensity versus wavelength or wavenumber from an interferogram (a plot of intensity versus time). This plot occurs because when a compound or material is irradiated with infrared radiation, the molecules in the sample are excited into different vibrational states. The FT allows for the separation of individual absorption frequencies

that are unique to the modes of vibration of different functional groups. These modes have stretching and or bending behaviors in their molecular structures that occur due to the changes in dipole moments with time.<sup>33</sup> The FTIR spectrums presented in this work were obtained by using a Bruker Tensor 27 spectrometer using the attenuated total reflectance mode. We recorded the spectra between 500 and 4000  $\text{cm}^{-1}$ , with a 4  $\text{cm}^{-1}$  resolution and with a total of 64 scans.

#### 2.4. Ultraviolet Visible Spectroscopy (UV)

UV-Vis is a technique that allows the measurement of the absorption or transmission of a sample as a function of wavelength. The data can be both quantitative or qualitative and it is taken with a reference zero of the solvent the sample is in. This technique uses the principle of absorbance of light energy or electromagnetic radiation, which excites electrons from the ground state to an excited state of the material being studied.<sup>34</sup> The analysis of an UV plot is achieved by following the Beer-Lambert Law which states that for a single wavelength, the absorbance (A) is proportional to the molar absorptivity ( $\epsilon$ ) of the compound, the path length of the cuvette or sample holder (b), and the concentration of the solution (c).

$$A = \epsilon bc$$

The UV used for the obtention of the data presented in this work is a Shimadzu UV-1800. Blanks were always Nanopure water obtained from the Milli-Q system.

#### 2.5. Freeze Dryer

Freeze drying, or lyophilization, is the process of removing solid water from a product or formulation. This process occurs in a vacuum by means of sublimation and



consists of three parts: freezing, primary drying (sublimation) and secondary drying (desorption). After freezing the sample with liquid Nitrogen or Overnight placement in a -80 C freezer, the primary drying refers to removing the frozen water (ice form) and the secondary drying refers to removing the bound residual water. The equipment used to perform the lyophilization process was a benchtop Labconco Freezone 2.5.

#### 2.6. X-ray Photoelectron Spectroscopy (XPS)

Is a technique that analyzes the elements making up a sample surface (0.5-3 nm depth), its composition, and chemical bonding state by irradiating x-rays on the sample surface. Elements in a sample can be identified by their binding energies indirectly measuring the kinetic energy of the photoelectron emitted after irradiation.

#### 2.7. X-Ray Diffraction (XRD)

Is a technique that focuses an X-ray beam at a sample and measures the scattered intensity as a function of the outgoing direction. This outgoing direction will depend on the sample's crystalline structure which is responsible for scattering the beam and forming a diffraction pattern.

#### 2.8. Thermogravimetric Analysis (TGA)

A thermogravimetric instrument continuously measures the mass of a sample across a ramp of temperature that is changed over time. It can be used to determine sample phase transitions and decompositions.

## 2.9. Cell Culture

All cell culture experiments were performed using human fetal osteoblastic cell line hFOB 1.19 from ATCC® CRL-11372™. Culture medium was used was Dulbecco's modified eagle's medium (DMEM) / Nutrient mixture F-12, G418 Geneticin, and fetal bovine serum (FBS) which were purchased from Gibco-Thermo Fisher Scientific. The cryopreservation medium consisted of DMEM 72%, FBS 20% and Dimethylsulfoxide DMSO 8%). The cells were always incubated at their optimal temperature of 34 C with a 5% CO<sub>2</sub>.

## 2.10. Cell Immunocytochemical Assays

Immunocytochemistry is a technique for detection and visualization of proteins expression, or other antigens, in cells. It is achieved by using antibodies who are specifically developed for the recognition of a target of interest. The selected antibody binds to the target and is tagged with a fluorophore or enzyme can be excited by UV-Visible light and emit fluorescence.

## 2.11. Cell Dehydration for SEM

Cell dehydration uses glutaraldehyde to fix cells without damaging their cellular membrane surface thereby retaining their morphology to be viewed by microscopy. This procedure involves initial fixation and gradual washes of EtOH solutions starting at 10% and gradually increasing concentration until reaching 100%. Afterwards the cells are chemically dehydrated using HMDS by rinsing in pure HMDS/EtOH ratios of 1:3, 1:1 and 3:1 until reaching pure HMDS. Afterwards samples are gold coated and examined at the magnifications of interest using a SEM.

## 2.12. Viability Assays

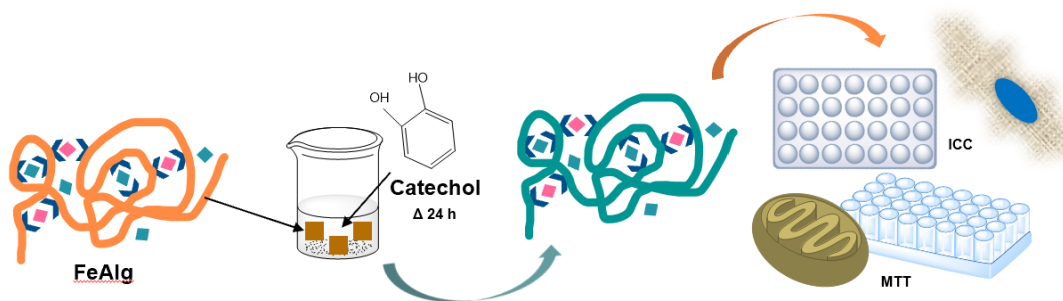
The principle behind cell viability assays is based on the conversion of tetrazolium salts MTT (3-(4,5-Dimethylthiazol-2-yl)-2,5-Diphenyltetrazolium Bromide) or MTS ([3-(4,5-dimethylthiazol-2-yl)-5-(3-carboxymethoxyphenyl)-2-(4-sulfophenyl)-2H-tetrazolium]) reagents into Formazan. The measured absorbance of formazan is directly proportional to the metabolic activity of cells because it is the mitochondrial reductase enzymes responsible for conversion of NAD to NADH<sup>+</sup> in the cellular respiration pathway.

## CHAPTER 3:ALGINATE MEMBRANES FOR POLYPHENOL RECOVERY

### ABSTRACT

This chapter presents the fabrications of alginate-based membranes using two different methodologies in the interests of achieving a polyphenol selective membrane. Membranes were prepared using a blend of Alginate with Poly (ethylene glycol) through the casting procedure and then Poly (ethylene oxide) was deposited via the electrospinning technique. The incorporation of ferric ion was included as the driving force in which catechols would bind through a coordination bond. Both membranes were characterized using AFM and SEM and the electrospun membrane was characterized with the additional techniques of FTIR and XPS. The membrane was tested for catechol adsorption using UV-Vis spectroscopy and upon adsorption verification, the removal potential from environmental water samples was explored. The characterization of the field samples was done using GC-MS and found no evidence of the catechol molecule. Preparing and using laboratory made catechol solutions, the catechol adsorbed membrane was tested for bioactivity potential with osteoblastic bone cell line by immunocytochemistry and evaluated catechol cytotoxicity using MTT assay.

### SYNOPSIS



## INTRODUCTION

Coastal wetlands are bodies of water that are transitional areas between terrestrial and marine ecosystems. These areas regulate floods, prevent soil erosion and serve as coastal protections.<sup>35</sup> In Puerto Rico, The *Ciénaga Las Cucharillas* wetland (18°26'25.27" N, 66°08'08.39" W), is an urban coastal palustrine/estuarine wetland located in the western side of the San Juan Bay. The remains of the original wetland covers an area of 500 hectares, the rest having been filled for urban and industrial use during the 20th century.<sup>36</sup> It is currently surrounded by highly urbanized and industrialized area, where discharges near the wetland are the main sources of organic and inorganic entrances into the system.<sup>37-38</sup> The entrance of polyphenols and phenol-based compounds into the aquatic environment results from natural, industrial, domestic and agricultural activities. Their presence may also be due to the degradation or decomposition of natural organic matter, disposal of industrial and domestic wastes and runoffs from agricultural lands such as *Las Cucharillas* site as exposed by Dr. K. Soto.<sup>39</sup> They are also synthesized by plants under the influence of certain external factors including UV radiation from sunlight, chemical stressors (cations, pesticides), and microbial infections.<sup>40</sup>

Polyphenols can be divided into different categories: flavonoids, phenolic acids, tannins, stilbenes and lignans and epidemiological data suggests there is a positive relationship between dietary exposure to polyphenols and health because they can act as anti-oxidants by chelating free radical species.<sup>41</sup> Among other applications of polyphenols, and due to their polymerization property, they have found applications as adhesives, sealants, coatings, and anchoring properties in various biomedical applications.<sup>42</sup> One specific group, catechols, are key components in many biological processes that include

pigment formation, neuron transmission, metal iron chelating, antioxidant properties, and robust adhesion.<sup>43</sup> As exposed by Luka, et. al., polyphenols can protect bones through five possible mechanisms: reduction of bone loss by the action of antioxidants, mitigation of bone loss through anti-inflammatory action, enhancement of osteoblastogenesis, suppression of osteoclastogenesis, and through osteoimmunological action.<sup>44</sup> This chapter focuses on the recovery of these phenols from water sources using 1,2-Dihydroxybenzene (catechol) as a model molecule.

Research conducted by Dr. Phillip Messersmith about catecholic amino acid 3,4-Dihydroxy-L-phenylalanine (DOPA), that is present in mussel adhesive proteins and can bind to organic and inorganic compounds, revealed the affinity of DOPA towards Titanium metals.<sup>45</sup> In other studies, DOPA has been identified as being able to penetrate water boundary layers to subsequently interact with local metal ions and form adhesive bonds with substrates.<sup>46</sup> Polyphenolic complexes including multiple catechol-grouped Tannic Acid have also been studied for surface coating applications due to its high affinity towards Iron III ions.<sup>47</sup> Many biopolymers exhibit the ability to form complexes through chelation with multivalent ions and form ionic bridges between the polymer chains resulting in solid and gel polymer networks.<sup>48</sup> Polymers can behave as polydentate ligands towards metallic ions such as Copper, Iron, Zinc, among others. Nevertheless, due to the intrinsic macrostructure of the polymers, there is a limited number of potential coordination sites that can be involved in coordination to the metal ion.<sup>49</sup>

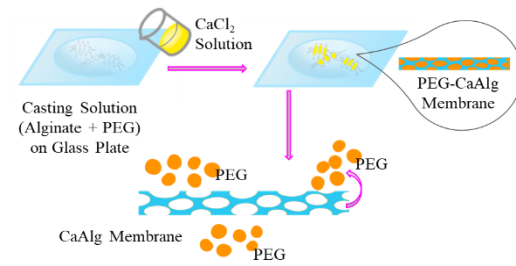
As mentioned in Chapter 1, part of the applications of alginates are their use as gel entrapment, microencapsulation, and hydrogel formulations; this is due to a unique property of alginates that they can crosslink in presence of divalent and trivalent cations.

This crosslinking occurs on the Guluronate (G) residues, so the mechanical properties of an alginate hydrogel depend on the M/G ratio. The amount and distribution of guluronate and manuronate depends on the sources from which alginate is isolated. Taking advantage of this affinity, Fe<sup>3+</sup> ions were incorporated into an electrospun Sodium Alginate hydrophilic membrane in the hopes of recovering polyphenols from water sources such as *Las Cucharillas* wetland ecosystem.

## RESULTS AND DISCUSSION

### 3.1. Alginate-PEG Membranes by Casting Procedure

Following a previously reported publication, the incorporation of Poly (ethylene glycol) (PEG) was done with the purpose of forming pores on alginate hydrogel after removing the PEG. PEG is a hydrophilic polyester prone to oxidative degradation, therefore, sufficiently stable in water for use in membrane applications.<sup>50</sup> Using a similar recipe to Kongyin Zhao's team for the creation of the membrane, sodium alginate and PEG solutions were prepared by stirring in deionized water.<sup>51</sup> When both polymers were blended, the mixture was used as a casting solution and was poured on a clean flat glass. Afterwards, a film casting doctor blade was employed on the glass in the interest of maintaining a homogeneous membrane thickness. The glass was placed in CaCl<sub>2</sub> to crosslink the alginate and then re-elute the membrane in warm water for a period of 48 hours to remove the PEG. Two different molecular weight (Mw) PEGs were used (PEG 400 and PEG 6000) to compare the effect on membrane morphology.



*Scheme 3.1 Preparation of Calcium Crosslinked Alginate Membrane*

### 3.1.1. Atomic Force Microscopy (AFM)

AFM was employed to verify with great detail the effect of varying the PEG molecular weight. The AFM images were obtained in the tapping mode of the instrument. The obtention of the images proved to be a very difficult task. The membranes had a gel-like structure and the cantilever tip would dig into the sample which upon removal, the tip would have a layer of alginate material surrounding it. The height scale was found to have a 100 nm difference, which is attributed to the increase in surface roughness resulting from the increase in PEG Mw. Due to this, the PEG 400 was discarded and PEG 6000 was used for the membranes.

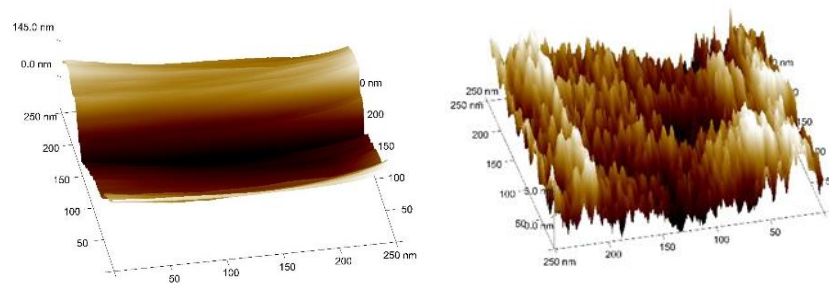


*Figure 3.1 AFM image of Sodium Alginate Membrane prepared with PEG (a) 400 Mw and (b) 6000 Mw*



### 3.1.2. Scanning Electron Microscopy (SEM)

The application of this membrane was to couple it to an osmosis filtration system and recover catechol. These systems are characterized by relying on membrane technology with varied pore diameters. In the search for pores, at the magnifications which the SEM images (Figure 3.2) were obtained, no pores were found.

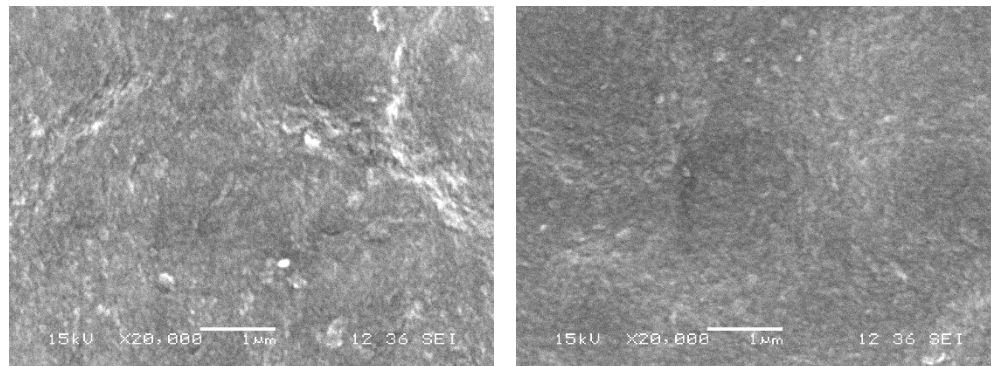


**Figure 3.2** SEM Images of  $\text{CaCl}_2$  Crosslinked Sodium Alginate Membrane Using (a) 1.5% and (b) 2.5% (w/v)

To corroborate water flux potential, the membranes were coupled as part of a suction filtering system and added water. There was no flow of water across the membrane and concluded that this membrane was impermeable. The presence or absence of pores does not mean that a membrane is useless. The sole objective of this project was to aid in the recovery of phenolic compounds via an Iron coordination compound. Instead of crosslinking the alginate membrane with  $\text{CaCl}_2$ , the membrane was crosslinked with a 0.1 M  $\text{FeCl}_3$  and resulted in a very brittle, shapeless gel. As an initial test to use as a proof of concept and evaluate whether optimization would be necessary, the gel was added to a 0.1% w/v catechol solution.

Due to the aromatic nature of catechol, the molecule can be detected and quantified using UV-Vis. Catechol has a maximum absorption at 275.5 nm. The expected behavior would be to find a decrease in catechol absorbance after iron gel

addition; but, upon interaction the solution began to change color to a blueish-green hue. This behavior suggested that the iron was not strongly bounded to the alginate gel and it was leaching from it. The change in color was occurring as a result of the oxidation of Iron given that in this solution the Iron III half-reaction ( $\text{Fe}^{3+} + \text{e}^- \rightarrow \text{Fe}^{2+}$ ) has a stronger tendency to occur than the oxidation of catechol due to its larger standard reduction potential (SRT) of +0.77 V against catechol SRT of +0.577 V. Besides the leaching of Iron from the Alginate gel, if Iron III oxidizes to become Iron II then the reaction will not proceed in the desired direction. To achieve porous structures and in the interest of achieving more favorable mechanical integrity of the alginates the casting solution method was replaced with electrospinning (Chapter 2).

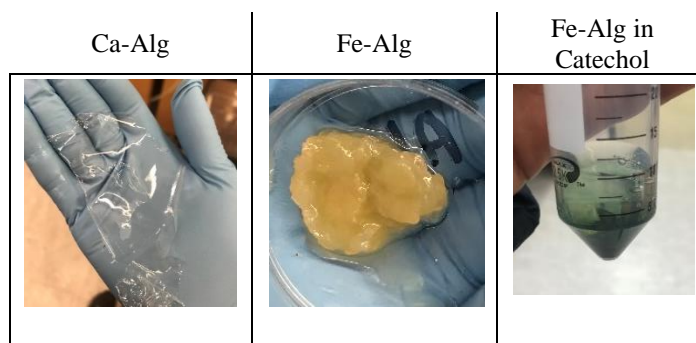


*Figure 3.3 Pictures of the Alginate Formulations and Effect on Catechol Solution*

### 3.2. Alginate-PEO Membranes by Electrospinning

ES has been widely utilized for different applications such as water remediation, bone healing, drug delivery, sensors, among others due to its capacity of creating fibrous membranes with high volume to surface areas.<sup>52</sup> For a polymer solution to work with the electrospinning technique, the polymer must be viscous enough to allow the formation of fibers by electrostatic repulsion. Sodium alginate, whose solubility is only in water could not be electrospun by itself. Previously used PEG has a low molecular

weight and blending it with the Alginate would not increase the viscosity of the polymer blend solution. Other works have reported the use of Poly(ethylene oxide) (PEO), in essence a high molecular weight PEG, to use in casting solution method as a pore-forming agent to rinse away after membrane solidification. In the interests of increasing viscosity and pore formation to achieve an increased surface area, an alginate-PEO blend was explored for membrane formation using ES. Several Alg:PEO ratios were tested and evaluated; the blend ratio that worked best for this project was a 7:3 ratio using a PEO LMw.

The fabrication of the electrospun membranes was achieved by using the following parameters: pumping rate of 1.5 mL/hr with an electrical potential of 7 kV at a 10 cm distance between the syringe tip and the collector rotating at 100rpm. Part of the industrial process of alginate extraction involves direct precipitation of Alg from a biomass extract with ethanol.<sup>53</sup> Taking advantage of this behavior and with the combination of the crosslinking properties of alginates, the electrospun membrane was immediately submerged into  $\text{CaCl}_2 \cdot 2 \text{H}_2\text{O}$  (3%) in EtOH. This step simulates the phase inversion methodology, commonly used for the creation of filtration membranes, where solvent replacement occurs as an exchange between water and EtOH molecules resulting in membrane separation from the aluminum foil. After 1 hr, consequent submersion in  $\text{FeCl}_3$  (3%) in EtOH for equal time allowed the incorporation of  $\text{Fe}^{3+}$  ions to the membrane. They were thoroughly washed with EtOH to prevent Iron leaching and left to dry at ambient conditions.

### 3.2.1. Catechol Adsorption

A 40 ppm Catechol solution was prepared. Adsorption experiments were done by placing 15, 30, and 60 mg of the Alg-PEO membranes in 10 mL individual

beakers, in triplicate, with the solutions on a platform shaker at 100 rpm. The absorbance of catechol was measured before ( $t_0$ ) and after incubation with membranes ( $t = 4, 24$  hrs). Catechol concentrations were calculated from the linear equation obtained from a calibration curve and plotted against the mass of the Alg-PEO membrane added (Figure 3.4).

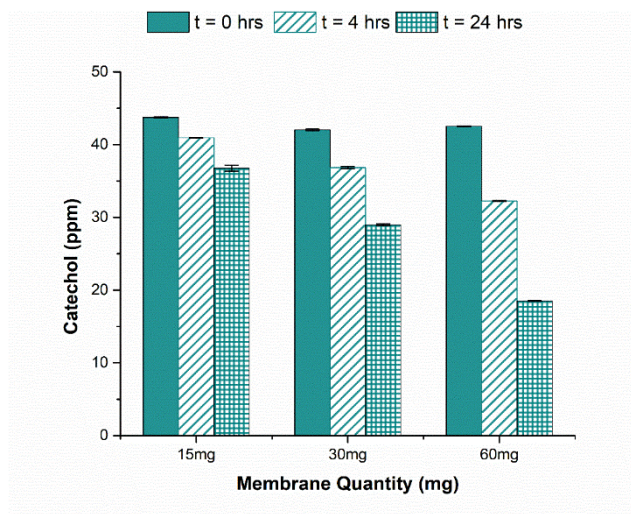


*Figure 3.4* Calculated Catechol Concentrations from Measured Absorbance at 275.5 nm before and after Incubation Periods of 4 and 24 hours.

### 3.2.2. Physical Characterization

The membranes were characterized by AFM (Figure 3.5) to compare the morphology against previously studied membranes fabricated using the casting method. The scale on the y-axis display a 1.9  $\mu\text{m}$  value while with the previous method (Figure 3.1) at most 250 nm. The ES method did result in membranes with a higher surface area and SEM images were collected afterwards (Figure 4.6).

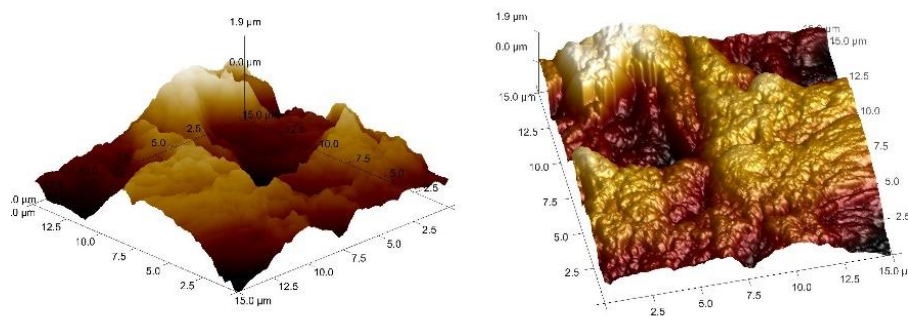


*Figure 3.5* AFM Images of Electrospun Alg:PEO Membranes



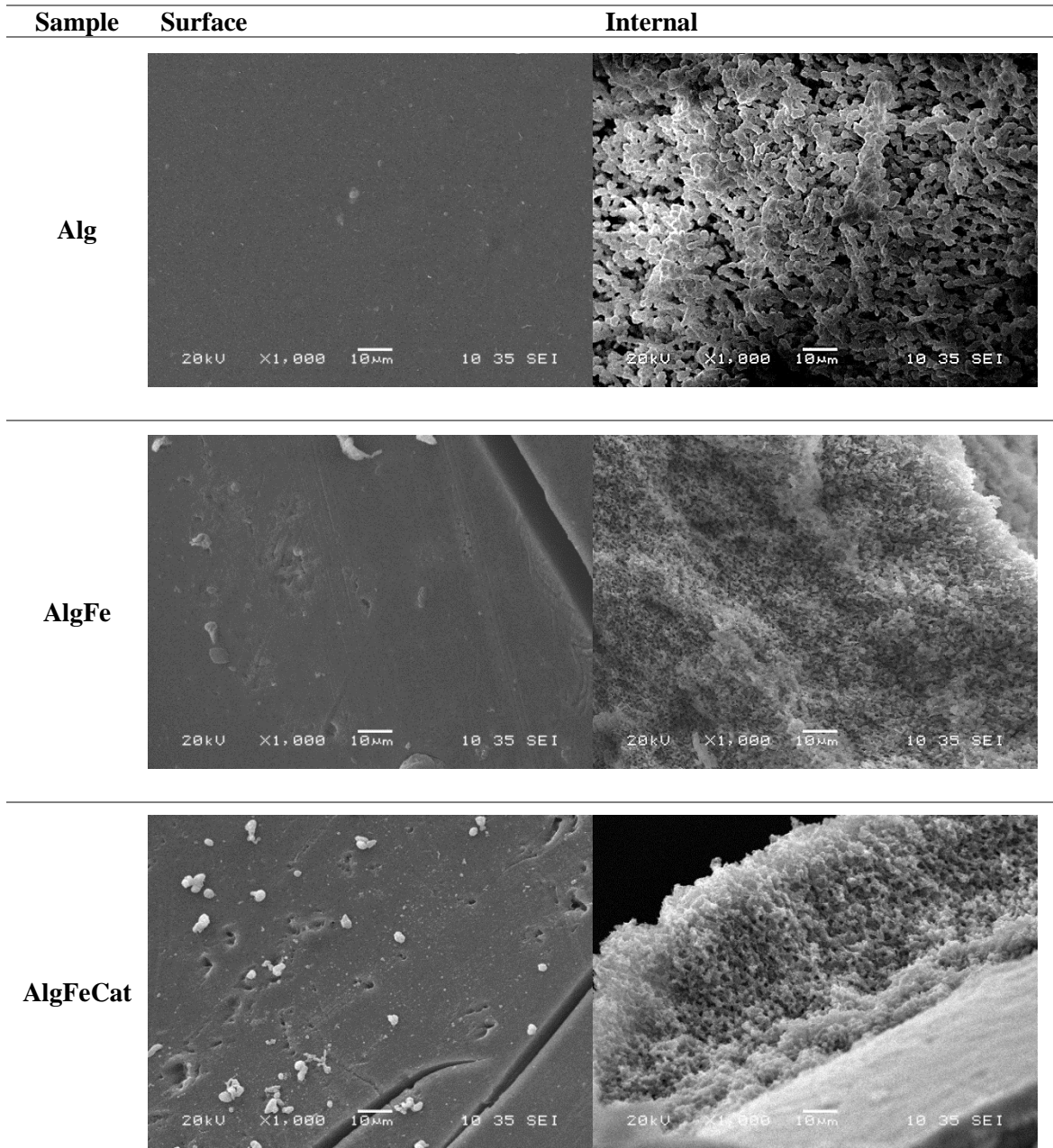


*Figure 3.6 SEM Images of Top Membrane Surface and Internal Morphology of Alg and its Subsequent Reactions*

Observing the surface of the AlgFeCat in Figure 4.6, there are some spheres forming in the surface which are believed to be catechol agglomerations. To verify this, Energy-dispersive X-ray spectroscopy (EDS) was performed; but, the chemical composition of the spheres would be equal to the chemical composition of the membrane since the atoms of each were Hydrocarbons and Oxygens with the Gold present from the Gold Sputtering performed for SEM analysis (Figure 3.7).

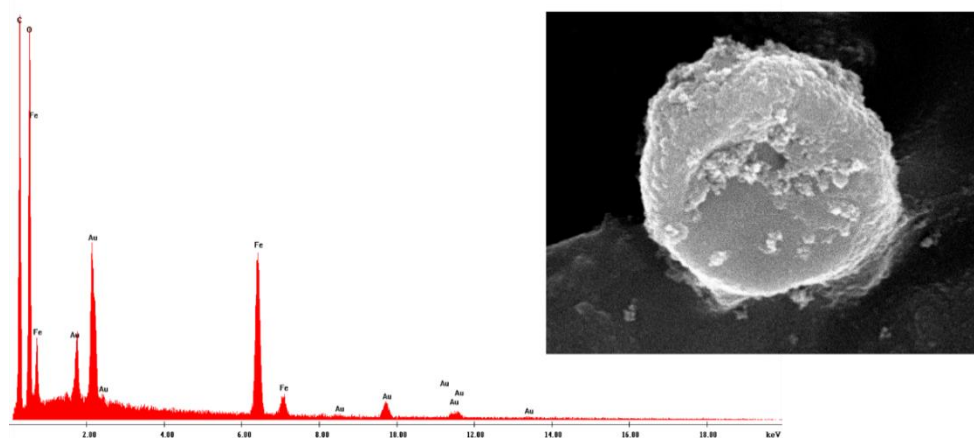


*Figure 3.7 EDS Spectrum of AlgFeCat Surface Sphere*

### 3.2.3. Chemical Characterization

FTIR was performed to find evidence of catechol presence. As can be seen in Figure 3.8, the initial membrane displayed a small and sharp peak that is characteristic of the PEO polymer; and after Iron incorporation and subsequent catechol solution submersion disappeared, suggesting the PEO had completely dissolved, and the structure left was a pure Alginate membrane. After immersing the AlgFe membrane in catechol solution, there was no evidence of ring C=C absorptions ( $1600 - 1475 \text{ cm}^{-1}$ ) nor phenol hydroxides ( $3050 - 3010 \text{ cm}^{-1}$ ) due to the large overlap with membrane -OHs. It is suggested that the amount of catechol adsorbed was too low to be detected.

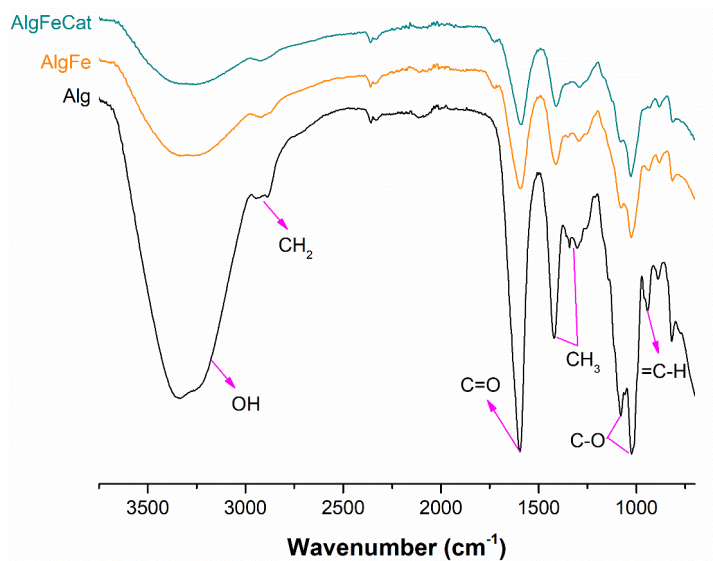
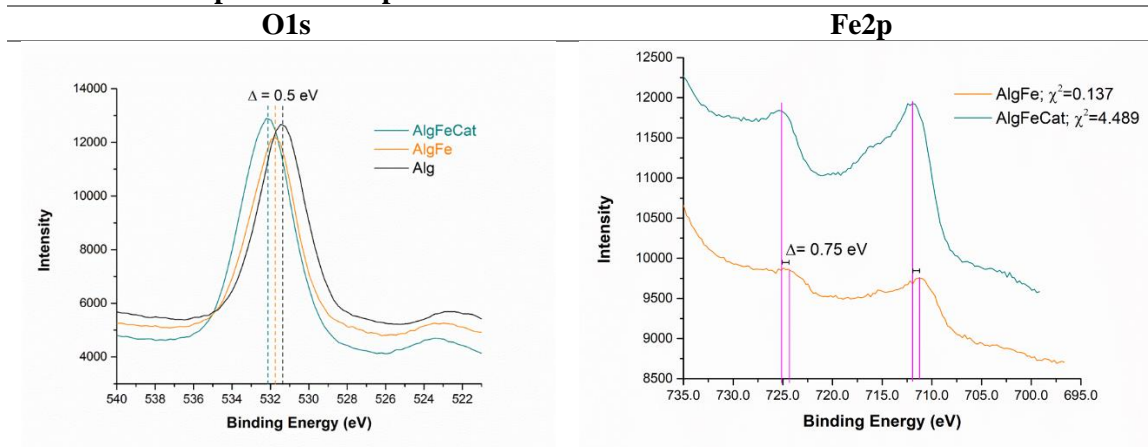


Figure 3.8 FTIR of Alg (black), AlgFe (orange) and AlgFeCat (turquoise) Membranes

Since the adsorption was occurring at the surface of the membrane, XPS was employed to study the interactions through the hydroxides (-OH) involved in the interaction with Iron. As seen in Figure 3.9 A, the recorded spectra for O1s shows a 0.5 eV shift towards higher Binding Energy with each treatment while the Fe2p is shifted 0.75 eV; a clear indication of a reaction occurring. Figure 3.9 B shows the O1s deconvolution where it can be appreciated that initially the Oxygen is bonded to the Carbon as simple and double bonds from the chemical nature of the Alg. After iron incorporation, a new coordination oxygen arises from the interaction with ferric center and after catechol adsorption, a decrease in the intensity of the iron-hydroxides and an increase in the double bonded oxygen with carbon can be seen. This increase in O=C intensity can be explained by considering that at acidic pH, catechols and  $\text{Fe}^{3+}$  react producing o-quinones.

## A. O1s and Fe2p Recorded Spectra



## B. O1s Deconvoluted Spectrums

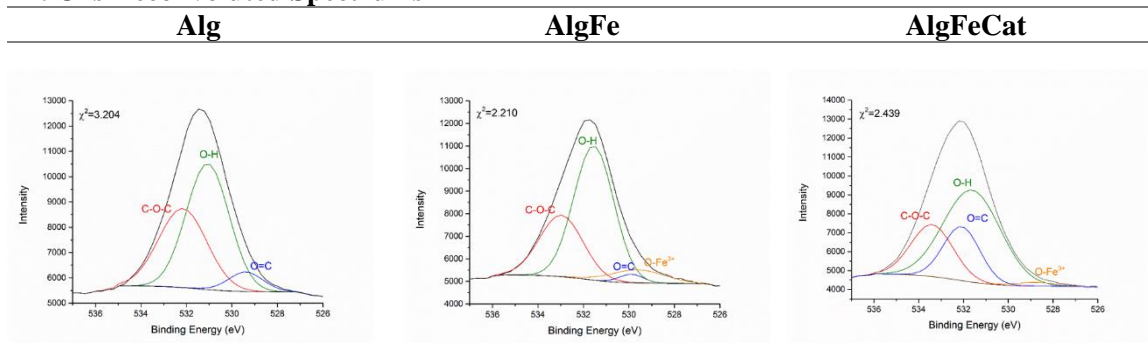


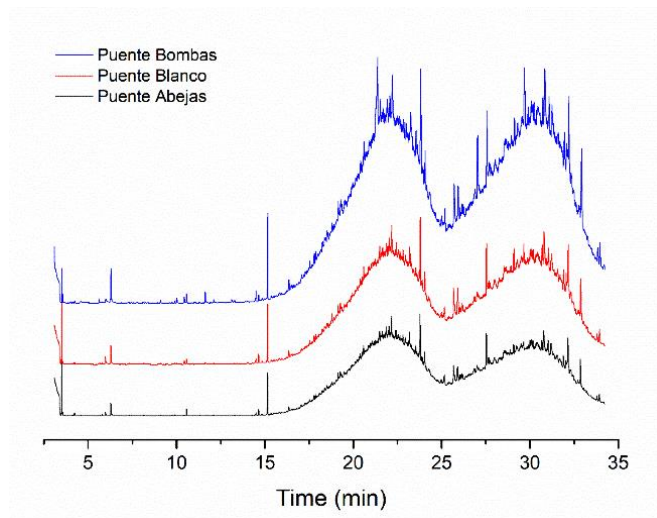
Figure 3.9 XPS Spectrums for Alg Membranes After Reactions

### 3.2.4. GC-MS Analysis of Environmental Samples

Samples belonging to *Las Cucharillas* environment were obtained to measure the viability of our membranes working with samples containing other interferences. Collection locations were from Puente Abejas (18.438087, -66.138550), Puente Blanco (18.4278105, -66.1342688) and Puente Bombas (18.447550, -66.135776). Water was collected in 1 L amber glass bottles and refrigerated quickly. The water was filtered with 0.2  $\mu\text{m}$  vacuum filters and stored in a 4 °C cold room. Before analysis, the water samples were pre cleaned by Solvent Phase Extraction (SPE) using reverse phase retention mechanisms to retain organic analytes; the cartridges used were Supelco's DSC-18 columns. SPE columns were

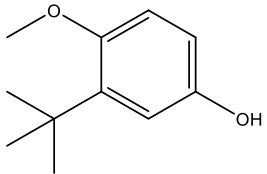
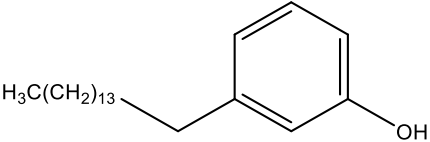
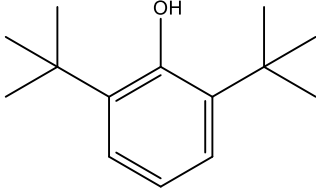
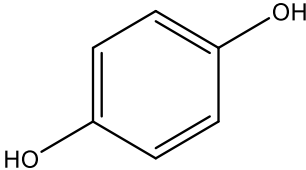


rinsed with 2 mL Acetonitrile followed by 2 consecutive 5 mL Methanol (MetOH) washes. To ensure that our molecules of interest were protonated, the samples were



*Figure 3.10 Gas Chromatogram of Field Water Samples Collected*

acidified to  $\text{pH} = 2$  using Hydrochloric Acid (HCl). They were added at 5 mL/min through the columns and the recovered water was subsequently used for solvent exchange extraction. This process was performed using Acetonitrile followed by the addition of Anhydrous Sodium Sulfate ( $\text{NaSO}_4$ ), filtering and using a rotary evaporator to recover the organic extract from the samples. The extracts were used for the analysis using Ethyl Acetate as the aqueous phase in a HP-5MS (5%-phenyl) – methylpolysiloxane column. The analysis parameters were as follows: using 10  $\mu\text{L}$  sample volume with flow rate of 1.5 mL/min and heating ramp of 8  $^\circ\text{C}/\text{min}$  until 300  $^\circ\text{C}$ . The phenols present in the samples are shown on Table 3.1. With the GC-MS analysis, the concentration of catechol was not detected; it is a possibility that the concentration of catechol in the samples was too small. As such, in order to proceed to evaluate the bioactivity of the membranes, catechol was adsorbed from prepared, and previously used, 40 ppm catechol solution.

Sample Site	Phenols Present, Time (min)	
Puente Bombas	3-(1,1-dimethylethyl)-4-methoxyphenol, 14.502	3-pentadecyl-phenol, 27.039
		
Puente Blanco	2,6-bis(1,1-dimethylethyl)-phenol, 14.016	
		
Puente Abejas	1,4-benzenediol, 30.678	
		

**Table 3.1** Phenols Detected by GC-MS in Water Samples from Las Cucharillas Sampling Sites

### 3.2.5. Catechol Bioactivity

Osteoblastic cell lines are adherent cell types; meaning that if they fail to attach to a surface, they will not be able to proliferate and mature. To test the bioactivity potential of catechol with bone cells (Chapter 3), the focal adhesion points were tagged to corroborate the adherence of the cells to these membranes. Immunocytochemistry (ICC) was performed using Goat Anti-Rabbit Vinculin antibody with Polyclonal Alexa Fluor 594 AffiniPure Goat Anti-Rabbit IgG (H+L) and Phalloidin-iFluor 488 Reagent to stain the actin filaments of the cell's cytoskeleton. The well plate was designed as to include a glass disc as control, Calcium-crosslinked Alginate membrane (Alg), Iron-crosslinked Alginate membrane (AlgFe), and catechol adsorbed membrane (AlgFeCat). The cells would be examined at 3 and 7 days. After initial cell seeding in well plates with the membranes, the culture medium was changed every other day with much care. Each passing day would deteriorate the hydrogel membrane's mechanical integrity. After the start of the immunocytochemical procedure, which requires numerous steps of multiple pipetting involving the fixation of cells, thorough washes with PBS, among others, the Alg was completely dissolved. Only a fraction of the AlgFe and AlgFeCat was able to be recovered and mounted on the microscope slides. As can be observed in Figure 3.11, the cells on the AlgFe showed no presence of filopodia extension for surface attachment and adopted small round shapes. In contrast to the rationale that Catechol would drive cellular proliferation, no cells were found on the AlgFeCat membranes. The first visible indication of cellular apoptosis is cell shrinkage; therefore, to test whether it was catechol catalyzing cell death or if cell death was due to another factor, an MTT cytotoxicity Assay was performed.

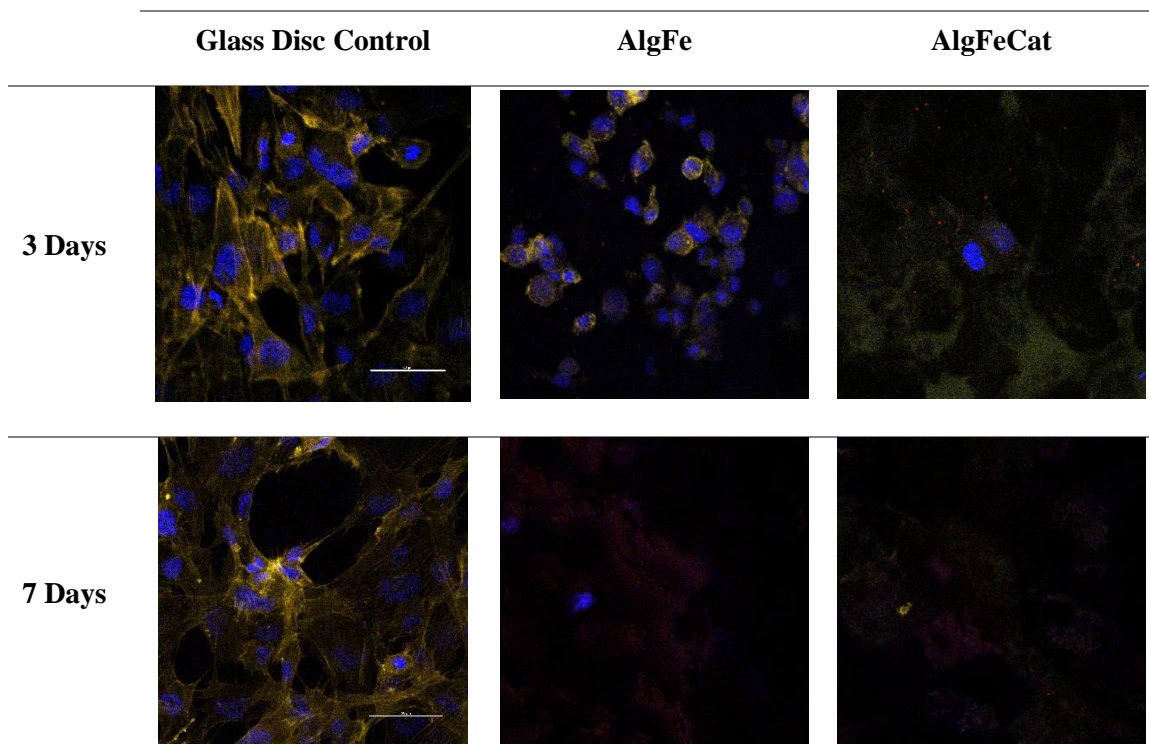


**Figure 3.11** Vinculin Expression of hFOB 1.19 in Alginate Membranes. Scale Bar represents 50  $\mu\text{m}$ .

The MTT assay was performed following the established protocol from the purchased kit. Briefly,  $2.0 \times 10^4$  cells were seeded per well with catechol/DMEM at 0.5, 1, 5, 10, and 20 ppm concentrations. Upon seeding they were incubated for 24 h and 10  $\mu\text{L}$  of MTT reagent were added afterwards. The cells were incubated for 4 hours with the MTT followed by 1 hr incubation after 100  $\mu\text{L}$  of 0.04 N HCl in isopropanol were added. The plate was centrifuged for 10 min at 10,000 rpm and the supernatant was transferred to a new plate for absorbance to be measured at  $\lambda_{570}$  (experimental values) and  $\lambda_{530}$  (DMEM absorbance). The results were plotted as the Experimental – DMEM absorbances against the catechol concentrations. As can be observed in Figure 3.12, an exponential increase in absorbance is observed beginning at 5 ppm. Single factor analysis of variances (ANOVA) was performed to test the significance of those values. The obtained F value was 57.3301 and at a

99% confidence interval the F value is 5.0643. The acceptable statistically significant values were only those at 0.5 and 1 ppm giving an F value of 0.4386.

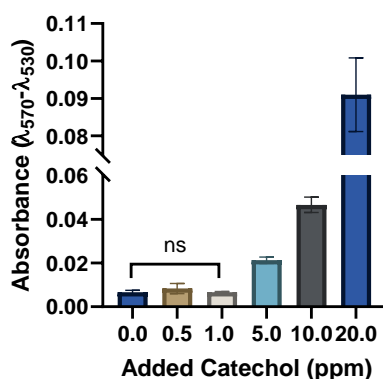
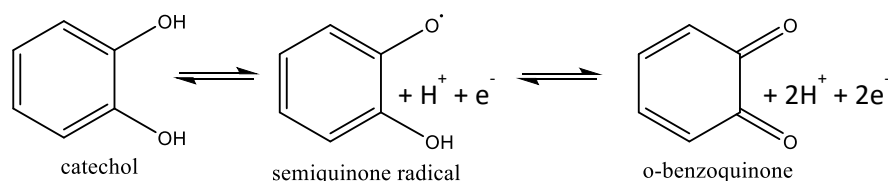


*Figure 3.12 MTT Assay of Catechol Cytotoxicity. Statistically Accepted Values Between Asterisk Bracket*

As discussed in Chapter 2, the MTT assay measures the absorbance of formazan molecule formed after enzymatic reduction of the MTT reagent by the mitochondrial enzymes. And thus, the absorbance is directly proportional to the enzymatic activity of the mitochondria in the process of cellular respiration. The results of the assay show that there is an elevated increase in enzymatic activity (cellular respiration) beginning at 5 ppm. Cells can increase their mitochondrial activity in respiration either by increasing their viability as a positive response to the experimental external stimuli or due to stressful responses to it.

Small polar molecules such as Catechol can travel across cell membranes; the biggest restrictions apply to the diffusion of highly charged molecules such as ions, and large molecules. Catechol can cycle between catechol, semiquinone radicals and ortho-benzoquinone because it can perform redox reactions. The equilibrium potential for the one-electron transfer between catechol and the semiquinone radical at pH = 7 is 100 mV and for the transfer between the semiquinone radical and the o-benzoquinone is 530 mV as previously reported; meaning that at physiological conditions, catechol is not auto-oxidized.<sup>54</sup>



*Scheme 3.2 Catechol Redox Chemistry*

There are three possible mechanisms that may be used to explain the behavior with catechol. (1) Many cellular enzymes have heavy metal centers and thus, upon encounter, catechols are oxidized enzymatically where electrons are transferred to molecular oxygen forming superoxide O<sub>2</sub><sup>-</sup>.<sup>55</sup> Upon encountering transition metals they react to reduce them which result in the reduced metals catalyzing sets of reactions that result in the formation of hydroxyl free radicals and reactive oxygen species (ROS). (2) As proposed by Schweigert et al., oxidized catechols react with sulphhydryl groups of proteins resulting in protein inactivation or formation of glutathione radicals by reactions with glutathione groups.<sup>56</sup> And (3), the catechol acts as an uncoupling agent of oxidative phosphorylation. In the latter mechanism, catechols act as proton carriers allowing protons to flow into the mitochondrial matrix without passing through the transmembrane protein complex that synthesizes adenosine triphosphate (ATP) from adenosine diphosphate (ADP) and electron transport proceeds in the normal fashion, but ATP is not formed.<sup>57</sup> Under normal conditions, the rate of oxygen consumption in the absence of ADP is low; but, with the addition of an uncoupler such as catechol, the respiratory rate increases in a dose-dependent manner just like what was observed in Figure 3.12 and progenitor cells have to rely on glycolysis as their main energy source.<sup>58</sup> It is this loss of respiratory control that leads cell into increased oxygen consumption as a compensatory function of detained ATP formation.<sup>59</sup> This last mechanism most closely resembles

the observed behavior with the MTT assay; if this is true, then it could also explain why the cells cultured with the AlgFeCat membrane did not survive since the calculated concentration of catechol adsorbed was 5.6 ppm assuming full adsorption. If the catechol was not the primary agent causing cell death then in the ICC assays, it is highly possible that the death behavior was a response to the lack of void space in the membranes that would allow the exchange of nutrients and eventually become a space for matrix deposition upon cellular differentiation and maturation.

## CONCLUSIONS

Using the knowledge from water purification membranes, an attempt at creating a membrane using an analogous procedure resembling the commonly used phase inversion technique was made to recover phenolic molecules from water sources. The selected Sodium Alginate polysaccharide did not have the required properties needed to develop such membranes. As such, the incorporation of another fabrication technique, electrospinning, was employed. ES membranes were achieved by incorporating another biopolymer with a high viscosity (PEO). The membranes were tested for recovery potential in laboratory conditions and the capacity to absorb was found to be proportional to the amount of membrane used as well as the contact time. The question remains whether they could work in environmental sites and if they would really be selective towards polyphenolic molecules. Nevertheless, the incorporation of Iron is a good approach to achieve phenolic specificity for related applications.

The chemical characterization through XPS was used to corroborate the adsorption of catechol to the membranes and afterwards they were tested for bioactivity with osteoprogenitor cells. It is unclear whether the reason that the cells did not survive in the

membranes was due to the cytotoxicity of catechol or to the dense morphology of the alginate hydrogel membrane. To disregard the catechol cytotoxicity hypothesis, an assay for the detection of hydroxyl and superoxide radicals is suggested. Sodium Alginate scaffolds should be coupled to another polymer with good mechanical integrity and added cellular attachment motifs or increased surface roughness to be considered as potential materials for bone tissue regeneration.

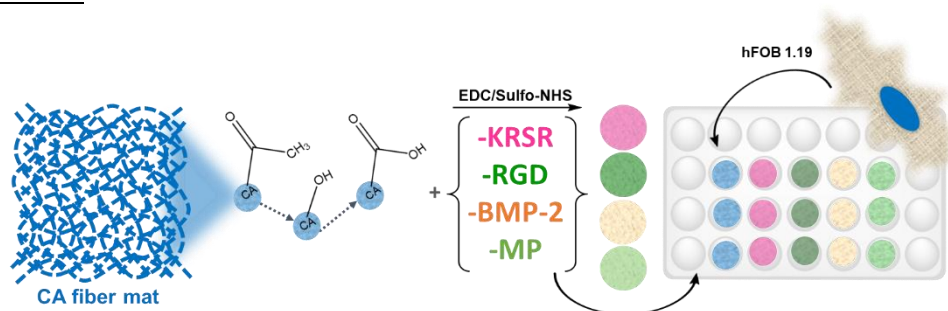


## CHAPTER 4: PEPTIDE COUPLED CELLULOSE ACETATE FIBER MATS AS BIOACTIVE SCAFFOLDS

### ABSTRACT

This chapter presents an organic – biological approach used in the design of a bioactive scaffold model. Using the electrospinning technique with Cellulose Acetate as starting material, a porous fiber mat was obtained to mimic the collagen fibers within bone extracellular matrix (ECM). The mats were chemically modified by two approaches in preparation for bioactivation. The fiber mats were bioactivated by coupling adhesive peptides -KRSR, -RGD and growth factor -BMP-2 to study their potential for Bone Tissue Regeneration (BTR) which was evaluated using Immunocytochemistry (ICC). The bioactive mats were characterized using FTIR, TGA and SEM/EDS and showed average fiber sizes of 120  $\mu\text{m}$ . The biological assessment of the fiber mats revealed cells were proliferating in all fiber mats; but to a greater extent in the multi-peptide coupled mat. Adhesive integrin  $\alpha_v\beta_3$  was activated and expressed at 7 days of culture and both maturation markers of Collagen and Bone Sialoprotein were present at 14 days of incubation. EDS analysis revealed that cells were producing Calcium and Phosphorous deposits around their structures meaning they were forming new bone and thus, making this CA Fiber Mat a potential scaffold material in the field of BTE.

### SYNOPSIS



## INTRODUCTION

Scaffolds are structures that bring support to the bone and can be used to promote bioactivity by behaving as templates for tissue deposition and facilitating cell proliferation.<sup>60</sup> The bone is a porous structure with interconnected channels that allow the development of blood vessels and nerves.<sup>2</sup> Scaffolds should also have a three-dimensional structure possessing high surface area and roughness. Cell adhesion has been studied in both synthetic and biopolymers, and it is in the latter, which most closely resembles the ECM, that cells are able to attach themselves with better ease and eventually grow tissue.<sup>9</sup>

Osteoblasts are anchorage dependent cells and the mechanical stimuli caused by rough surfaces causes the cells to develop the filopodia protrusions in the membrane that are responsible for the cell's movement and adhesion. As previously mentioned, Olivares-Navarrete et al revealed the importance of  $\beta$ 1 subunit for roughness recognition and the  $\alpha$  subunits for chemical surface recognition.<sup>12</sup> Adhesion can be mimicked by stimulating the proteoglycan membrane containing heparan sulfate as one of its components. A peptide sequence that has been found in the five different bone related adhesive proteins mentioned in Chapter 1 has shown to be selective for osteoblast adhesion; this sequence is KRSR and it binds to heparan sulfate. A study evaluated different cell types and their finding are that some cell lines required the addition of a heparin binding peptide to be able to proliferate and anchor themselves to the substrate as the heparan sulfate (HS) is one of the linear polysaccharides that form the glycosaminoglycans which cells recognize.<sup>61, 62</sup>

Besides glycosaminoglycans, many cells recognize arginine-glycine-aspartic acid-X (RGDX) sequences, where X is one of several possible amino acids. These are adhesive peptide sequences which mediate integrin receptor interactions and are exhibited by many

ECM molecules such as fibronectin, vitronectin, bone sialoprotein, and osteopontin. In fibronectin, a type of adhesive glycoprotein, RGD<sub>X</sub> recognizes a number of integrin ligand receptors like  $\alpha_v\beta_3$  (Figure 1) ligands on various cell types.<sup>63</sup> Providing both heparin binding and integrin binding domains may have a synergistic effect on osteoblast cell adhesion and spreading and may lead to enhanced newly formed mineralized tissue.

Another protein involved in the development and regeneration of tissue and cartilage is the Bone Morphogenetic Protein 2 (BMP-2), which is the most potent osteoinductive growth factor. However, the complex multilevel structure of BMPs makes the protein prone to degradation and loses its bioactivity quickly in physiological conditions. Because of this, peptides from the active sites of the BMPs have been isolated and identified.<sup>64</sup> Specifically for the BMP-2, the peptide sequence was identified as: KIPKASSVPTELSAISTLYL, and was proven to signal bone cells into proliferation and differentiation.<sup>65</sup>

In the last decades, cell-based approaches for bone tissue engineering, has focused on pre-calcified materials or simulated body fluid (SBF) treated models who fail to reproduce either the complexity of the bone 3D microenvironment or the nanoscale characteristics of mineralized bone collagen.<sup>66</sup> Thus, taking the beforementioned reasons, in this chapter we a scaffold model was developed using Cellulose Acetate (CA) biopolymer to take advantage of its versatile applications and different arrangements that can favor osteoblastic adhesion. We used the electrospinning technique with Cellulose Acetate as starting material to create a porous electrospun membrane mimicking the collagen fibers within bone extracellular matrix (ECM). We modified this CA membrane to provide

surface roughness and bioconductivity and study its potential to be used as a scaffold material in the fields of bone tissue regeneration.<sup>67</sup>

## RESULTS AND DISCUSSION

### 4.1. Synthesis of Cellulose Acetate Electrospun Fiber Mat

Following a previous report by Tungprapa et al.<sup>68</sup> on the morphological effect of solvent systems with CA electrospun fibers, a 5% CA solution was prepared by dissolving a certain amount of the polymer (CA, 30,000 g/mol) in a 9:1 mixture of CCl<sub>4</sub> and Acetone. The solution was left in constant stirring for a period of 20 hours. Then, the solution was used to fill a conductive syringe connected to the positive electrode of the high voltage power supply (Gamma High Voltage Research). The needle was kept 10 cm apart from the collector with a delivery flow rate of 3 mL/h under a fixed voltage of 7 kV at 1000 rpm. The fiber mats were stripped from the aluminum foil by submersion in Methanol followed by thorough washing using nanopure water.

### 4.2. Functionalization of Cellulose Acetate Electrospun Fiber Mat

As a strategy to activate the cellulose acetate fibers for its further activation with the biomolecules, chemical modification was performed. The fiber mats were deacetylated, then oxidized and afterwards submitted to the peptide coupling reaction. A brief scheme of the chemical nature of this process can be seen in Scheme 5.1.

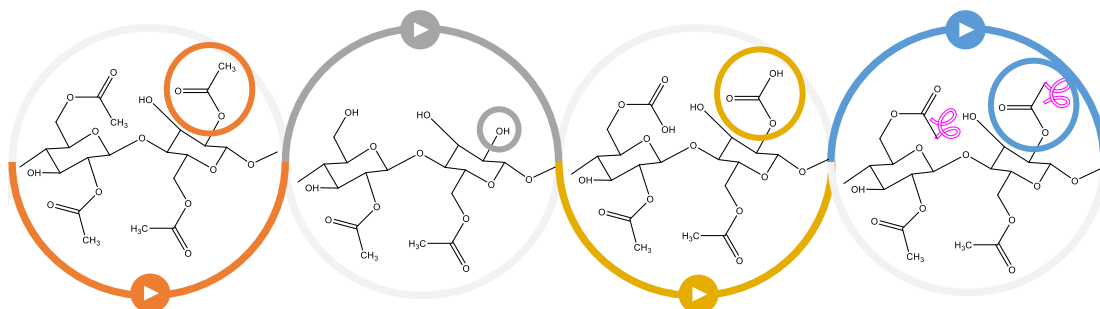
#### 4.2.1. Deacetylation

The fiber mats were deacetylated following well established procedures published elsewhere.<sup>69</sup> The degree of deacetylation was assessed using FTIR from 5-30 min. and 1-3 h. This process was optimized, and a period of 10 minutes was

selected for deacetylation using 0.2 M NaOH in 95% EtOH. The fiber mats were thoroughly washed with water before further use.

#### 4.2.2. TEMPO Mediated Oxidation

Then, the fibers are oxidized to allow the formation of carboxylic terminals for further bioconjugation. In brief, the fibers are oxidized membrane by mixing 0.0648g of NaBr and 0.059g of TEMPO in 100 mL of H<sub>2</sub>O along with  $\approx$ 20 mg of membrane. Then, 2 mL of a 12% NaOCl was added and the pH was fixed to 10. Afterwards the solution was left to react for 1 h on a shaker and the reaction was stopped by adding 20 mL of methanol and adjusting the pH to 7. The fiber mats were removed from the solution and washed thoroughly with water.



**Scheme 4.1** CA Modifications: (a) deacetylation, (b) oxidation and (c) peptide coupling

Figure 4.1 shows the final modification results. As can be seen in this figure, in the unmodified CA membrane, the hydroxide (-OH) band originally present at  $3500\text{ cm}^{-1}$  is broadened and shifted after modifications to  $3320\text{ cm}^{-1}$ . This may be due to the increase in H-bonding that occurs upon modifications since the stronger the H-bond, the longer the -OH bond and thus, the lower the vibrational frequency and broader and more intense will be the absorption band. However, the most important information regarding the modifications can be found within the carbonyl peaks. The first carbonyl peak observed belonging to the raw CA occurs

at  $1750\text{ cm}^{-1}$  due to the ketone (C=O) group of the acetate structure in CA. After deacetylation this band is lost and upon oxidation a new carbonyl band emerges at  $1610\text{ cm}^{-1}$  belonging to the carbonyl from the carboxylic acid (C=O).

It was also important to verify that the porosity and surface characteristics were retained and remained undamaged by the modification processes and thus SEM was employed prior to proceeding to the peptide coupling procedures. The images across the sequential modification of the fiber mats demonstrate that the processes did not damage the porosity of the fibers (Figure 4.2 a) as well as the fiber diameter (Figure 4.2 b). The fiber diameter was determined using Image J software from FIJI and obtaining 200 data sets to graph the histograms.

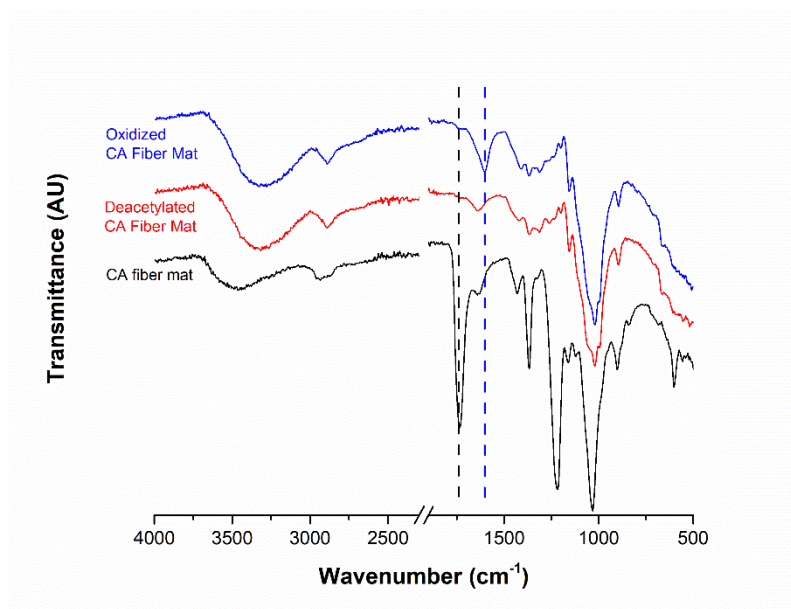


**Figure 4.1** FTIR of CA Fiber Mat (black) after Deacetylation (red) and Oxidation (blue)



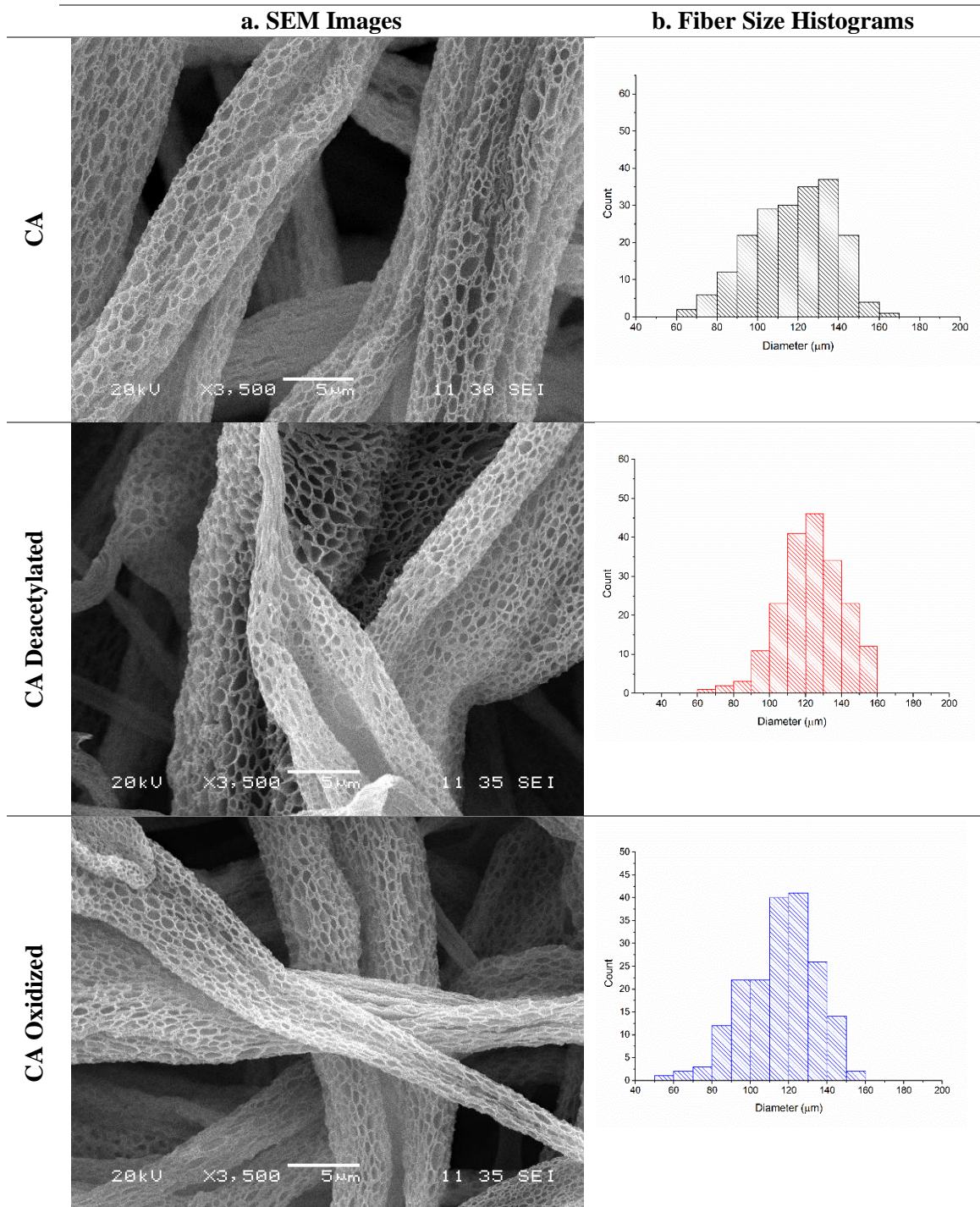


Figure 4.2 SEM Images and Fiber Size Histograms of CA with Deacetylated and Oxidized Modifications

### 4.2.3. Carbodiimide Crosslinking Chemistry

The bioconjugation technique used to activate the carboxylic acids to attach the selected peptides and attach the peptides was the EDC/Sulfo-NHS reaction. This reaction uses a reactive carbodiimide (EDC-HCl) and Sulfo-NHS catalyst which was used to conjugate the peptides KRSR, RGD and BMP-2 (Table 4.1) to the fiber mats. After testing different formulations, the chosen protocol was modified to our purpose which was achieved using a membrane size corresponding to approximately 18 mg with 7.2 mg of EDC, 19.8 mg Sulfo and 50 mL of Milli-Q nanopure water at a neutral pH.

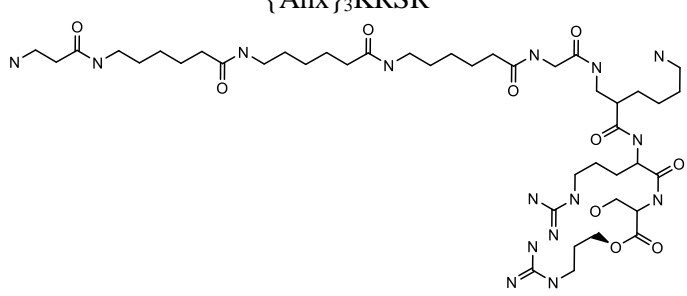
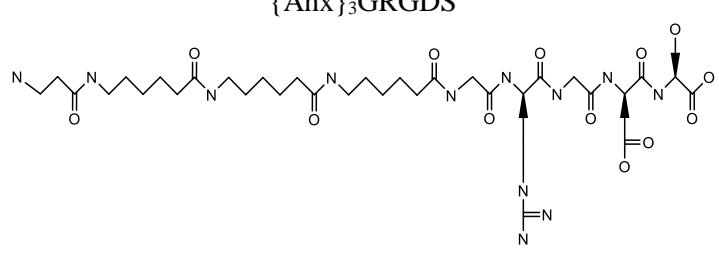
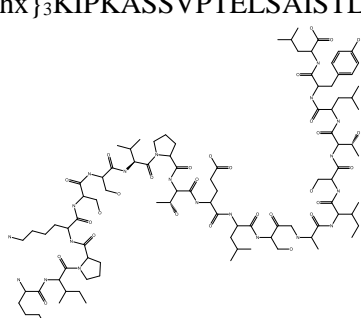
Peptide	Sequence and Structure
<b>KRSR</b> Glycosaminoglycan Binding Domain	$\{\text{Ahx}\}_3\text{KRSR}$ 
<b>RGD</b> Integrin Binding Domain	$\{\text{Ahx}\}_3\text{GRGDS}$ 
<b>BMP-2</b> Osteoinductive Growth Factor	$\{\text{Ahx}\}_3\text{KIPKASSVPTELSAISTLYL}$ 

Table 4.1 CA Coupled Peptide Structures

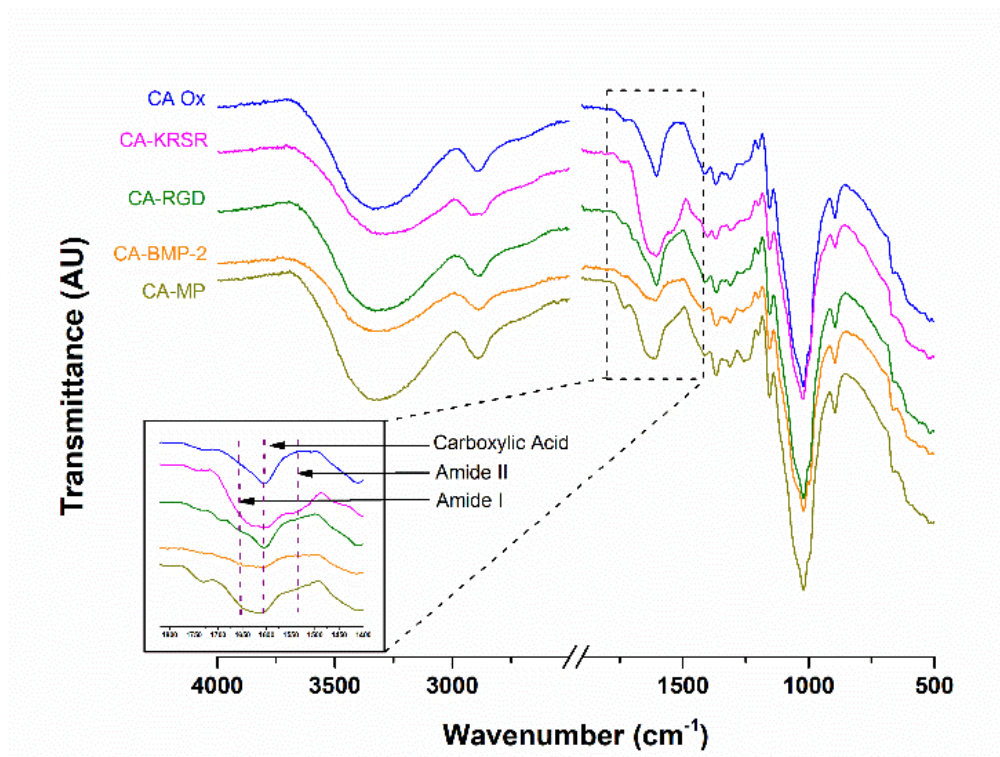


### 4.3. Characterization

#### 4.3.1. Fourier Transform Infrared Spectroscopy (FTIR)

After coupling the peptides CA-KRSR, CA-RGD, CA-BMP-2 and CA-MP (Figure 4.3), a change can be observed in the shape of the of amino acid side chains characteristic carbonyl bands around 1,700  $\text{cm}^{-1}$  (C = O, Amide I) and 1,540  $\text{cm}^{-1}$  (N – H Amide I). The carbonyl signals belonging to a carboxylic acid group usually occur between 1730 and 1700  $\text{cm}^{-1}$ ; however, these peaks are now shifted to lower frequencies due to the new membrane conjugations. In the CA-KRSR sample the amide band occurs at 1649  $\text{cm}^{-1}$  and 1604  $\text{cm}^{-1}$ , the CA-RGD at 1689  $\text{cm}^{-1}$ , the CA-BMP-2 at 1644  $\text{cm}^{-1}$ . An interesting weak band occurring at 2338  $\text{cm}^{-1}$  in the CA-RGD sample which corresponds to the region of a thiol (-SH) group. None of the peptides exhibit such group and this thiol may correspond to an impurity present from the peptide synthesis which matches the certificate of purity during manufacturing where the HPLC curve displayed 3 additional peaks. The only peptide coupled fiber mat with noticeable amide II signal corresponds to the CA-KRSR peptide which can be attributed to the presence of two Arginine amino acids in the structure allowing the vibration of this band. The FTIR Amide deconvolution for individual peptide couplings was also performed and can be appreciated in Figure 2 C.

A.



B.

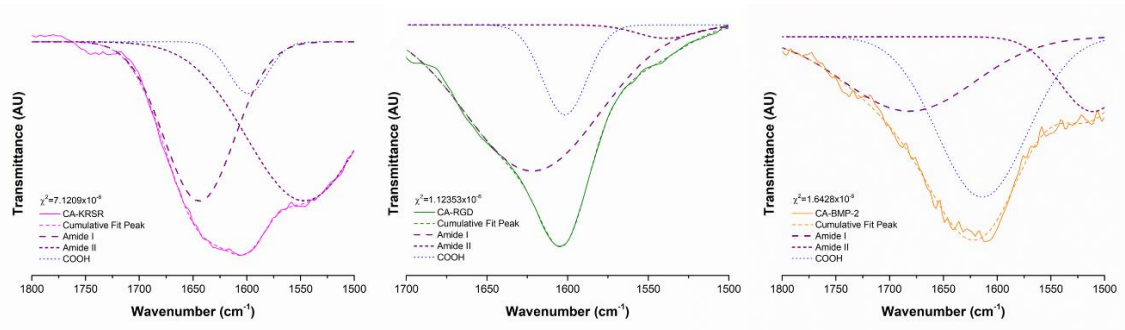


**Figure 4.3** FTIR spectra comparison of the (A) Individual Peptide Couplings KRSR (pink), RGD (olive), BMP-2 (orange) and d) Multi-peptide Coupling (dark yellow); and (B) Deconvoluted amide (purple) peaks using a Gaussian curve fitting function for CA-KRSR (pink), CA-RGD (olive) and CA-BMP-2 (orange).

#### 4.3.2. Scanning Electron Microscopy (SEM)

SEM microscopy was utilized to account for morphological changes in the fiber mats after chemical and biological modifications. The images across the sequential modification of the fiber mats demonstrate that the chemical modification of the cellulose acetate mats is not affected. After the biological coupling, the surface roughness is different although the porous nature of the mats is retained as can be observed in Figure 4.4 a. The porous structures in a scaffold are believed to be crucial for cell osteogenesis as they allow mass and fluid transport, cell adhesion and bone ingrowths. Micro-pore diameters in macrostructures, such as our fibers, are optimal for osteogenesis as they entrap dissolved  $\text{Ca}^{2+}$  and  $\text{PO}_4^{3-}$  ion concentrations in the pores and by doing so, decrease the shearing stress present in cells and proteins attached to macro-pore surfaces.<sup>70</sup> In the natural bone matrix, the coiled and crosslinked microfibrillar structures of collagen type I have a length of ~300 nm and a diameter of 1.23 nm.<sup>66</sup> In this work, the average diameter of the fibers is maintained between 100  $\mu\text{m}$  and 130  $\mu\text{m}$  and the micro-pore diameters range from 0.5  $\mu\text{m}$  to 1.5  $\mu\text{m}$  as can be seen in the histograms on Figure 4.4 b.

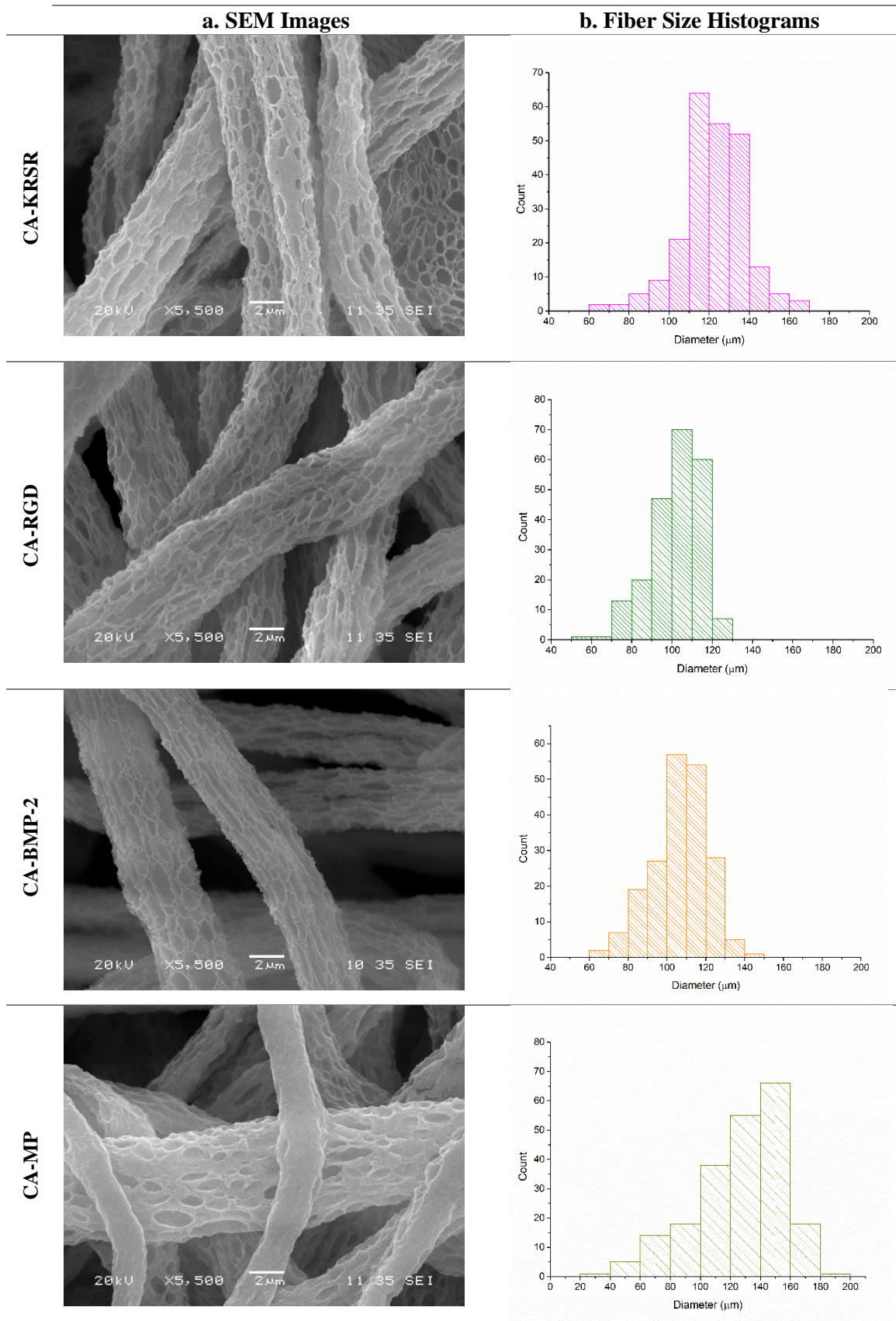


**Figure 4.4** a) SEM Images and b) Fiber Size Histograms of CA Fiber Mats after Peptide Couplings

#### 4.3.3. Thermogravimetric Analysis

TGA analysis was performed using LABSYS EVO STA from Setaram. In these experiments we ran a heating ramp from 20 °C to 600 °C at a 20 °C/second rate in Nitrogen gas with a balance purge of 10 mL/min. As can be seen in Figure 4.5 a, the CA membrane has an initial endotherm corresponding to the trace ethanol solvent loss beginning around 50 °C followed by water loss from 70 °C and evolving up to 140 °C. Afterwards, the beginning of the thermal decomposition at 230 °C can be observed, yet the rate of mass loss is largest at 370 °C for CA and Deacetylated fiber mats as can be seen in the DSC plot (Figure 4.5 b). The oxidized membrane presents a smaller thermal stability possibly due to the carboxylic acid components present in this structure. Decarboxylation process related to the depolymerization of the CA polymer occurs around 250 °C, hence, this explains the appearing shoulder in the DSC curve for the Oxidized fiber mat and afterwards in the peptide coupled mats.<sup>71</sup> The peptide coupled fiber mats share similar behavior with the distinction of the CA-KRSR membrane. This can be attributed to the presence of two Arginine (R) groups contributing a positive charge to the structure. It is suggested that the use of NaOCl in the oxidation reaction could have promoted a glycosidic bond degradation resulting in the appearance of the decomposition at a lower temperature. The fact that the DSC signals appear as bell shaped peaks at the TGA drop, proves that a simple decomposition process takes place instead of a spectrum of decomposition temperatures; the process observed does not involve any melting or sublimation transitions.<sup>72</sup> Total carbonization of the polymer in all fiber mats occurs after 350 °C meaning that the core structure of the CA polymer was retained independent of the modification performed.

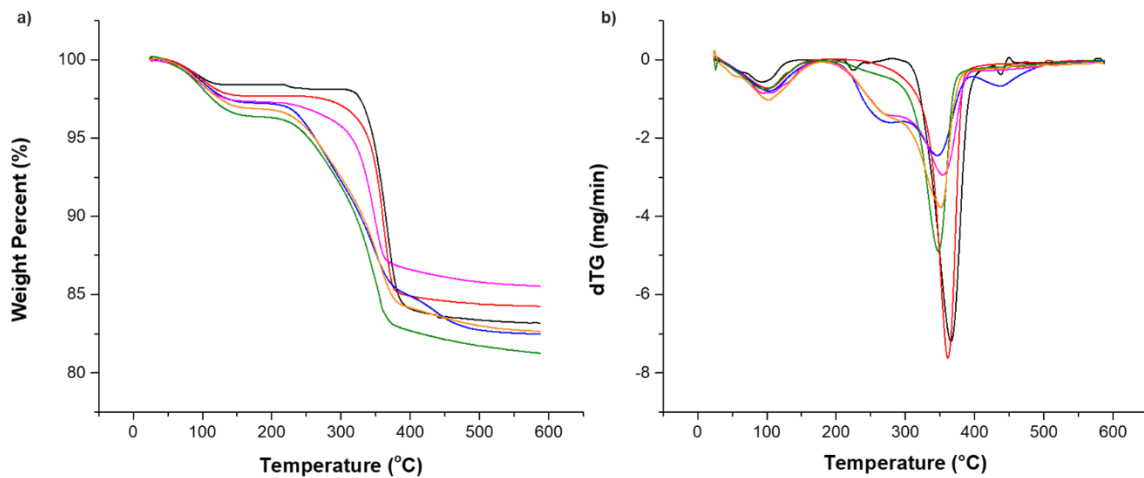


**Figure 4.5** a) TGA and b) DSC of CA (black) Deacetylated CA (red), Oxidized CA (blue), CA-KRSR (pink), CA-RGD (olive) and CA-BMP-2 (orange)

#### 4.4. Biological Assays

##### 4.4.1. Expression of $\alpha_v\beta_3$ integrin receptor

It is known that cellular adhesion to the surface of a biomaterial occurs by (1) attachment, (2) spreading, and (3) focal adhesion to promote a strong interaction; a process mediated by integrins.<sup>67</sup> Given that adhesive proteins attach to the integrin receptors on osteoblast fiber mats, and the  $\alpha_v\beta_3$  integrin receptor is one of the primary RGD binding domains, the expression of this receptor was studied next. Prior to performing this assay, the presence of the  $\alpha_v\beta_3$  protein in our cell lines was corroborated using Flow Cytometry.

##### 4.4.1.1. Flow Cytometry (FC)

Cells were physically detached from the culture flask using a scraper and washed with Fluorescence-activated cell sorting (FACS) buffer (PBS with BSA and  $\text{NaN}_3$  at 0.05 %). After cell counting,  $1 \times 10^6$  cells in 100  $\mu\text{L}$  were added to microtubes in FACS buffer to minimize non-specific binding of antibodies.

Previously prepared primary antibody Anti-Integrin alpha V beta 3 antibody [BV3] at a 1:50 dilution in FACS was added as 5  $\mu$ L to the cell containing microtubes and they were left in ice. After 30 mins, the microtubes were washed with FACS and centrifuged 3 times at 400 G for 5 mins. Superclonal secondary antibody Alexa Fluor 555 Goat Anti-Mouse IgG (H+L) was added and after another 30 mins incubation they were washed again with FACS. To analyze in FC, the cells were resuspended with 200  $\mu$ L FACS. The FC results can be seen in Figure 4.6.

The experimental sample shows that 53.2% of the cells were expressing the  $\alpha_v\beta_3$  integrin receptor (Figure 4.6 f). The culturing method of the cells involves the use of Trypsin-EDTA to detach the cells from the walls of the flask and it is known that the proteolytic activity of trypsin may harm cells by cleaving the growth factor receptors or membrane proteins.<sup>73</sup> Most cells recover their surface proteins after 24 hours but some are not reversible and it is possible that during the cell passages previous to performing the experiment, this integrin was detached from the cells.

It is possible that the population differences (as shown in Figure 4.6 a) could've been differences between the progenitor states and differentiated states of the osteoblasts and the chosen population was not representative of the whole expressing the receptor. However, corroborating the presence of the integrin receptor and this was achieved, and the expression of this integrin was studied against the CA fiber mats and their peptide treatments.



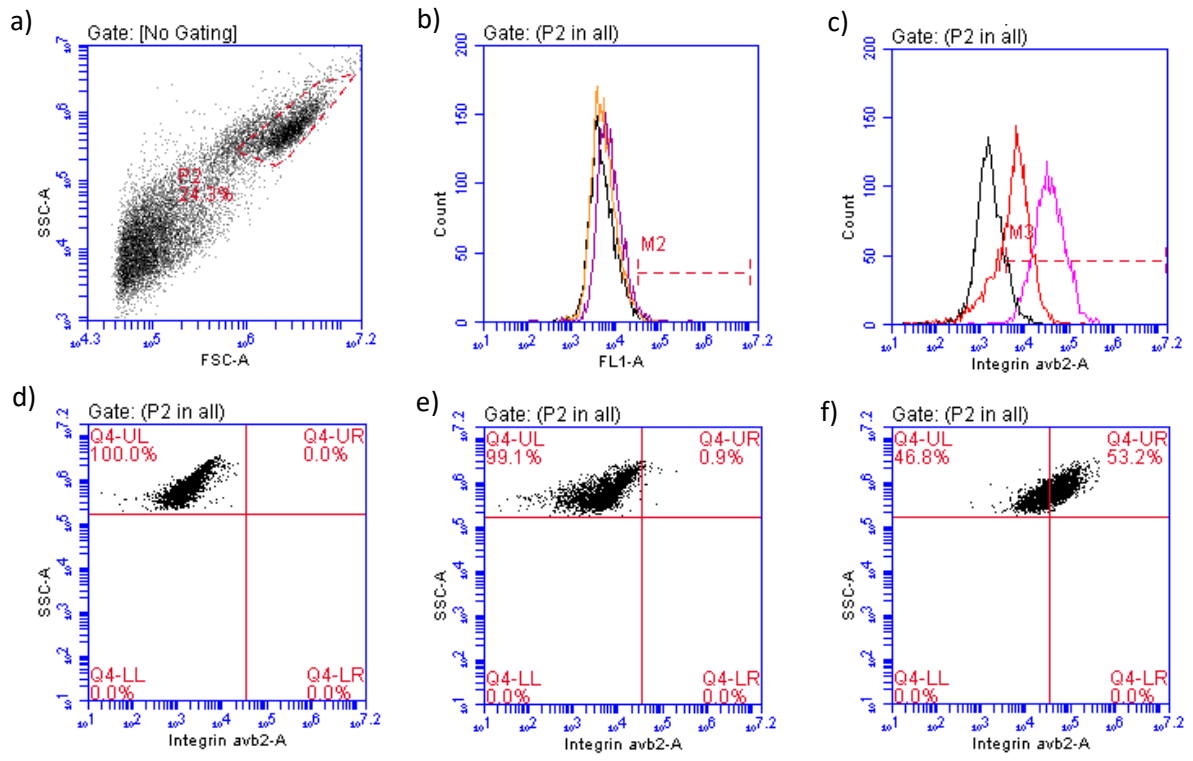


**Figure 4.6** Flow Cytometry of hFOB 1.19 a) Population Chosen, b) Control Fluorescence, c) Antibody Fluorescence, d) Untreated Control, e) Secondary Only Control and f) Antibody Treated Cells



#### 4.4.1.2. Microscopy Images of the $\alpha_v\beta_3$ Integrin Receptor

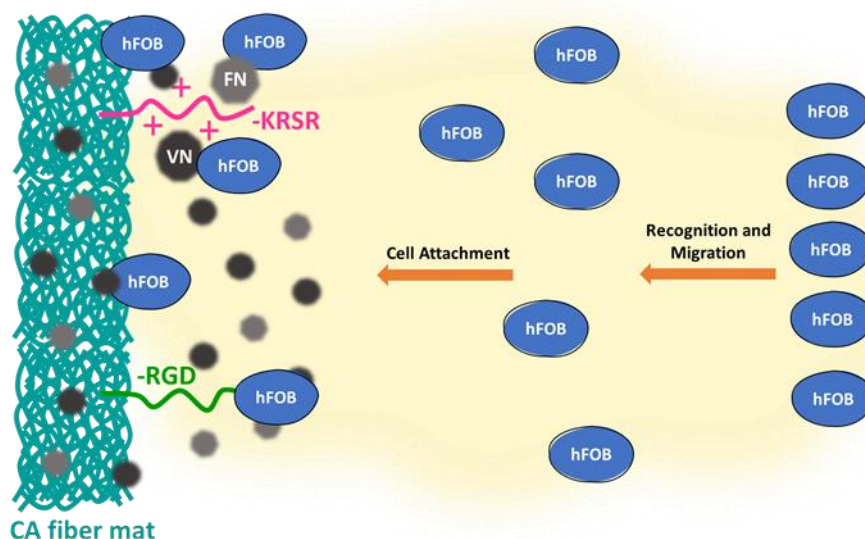
The cells were cultured for a period of 7 days, with culture medium replaced every other day. Firstly, the cells were fixed with Paraformaldehyde (4% in PBS) and rinsed in triplicate with PBS after 15 mins. Following this step, the cells were permeabilized with Triton-X100 (0.1% in PBS) for 15 mins and washed with PBS again. To block antibody binding to non-specific sites, a Goat Serum (2% in PBS with sodium azide) solution was added for 1 h. Upon removal, the cells were incubated with Anti-Integrin alpha V beta 3 antibody [BV3] (1:500) and placed overnight in a wet chamber at 4°C. After incubation with the primary antibody, the cells were washed with PBS a total of 4 times and 10 minutes and subsequently incubated in dark for 1 h with Polyclonal Alexa Fluor 488 AffiniPure Goat Anti-Mouse IgG (H+L) secondary antibody (1:500) and Phalloidin-iFluor 647 Reagent (1:500). Lastly, the samples were washed 4 times with PBS for 10 mins and mounted on 24 × 60 mm coverslips with ProLong Diamond Antifade reagent containing 4', 6-diamidino-2-phenylindole (DAPI) and left in the dark at room temperature until microscope analysis.

As can qualitatively be seen in Figure 4.7, the background reduced CA and CA-MP (Figure 4.7 a and e respectively) images showed a high expression of the integrin receptor. Another observation is that the KRSR peptide (Figure 4.7 b) appears to induce cellular aggregation. The major difference between adhesive RGD and KRSR peptide relies on KRSR having three out of four amino acids positively charged to bind to the negatively charged HS on glycosaminoglycans. Zhang and Webster indicate that there is a strong electrostatic attraction between negatively charged proteins (i.e., fibronectin and

vitronectin) and positively charged surfaces.<sup>74</sup> Similar behavior was observed by Chen et al. evaluating osteoblastic actin microfilament arrangement on KRSR-modified surfaces.<sup>75</sup> This implies that the incorporation of positive charges in surfaces can favor preosteoblast adhesion. However, it is also a possibility that the distribution of KRSR peptide throughout the fiber mat was not homogeneous, and cells attached preferably to the KRSR binding sites.

Contrary to what was expected, the number of cells present in the CA-RGD (Figure 4.7 c) fiber mat on most images was lower than in the unmodified CA sample. It is important to distinguish that the adhesive proteins from the culture medium attach to the substrates of biomaterial surfaces in study (in this work, the CA fibers) and cells attach to those adsorbed proteins on the biomaterial surfaces. Hennessy et al. explains that the presence of RGD peptides in combination with adsorbed endogenous proteins might contribute to diminished cell attachment because their presence disrupts the conformations of adsorbed Fibronectin (FN) and Vitronectin (VN) or because the presence of the RGD peptides blocks the adsorption of endogenous proteins.<sup>76</sup> In this sense, even though RGD peptides have been used to support cell attachment, migration and differentiation, they reduce binding affinity compared with the same peptide

existing as part of its parent protein structure.<sup>77</sup> A representation of these hypothesized interactions can be seen in Scheme 4.2.



*Scheme 4.2 Hypothesized Peptide Interactions and Effect on Cellular Attachment Preference*

The peptides just discussed (KRSR and RGD) were coupled to stimulate cellular adhesion and similarly, the fiber mat treated with BMP-2 peptide growth factor showed lesser cells against other treatments (Figure 4.7 d). It is known that BMPs have significant effects on human osteoblast cells between 10 and 1000 pg/ml in vitro.<sup>78</sup> However, it is important to note that the effect of the concentration of natural BMP-2 is not necessarily equal, to the effect of peptide concentration. And, since the real concentration of peptide present in the fiber mats is unknown, the low number of cells could be due to the concentration of the peptide in the fiber mat being too high inducing a contrary and toxic response to the cells. Saito et al. studied the activation of osteo-progenitor cells by the BMP-2 synthetic peptide corresponding to the knuckle epitope of BMP-2, the same sequence used in this study, and found that when co-cultured alongside rh-

BMP-2 parent protein, the fluorescence exhibited by the cells with the peptide alone disappeared.<sup>79</sup> This could mean that the absence of the synergy domains of BMP-2 in the peptide leads to poor osteoconduction. In our study, after comparing fluorescence intensity (Figure 4.8), the CA-BMP-2 sample was the only significant value against untreated CA Fiber Mat and showed the highest fluorescence intensity signal while the number of nuclei (49) was lesser than in the other fiber mats. Likewise, the CA-MP Fiber Mat had the highest number of cells (255) while its fluorescence intensity was the lowest.

Integrins, like  $\alpha_v\beta_3$ , are constantly switching between inactive bent and active extended conformations responsible for adhesion initiation after ligand binding.<sup>80</sup> The crucial step in integrin activation is considered to be the binding of intracellular proteins, such as talins and kindlins, to the tail of  $\beta$ -integrins who cluster into focal complexes for attachment while inactive integrins are usually found disordered across the cell or dorsally.<sup>81</sup> Overall, integrin activation involves a series of steps that include conformational changes, engagement with extracellular ligands, connections with the actin cytoskeleton, clustering to form focal adhesions and signal transductions all leading to integrin inactivation which occurs by Ser/Thr phosphorylation of the talin and kindlin binding motif (NPXY).<sup>82-83</sup> Inactive integrins diffuse rapidly in the plane of the membrane because focal adhesions disassemble to recycle integrins and permit new adhesion sites.<sup>84</sup> By analyzing the distribution and quantity of  $\alpha_v\beta_3$  integrins present, we can suggest that the fluorescence intensity is indirectly proportional to the integrin activity and thus the Fiber Mat treatment which activated  $\alpha_v\beta_3$  to a larger degree corresponds to CA-MP followed by untreated CA. Additionally,

it is possible that the incorporation of the BMP-2 peptide does not activate the  $\alpha_v\beta_3$  integrin considering that the purpose of its incorporation was not for adhesion but for later maturation. A concluding remark with certainty towards integrin activation evaluation cannot be offered with this data. A more accurate method to determine such information would be to use an active/inactive antibody that is specific for this integrin or a variation of  $\alpha_v\beta_3$  secondary antibody that could be used with a phosphorylation tag.

It is important to also acknowledge that the definite concentration of the peptides present in the CA fiber mats as an unknown variable and that it is also possible that there was a competition between all three peptides to couple to the fiber mats in the CA-MP sample; which could explain why qualitatively there were more cells found in this fiber mat. Yet, to attribute the increased expression observed in CA-MP to either one of the peptides, would be incorrect.

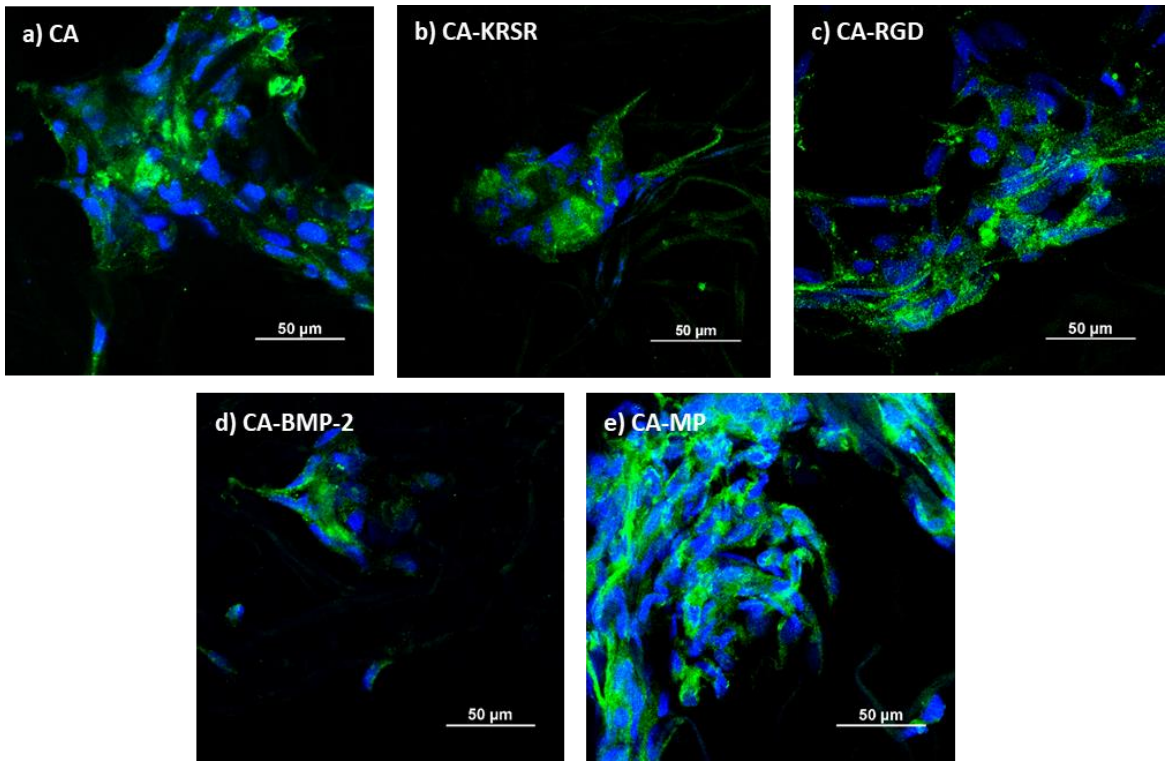


**Figure 4.7**  $\alpha_v\beta_3$  integrin expression (green) in hFOB 1.19 (blue nuclei) across each CA electrospun mat (a) CA Fiber Mat, (b) CA-KRSR, (c) CA-RGD, (d) CA-BMP-2, and (e) CA-MP. Scale bar represents 50  $\mu\text{m}$ .

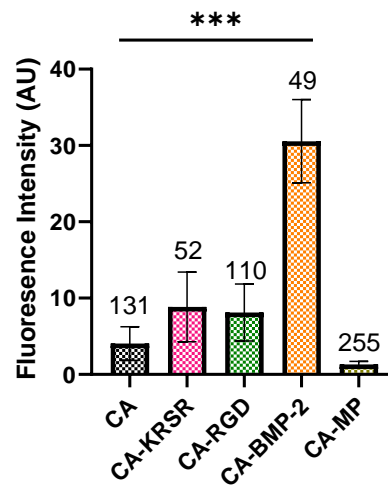


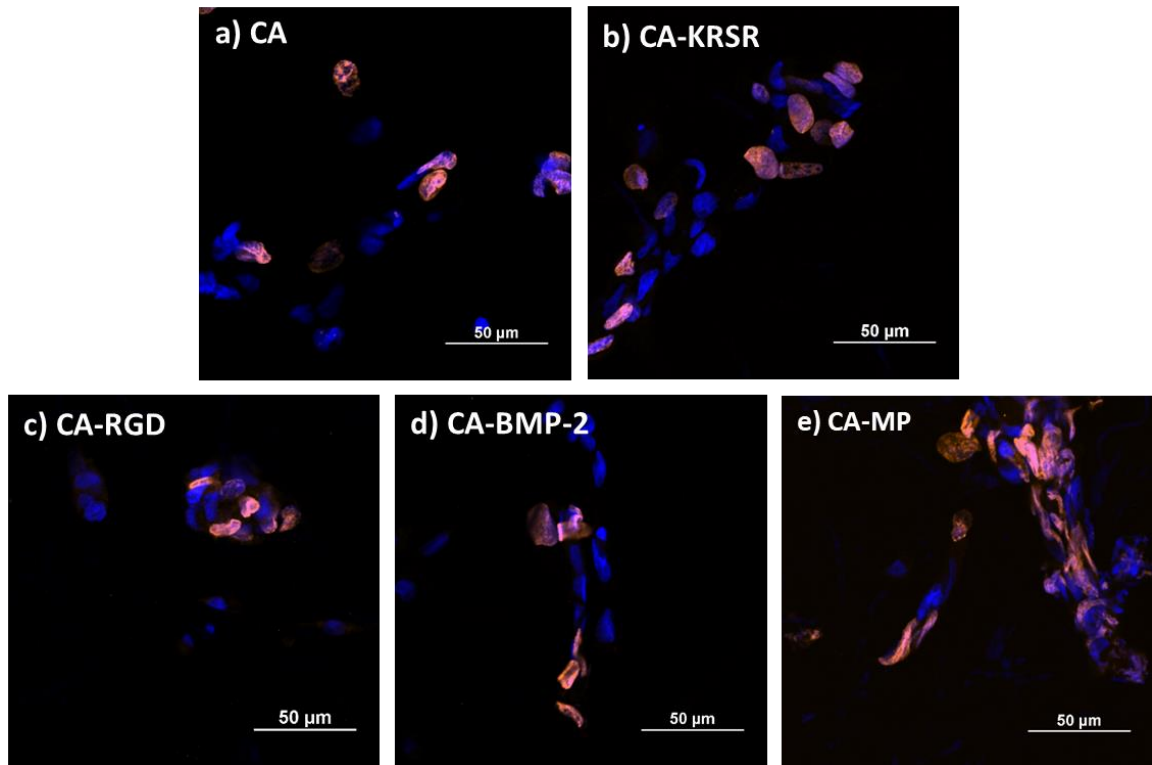
**Figure 4.8** Fluorescence Intensity Across Fiber Mat Treatments Normalized by the Total Cells Displayed Over Each Column Respectively.

#### 4.4.2. BrdU Proliferation Assessment

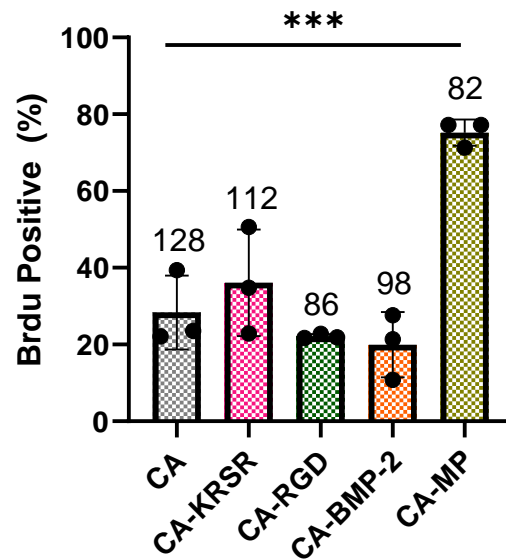
5-Bromo-2'-deoxyuridine, BrdU was used to evaluate the proliferation of the cells. BrdU is a thymidine analog that is incorporated into the cell DNA at the S phase of cell cycle and allows us to determine how many cells are reproducing. Cells were seeded at 50,000 cells per well in contact with the fiber mats for 48 hours. After incubation, DMEM was removed from each well and a 10  $\mu$ M BrdU solution in DMEM was added and incubated for 6 h. The BrdU solution was removed from each well and the fiber mats were rinsed with PBS for 1 min. Afterwards, the cells were fixed with Paraformaldehyde (4% in PBS) and rinsed in triplicate with PBS after 15 mins. Then, the cells were permeabilized with Triton-X100 (0.1% in PBS) for 15 mins and washed with PBS again. Following this step, for the purpose of denaturing the DNA, HCl at 0.05 N was added for 1 hour and rinsed with PBS for 5 minutes. A Goat Serum (2% in PBS with sodium azide) solution was added for 1 h to block antibody binding to non-specific sites and when removed, the cells were incubated with Anti-BrdU solution (1:5) and placed overnight in a wet chamber at 4°C. The next day, the solution was removed from the well plates and the fiber mats were rinsed 3 times with PBS for 10 minutes. After rinsing, polyclonal Alexa Fluor 594 AffiniPure Goat Anti-Mouse IgG (H+L) secondary antibody (1:500, Jackson Immuno Research) was added and left in the dark at room temperature for 1 h. Lastly, the samples were washed 3 times with PBS for 10 mins and mounted on 24  $\times$  60 mm coverslips with ProLong Diamond Antifade reagent containing 4', 6-diamidino-2-phenylindole (DAPI) and left in the dark at room temperature until microscope analysis.

Figure 4.9 presents some images of the BrdU assay where the total number of nuclei present can be seen by the blue DAPI staining including the BrdU incorporated nuclei seen with orange overlaps. The total number of BrdU positive cells was adjusted by the total number of cells present in each sample and expressed as percentages in Figure 4.10. Values represent mean  $\pm$  standard deviation (SD) from three replicates. Triple asterisk indicates statistical significance against untreated CA fiber mat sample ( $p < 0.0002$ ). The total amount of cells that attached to the fiber mats can be seen in Figure 4.10 above each column where it is suggested that the low number is due to the following reasons: (1) the cultured cell concentration was too low to be significant in (2) a 3-dimensional scaffold where the focusing could miss other nuclei present at a different focal lengths as per described in the acquisition methodology used. Examining cell proliferation by itself in a period of hours is not a mere indicator of the bioactivity of a material unless complimented with other assays. Other possible explanations that justify lower than expected cell numbers and proliferation was discussed in the previous adhesion assay analysis as well.





**Figure 4.9** hFOB 1.19 BrdU cell proliferation assay against each CA electrospun mat. Blue nuclei represent total cells and orange overlaps represents the BrdU incorporated nuclei in (a) CA Fiber Mat, (b) CA - KRSR, (c) CA - RGD, (d) CA -BMP-2 and (e) CA-MP. Scale bar represents 50  $\mu\text{m}$ .



**Figure 4.10** a) Percentage of BrdU Positive Cells in each Fiber Mat Treatment and b) Total Number of Cells Present in each Fiber Mat Treatment

#### 4.4.3. Maturation Assessments

The cell culture incubation time was extended to a period of 14 days to study the expression of maturation markers such as Collagen and Bone Sialoprotein (BSP) as these are secreted from the cells when they are in the process of forming the bone matrix. For this assessment the cells were cultured following the same previously mentioned procedure. For these specific assays, 75,000 cells were seeded per well to avoid overlapping fluorescence and the culture medium was replaced every other day until fixation.

##### 4.4.3.1. Collagen Expression

Collagen is an indicator of osteoblast differentiation as these cells secrete large amounts of type I collagen (with small quantities of matrix organizing proteins that include osteocalcin and osteopontin).<sup>85</sup> Initially, bone collagen is secreted as a propeptide, that when cleaved, the molecules assemble to form fibrils. The immunocytochemical procedure was performed in the same manner as the previous performed for  $\alpha_v\beta_3$  integrin with the distinction of the primary antibody Anti-Collagen I antibody and secondary Alexa Fluor 488 Goat Anti Rabbit IgG (H+L) at (1:500) with Phalloidin-iFluor Reagent 647 (1:500).

Results shown in Figure 4.11 display the abundance of collagen fibers according to representative images from quantitative data shown in Figure 4.13. The CA-KRSR sample displayed cellular aggregation just like in the results seen in Figure 4.7 b; yet the control plate (Figure 4.12) showed a larger network of collagen evenly distributed across the sample. This could be due to the previously discussed reasoning implying that native proteins attach to the fibers

while the peptides are continuously washed away with each medium replacement; and specifically, the KRSR peptide has a positive charge to which we could attribute the preference of serum proteins to attach to the CA Fibers over the peptides. Figure 4.13 shows quantitative results obtained from fluorescence intensity values and normalized by the total number of cells found in the images used for obtaining intensity values. There was no significant difference found between any of the treatments. In this experiment, the conjugation of the peptides is not promoting long term effects over differentiation and maturation.

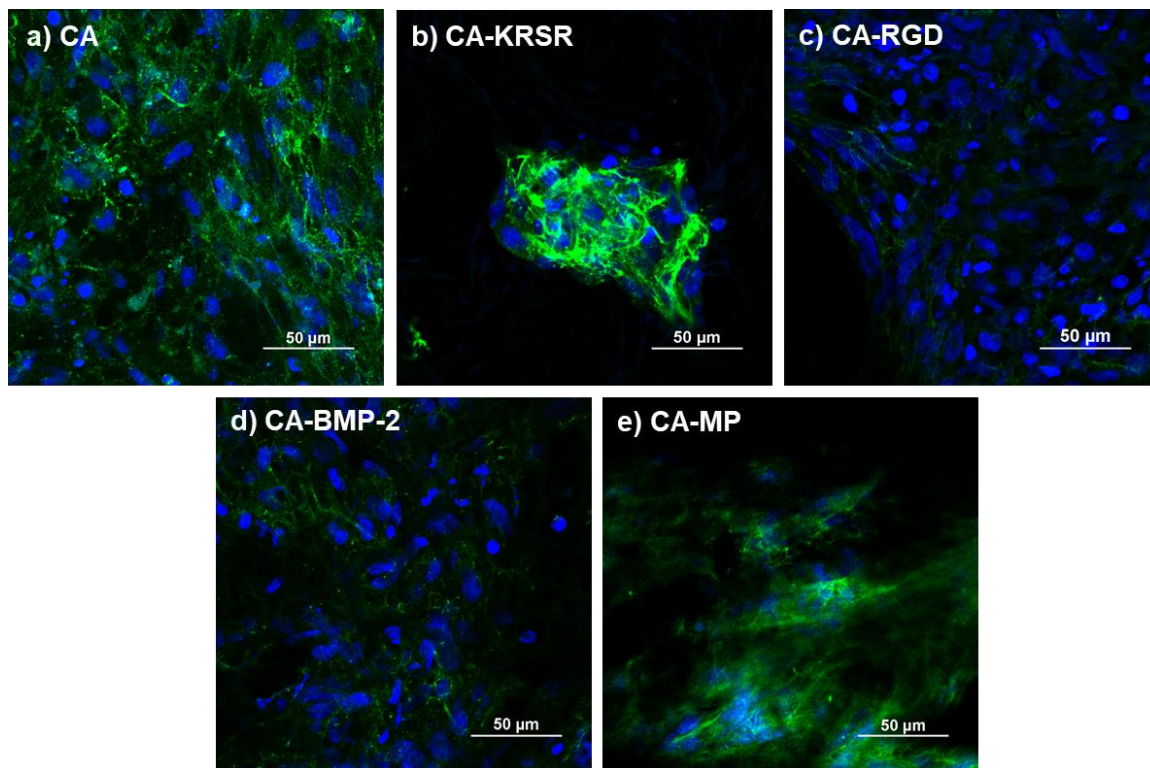


**Figure 4.11** Collagen I (green) assay for hFOB 1.19 (blue nuclei) across each CA electrospun mat (**a**) CA Fiber Mat, (**b**) CA - KRSR, (**c**) CA - RGD, (**d**) CA - BMP-2. Scale Bar Represents 50 μm.

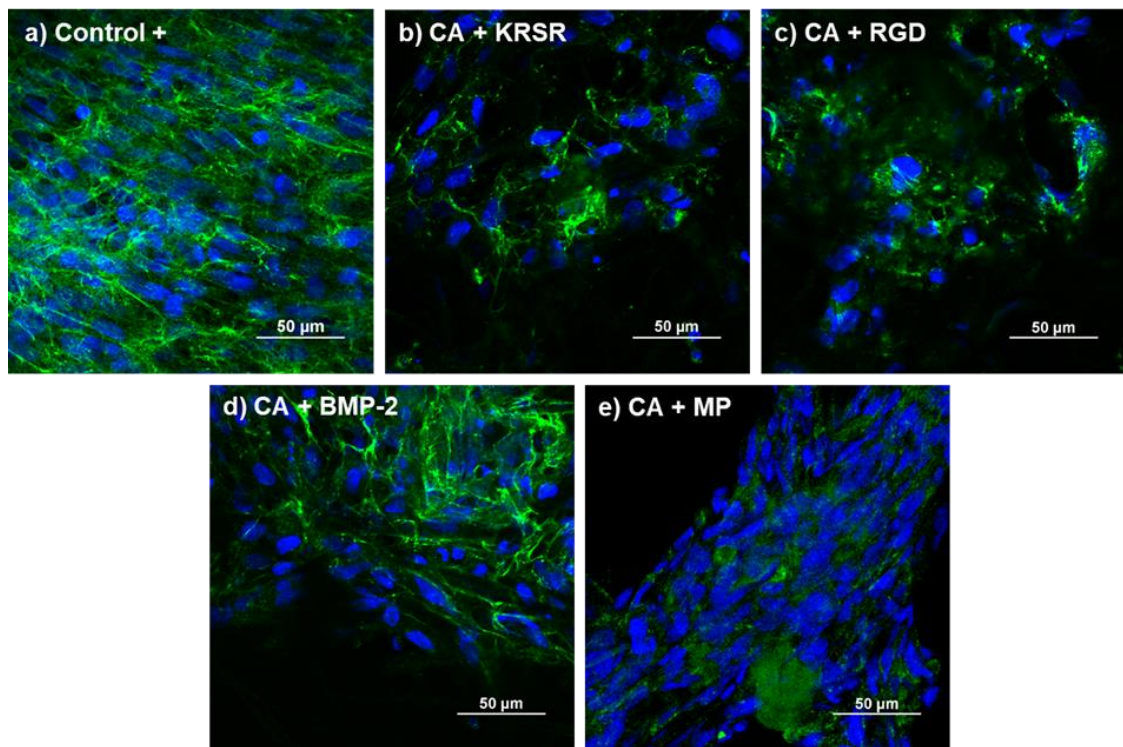


**Figure 4.12** hFOB 1.19 Expression of Collagen I (green) in a) Positive Disc Control, b) CA + KRSR, c) CA + RGD, d) CA + BMP-2 and e) CA + MP in DMEM. Scale bar represents 50 μm

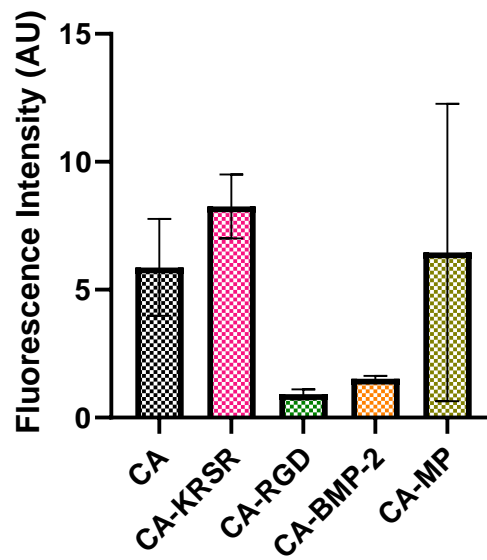


**Figure 4.13** Alexa Fluor 488 Fluorescence Intensity plot normalized by the number of cells for collagen expression. Error bars represent the standard error of the mean.

#### 4.4.3.2. Bone Sialoprotein (BSP)

Osteoblast differentiation can also be assessed by the deposition of  $\text{Ca}^{2+}$  and  $\text{PO}_4^{3-}$  minerals who form the mineral matrix of hydroxyapatite. Bone sialoprotein (BSP) binds tightly to hydroxyapatite crystals which are deposited in the gaps between collagen fibers. This assay provides important information about the cell-matrix interaction. The immunocytochemical procedure was performed in the same manner as the previous performed for  $\alpha_v\beta_3$  and collagen expression with the distinction of the primary antibody Anti-Bone Sialoprotein antibody and secondary Alexa Fluor 488 Goat Anti Mouse IgG (H+L) at (1:500) with Phalloidin-iFluor Reagent 647 (1:500).

Results in Figure 4.14 show evidence of BSP expression adjusted relative to quantitative fluorescence intensity data throughout all the fiber mats. The BSP expression is homogeneous across the fibers in all the samples and thus, the fibers provide good surface morphology for osteoblastic cell proliferation and maturation. Although not as notable as in Figure 4.14, the control samples with the peptides in solution (Figure 4.15) also demonstrated evidence of BSP expression. The CA-KRSR fiber mat (Figure 4.14 b) continues showing cellular aggregation; yet the cells continue to grow and form new matrix. Reasons for this behavior were discussed previously. Similar to the previous Collagen assay, the quantitative data representing the fluorescence intensity plot normalized by the total cells found in the images used for obtaining intensity values (Figure 4.16) did not show significant differences across either Fiber Mat treatment, sustaining the previous statement about long term effects of peptide couplings.

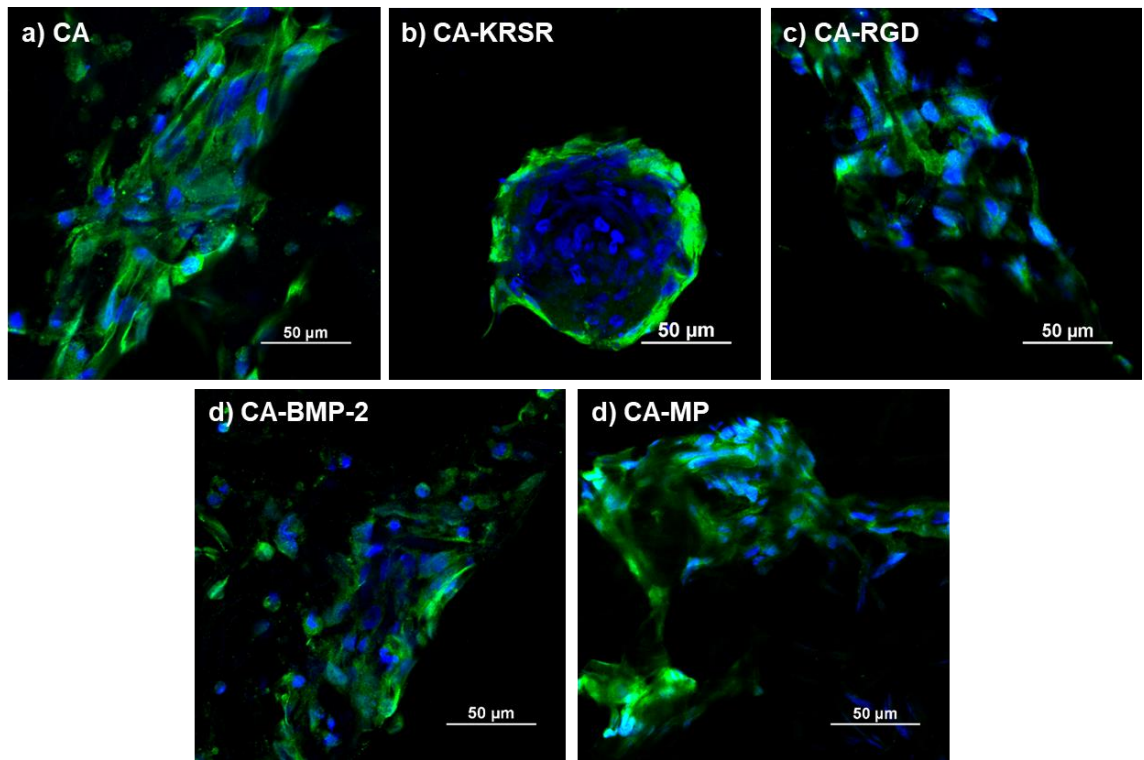


**Figure 4.14** Bone Sialoprotein (green) assay for hFOB 1.19 (blue nuclei) across each CA electrospun mats (a) CA Fiber Mat, (b) CA - KRSR, (c) CA - RGD, (d) CA - BMP-2 and (e) CA-MP. Scale Bar Represents 50  $\mu\text{m}$ .

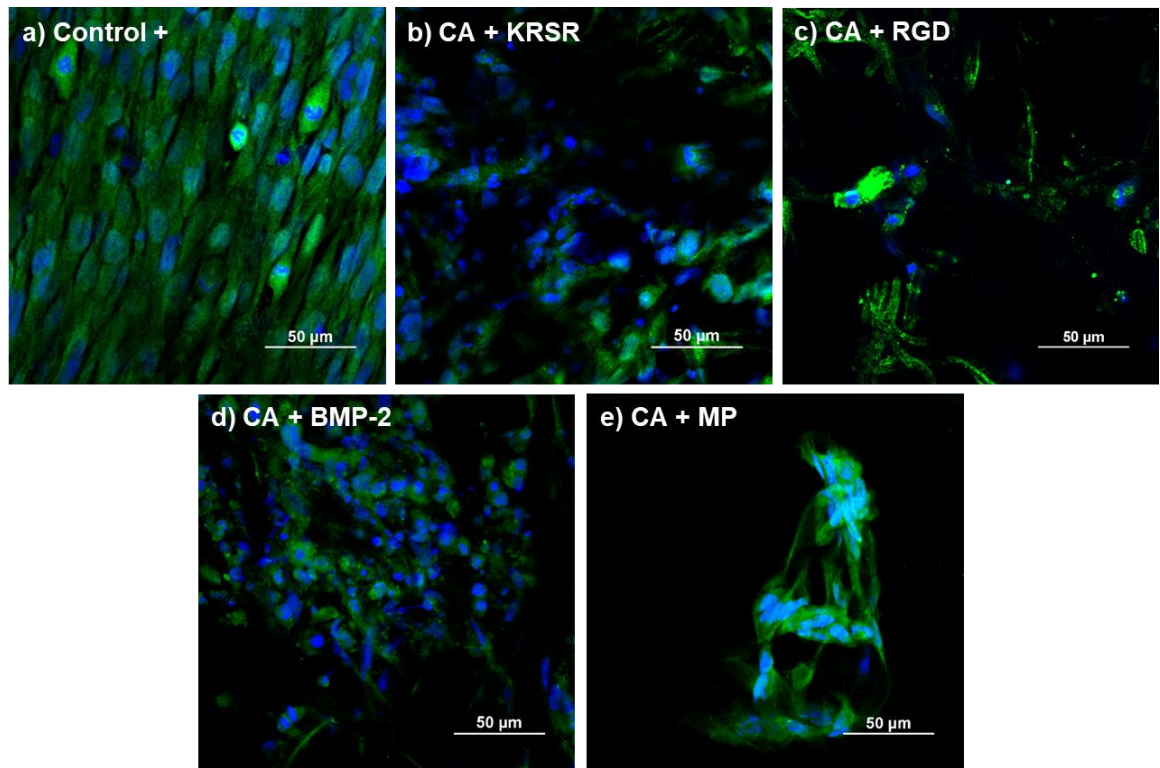


**Figure 4.15** hFOB 1.19 Expression of BSP (green) in a) Positive Disc Control, b) CA + KRSR, c) CA + RGD, d) CA + BMP-2 and e) CA + MP in DMEM. Scale bar represents 50  $\mu\text{m}$ .



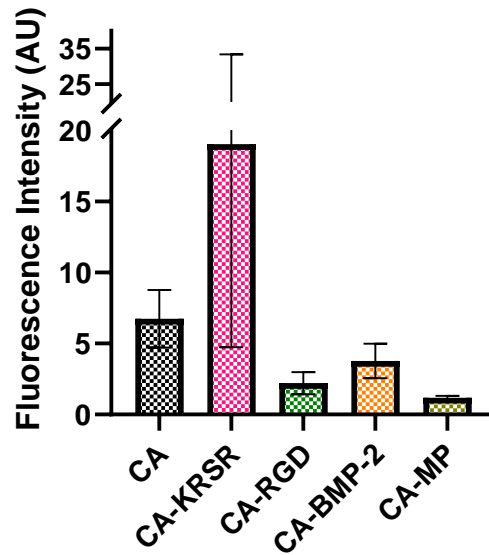


**Figure 4.16** Alexa Fluor 488 Fluorescence Intensity plot for BSP expression normalized by the total cells. Error bars represent the standard error of the mean.

#### 4.4.4. Cellular Morphologic Assessment

As stated in Chapter 2, osteoblastic cell lines are adherent cell types. As described in 4.4.3.1 the immunocytochemical procedure included the addition of Phalloidin 647 iFluor Reagent together with GAM 488 secondary antibody for the purpose of staining the cellular actin filaments that allow the assessment of the cytoskeleton morphology. As seen in Scheme 1.2, if the osteoblastic cell lines are not able to adhere to a substrate, then they will become apoptotic. The morphology of the cells in the Fiber Mats (Figure 4.17 and 4.18) indicate that there is no effect of the peptide presence against the cellular cytoskeleton. The same extended shape that is seen in the untreated membrane is repeated throughout all samples. In a 2D culture system (i.e. glass discs) the morphology of the osteoblastic lines appears as elongated and flat linear shapes; but the morphology is interpreted differently in a 3D system such as this one. The elongation of the cells is dependent of the fibrous

arrangement in which the cell is adhered. Since the fibers in the mats are not oriented in a specific direction, the shape of the cells will surround the shape of the fibers.

For this assesment, SEM-EDS was also employed as a complimentary technique to evaluate the fillipodia formation of the cells. To study the morphology of the cells by SEM, after a 14-day incubation period, the cells were fixed with glutaraldehyde and stored at 4°C overnight. After removing the Glutaraldehyde, they were rinsed three times with PBS for 10 min. The fiber mats were washed in a series of EtOH solutions beginning at 10%, 20%, all the way up to 90% for a period of 10 min each and finishing with three washes at 100%. The cells were chemically dehydrated by HMDS by rinsing in pure HMDS/EtOH ratios of 1:3, 1:1 and 3:1 for periods of 10 min and finishing with triple HMDS washes and overnight evaporation of HMDS filled well. They were gold coated (12 nm) and examined at x500 and x2500 magnifications using a High Resolution JSM-IT500HR Scanning Electron Microscope with electron beam energy of 20 kV. Figure 4.19 shows evidence of anchoring activity from the cells to the Fiber Mats through the presence of extended filopodia. Because the maturation of the cells leads to collagen formation where hydroxyapatite crystals are deposited, Electron Dispersive Spectroscopy (EDS) was employed with SEM to check for mineralization evidence. Evidence of bone crystals was found in the spheric protuberances whose composition included Calcium and Phosphorous corroborated elements (Figure 4.20).



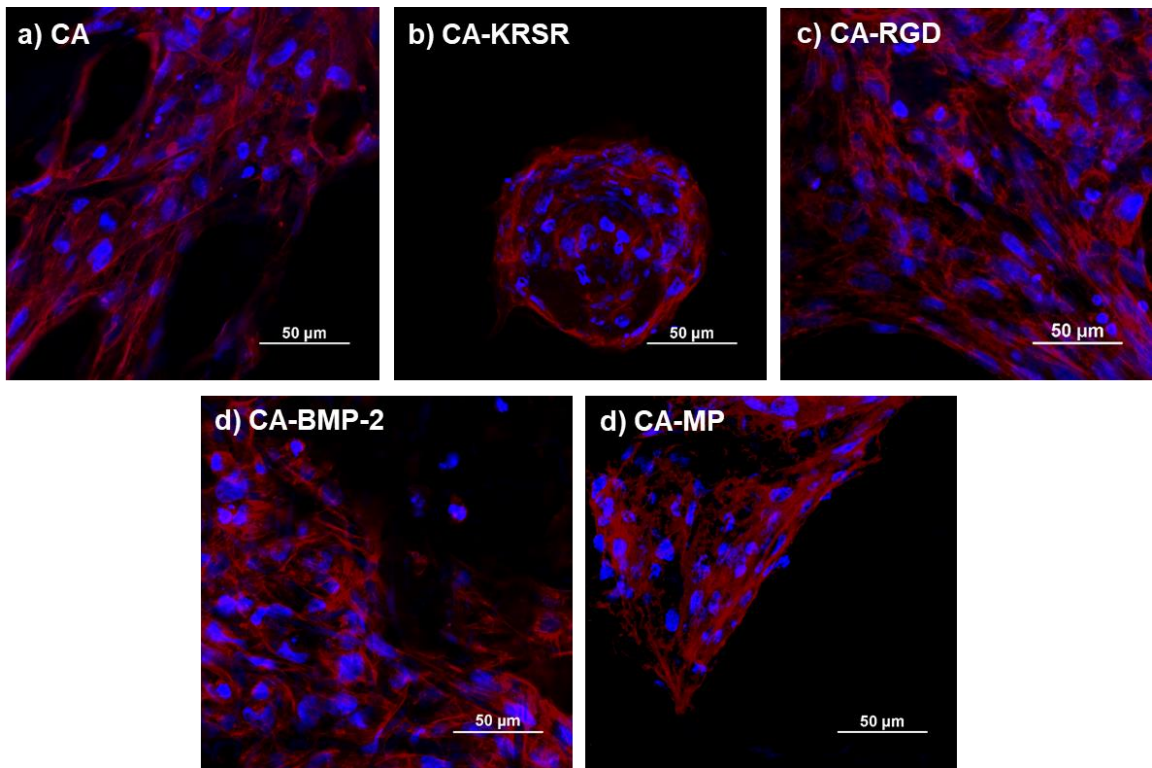


*Figure 4.17 Phalloidin Stained hFOB 1.19 Cytoskeleton at 14 days from BSP Assay. Scale Bar Represents 50 μm.*

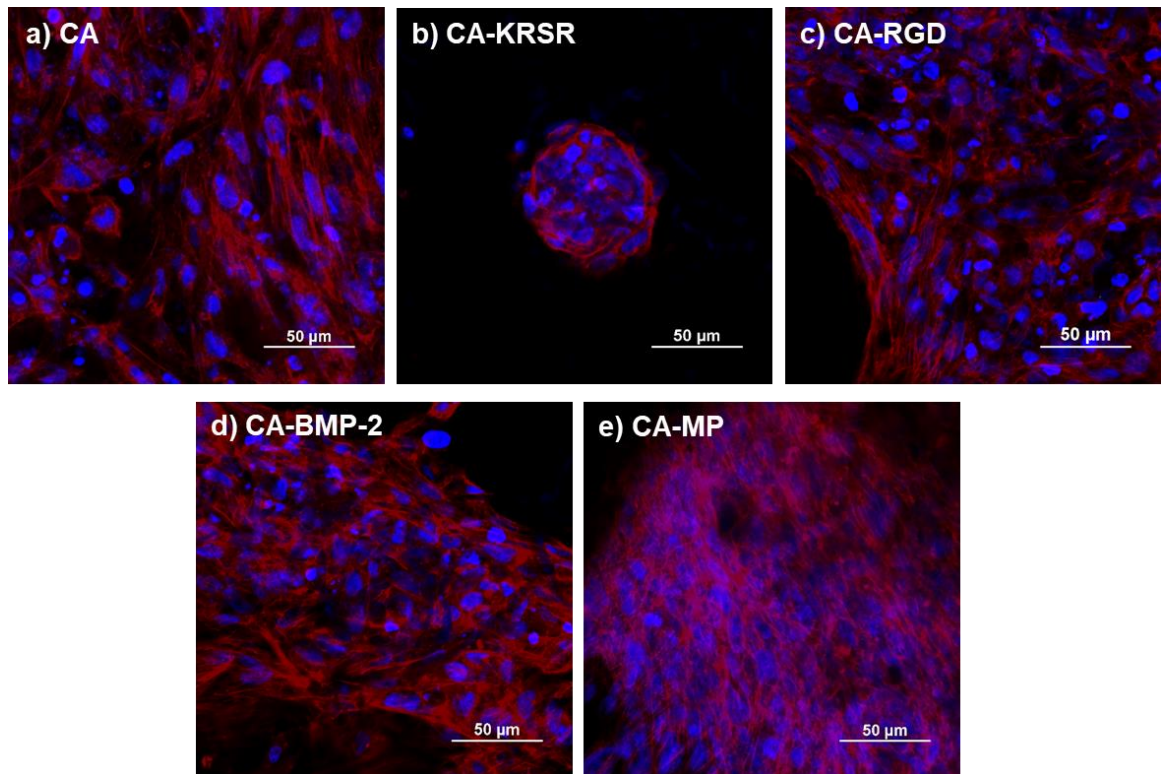


*Figure 4.18 Phalloidin Stained hFOB 1.19 Cytoskeleton at 14 days from Collagen Assay. Scale Bar Represents 50 μm.*

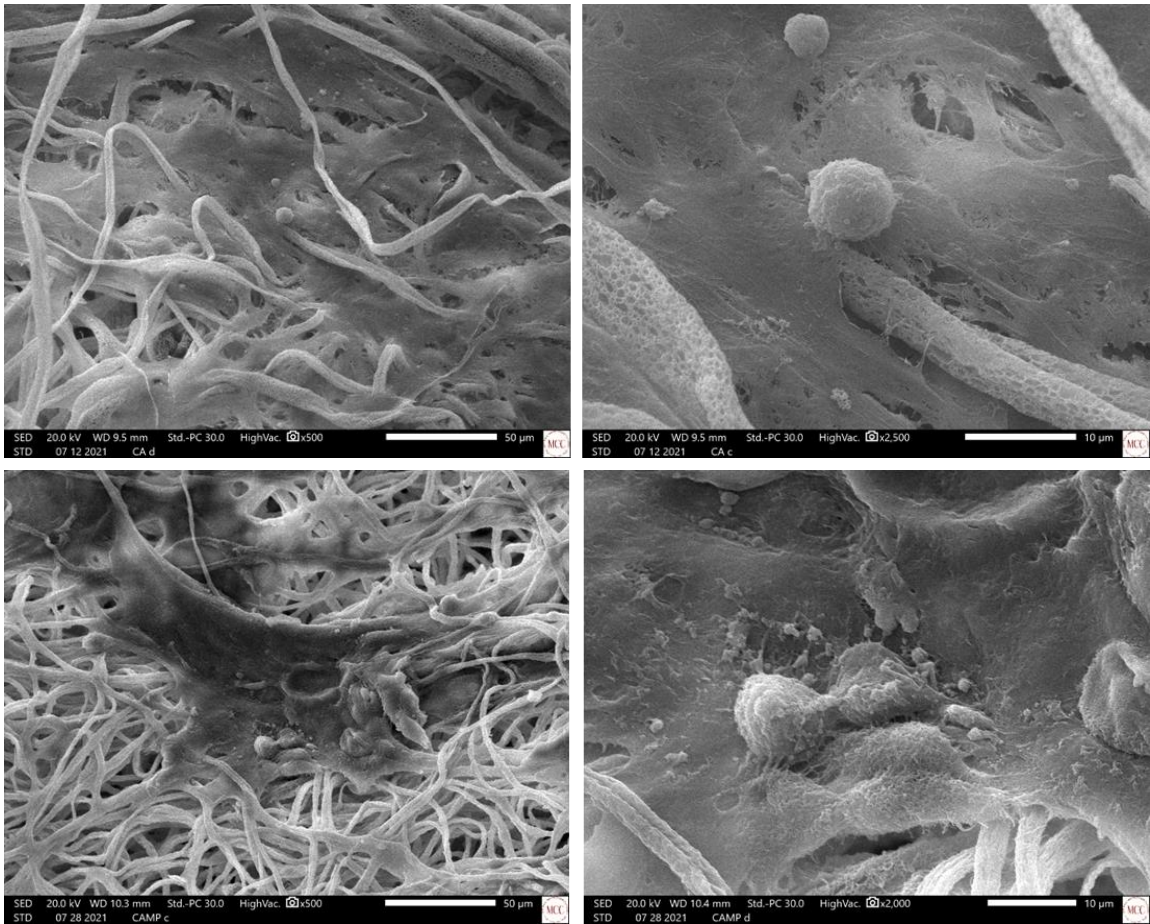


*Figure 4.19 SEM Images of hFOB on a) CA and b) CA-MP Fiber Mats after 14 Days of Incubation*

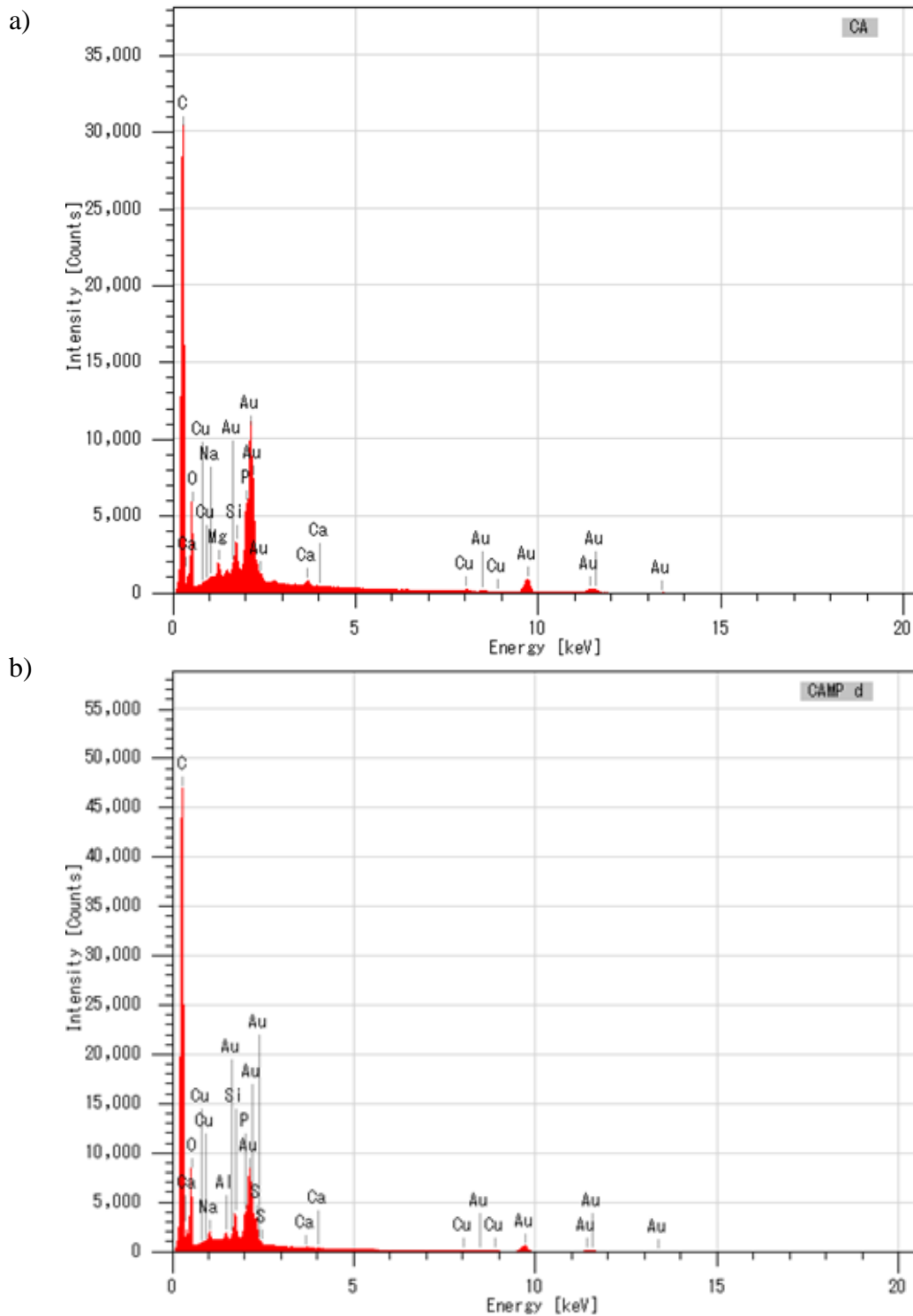


Figure 4.20 EDS of hFOB 1.19 on a) CA and b) CA-MP Fiber Mats

## CONCLUSION

This chapter presents an organic – biological approach used in the design of a bioactive scaffold model. In this chapter, using the electrospinning technique with Cellulose Acetate as starting material, a porous fiber mat was obtained to mimic the collagen fibers within bone extracellular matrix (ECM). The mats were chemically modified by two approaches in preparation for bioactivation. The porous fibers provided rough surfaces and a favorable arrangement for cells to grow. Peptide coupling approach has proven beneficial for initial cell adhesion; but, had no significant effect on differentiation and/or maturation. Independent of the Fiber Mat treatment, all peptides allowed the differentiation and maturation of the osteoblast progenitor cells and all cells were able to attach to the fibers in their usual extended manner except for -KRSR which induced a cellular agglomeration effect on the mats. SEM/EDS confirmed the presence of Calcium and Phosphorous elements in the mats after 14 days of incubation indicating that new bone was being formed.

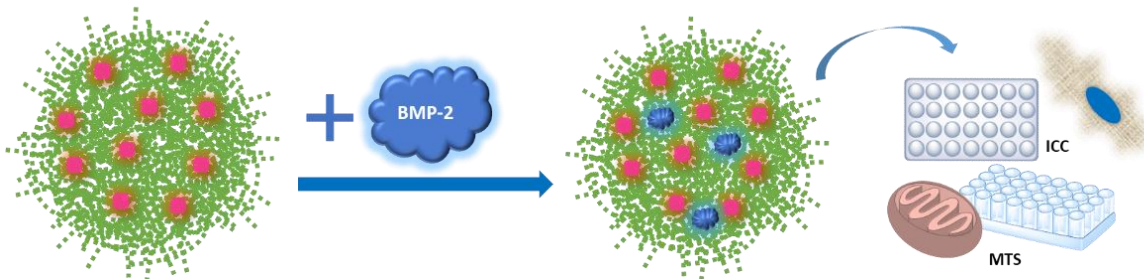
There is no known correlation between the amount of peptide present and the expression of the proteins which is a limitation of the project; but since the initial modifications and optimizations were already developed, a method for the quantification of the peptides present in the CA fiber mats would be the next step to explore. It will be possible then, and only then, to compare the expression of the markers across groups. Nevertheless, it can be concluded that the peptide coupling approach proved to be a potential alternative to implement in BTE to drive initial osteoconduction in biomaterials.

## CHAPTER 5: CELLULOSE NANOCRYSTALS AS HAp MATRIX

### ABSTRACT

This chapter presents an inorganic – biological approach by evaluating varying proportions of a Cellulose Nanocrystals (CNC's) polysaccharide network with Hydroxyapatite (HAp) composite synthesized via a simple sol gel method to be used as coating material for bone implants. The composites were characterized by means of TGA, XRD, FT-IR, DLS, Zeta Potential and SEM and neither of the properties of CNC or HAp changed due to the chemical interaction between them. After an MTS viability assay, having found a high cellular viability in the CNC biopolymer alone, using the same HAp-CNC proportion the concentration of CNC was varied and tested at 3, 6, and 9 %. The incorporation of the bone morphogenetic protein 2 (BMP-2) was also done to further evaluate the effects that the interaction could have with progenitor osteoblast cells (hFOB 1.19). Statistical comparison between viability percentages of same composite samples with and without the BMP-2 showed no correlation between the viability and inclusion of BMP-2.

### SYNOPSIS



## INTRODUCTION

Thanks to Per-Ingvar Brånemark who serendipitously discovered the fusing of bone with titanium (osseointegration) in 1952, Titanium (Ti) and its variations as alloys are broadly used for dental and orthopedic implants.<sup>86</sup> Implants are medical devices made to replace missing joints or bones; or to support damaged bones when the risk of injuries are large. The most common implant material is the Ti<sub>6</sub>Al<sub>4</sub>V alloy due to its high biocompatibility and load bearing properties; however, their biomechanical properties often cause failure. Some major contributors of implant failures are: conflicts in physical properties between the implant and the body, biocompatibility, deterioration, surgical procedures, and design failure.<sup>87</sup> The recovery time needed to return to normal activities fluctuates around a year and if poor or no osseointegration occurs, implants can engage in mechanical loosening causing a wear on the articular bearing surface that lead to dislocation, which corresponds to the leading cause of failure. As a result of poor osseointegration at the bone-implant interface, surface topographies have been explored to increase surface area and promote higher bioactivity through bioactive coatings.<sup>88</sup>

Advances in Bone Tissue Engineering (BTE) hold promise for the development of new functional coatings for bone regeneration. The integration of novel bionanomaterials that induce bone regeneration can contribute to the field of BTE and help settle the incidence of bone disorders and conditions.<sup>89-90</sup> The most studied material to replace and regenerate human hard tissue is Hydroxyapatite (HAp), an interesting biomaterial with potential to improve the field of medicine and dentistry. As discussed in Chapter 1, HAp is chemically and structurally similar to the inorganic components of bone, enamel, and dentin; it is also bioactive and supports bone ingrowth and osseointegration. Due to these

unique features it has been successfully used as bone fillers, aesthetic restorative, coating of orthopedic implants, filler of inorganic/polymer composites, and cell-culture carriers, among others.<sup>91</sup>

Overall, the use of basic calcium phosphate (BCP) crystals, such as HAp, has been associated with many diseases due to their deposition in intraarticular and periarticular locations site.<sup>92</sup> New pathogenic mechanisms for the deposition mechanisms of BCP's suggests that the extracellular inorganic phosphate, inorganic pyrophosphate and  $\text{Ca}^{2+}$  concentrations are critical determinants of mineralization.<sup>93-94</sup> It has been found that BCP crystals activate three major signaling pathways: crystal endocytosis and intracellular crystal dissolution with subsequent intracellular calcium increase.<sup>95</sup> Therefore, by placing the HAp in a polysaccharide network might prevent this cell activation. Additionally, the use of HAp as a coating agent for metallic implants has been discouraged by many scientists because it is limited to non-load bearing applications due to the disproportion between the different Young's modulus of each. This is an undesired effect because it leads to bone density loss and even fracture or disconnection of bone from the implant. It is of our interest that the polysaccharide network could serve as a hardening intermediate between the bone and the implant.<sup>96</sup>

There are many polysaccharides that have been used for tissue engineering applications such as chitosan and gelatin.<sup>97-98</sup> A similar material, cellulose nanocrystals (CNC), has been the subject of study in several applications because it is one of the most abundant biopolymers on earth, it is non-toxic and because it has a Young's Modulus of 167.5 GPa comparable to the stiffness of titanium, copper, and bronze materials used in bone implants (Chapter 1).<sup>99</sup> In this chapter the use of CNCs as a polymer matrix is used



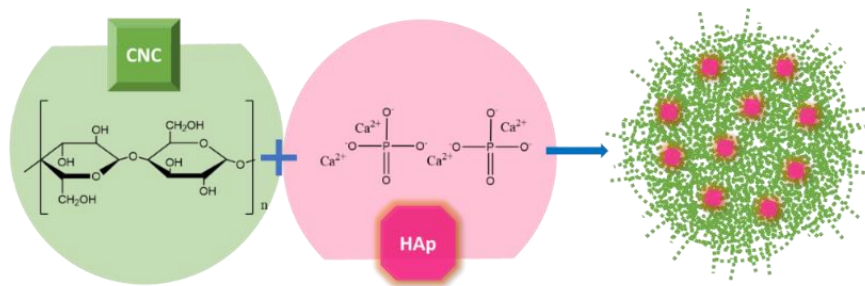
to suspend HAp and evaluate its potential for osteoconduction using biological assays of MTS and ICC.

## RESULTS AND DISCUSSION

### 5.1. Composite Fabrication

In the interest of evaluating a potential bioactive coating for Ti alloys used as bone implants the creation of a nanohydroxyapatite (nHAp) composite with cellulose nanocrystals (CNC) was developed. To compare the effects of polysaccharide to BCD crystals, three composites were prepared with different proportions of HAp and CNC following the proportions of HAp>CNC, HAp=CNC, and HAp<CNC while maintaining the same ratio of ethanol and acetic acid such as the procedure used to produce nHAp from HAp, by Monreal et al.<sup>100</sup> In brief, 1 mL of 99 % chemically pure grade biopolymer  $\beta$ -1, 4-D-linked glucose (CNC) at a 3.2 % wt was placed at 30 °C for 30 minutes and added to the solutions of HAp with 5mL ethanol and 1.25 mL acetic acid for gel formation. The first solution (nHAp>CNC) was prepared using 0.5 g HAp and 9.17  $\mu$ L CNC's (3.2%), the second solution (nHAp=CNC) consisted of 0.5 g HAp and 458  $\mu$ L CNC's (3.2%), and the third solution (nHAp<CNC) of 0.01 g HAp and 458  $\mu$ L CNC's (3.2%) subsequently the solutions were sonicated at 30 °C for 15 minutes. After sonication each gel was placed in a 50 mL tube and centrifuged 3 times at 12,500 rpm for 5 minutes at 30 °C, in-between the procedure, the concentrated gel was poured off and the precipitate was re-suspended twice with deionized water to eliminate any amount of gel residue. The resulting pellet was freeze dried for 24 hours and stored for further characterization.





*Scheme 5.1 Representation of the Interaction between CNC and HAp in the Composite*

### 5.1.1. TGA

The thermal stability of the composites was assessed to obtain indications of the interactions between particles and about the critical transition temperatures in the material. As can be seen in Figure 5.1, a temperature drop at 300 °C was consistently observed and is ascribed to the thermal decomposition of the CNC while the nHAp decomposition transition was not observed as it belongs to a region of approximately 1080 °C, although some mass loss is present. The decomposition of nHAp occurs in three steps: (1) the appearance of  $\text{Ca}_{10}(\text{PO}_4)_6\text{O}_x(\text{OH})_{2-2x}$  as a transition product for the (2) dehydroxylation producing oxyapatite  $\text{Ca}_{10}(\text{PO}_4)_6\text{O}$  ending with (3) decomposition of this oxyapatite and resulting calcium phosphates.<sup>101</sup> The mass losses belonging to the first two steps can be observed at around 400 °C and 600 °C respectively for each sample. The nHAp>CNC sample (red) is the most stable of all, maybe due to the higher proportion of Hap, followed by the nHAp=CNC (black) with a well-defined transition belonging to the CNC and nHAP. Lastly, the nHAp<CNC sample (blue) shows less thermal stability due to a lower amount of CNC in the sample in comparison to the nHAp with a higher change in mass loss at 300 °C belonging to the CNC. Also, in this sample a transition at 450 °C ascribed to the mass loss from the first step of the decomposition of nHAp appears to be more significant. This behavior may be due

to the expected stronger interaction between nHAp and CNC that will ultimately cause heat dissipation to reach the transition product. The heat flow results also evidence the evaporation of remaining water in the samples. The transitions ascribed to the water removal are not very noticeable in the gravimetric results at 130 °C. These results suggest a correlation between the ratio of nHAp and the thermal stability. It is noticeable that the samples with higher hydroxyapatite content provides better thermal stability as it was expected due to the degradation temperature of nHAp being much higher than that of CNC.

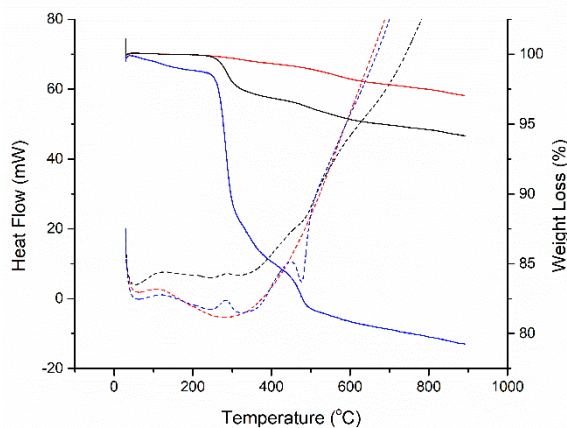


*Figure 5.1 TGA and DSC Analysis of nHAp>CNC (red), nHAp=CNC (black), nHAp<CNC (blue)*

### 5.1.2. X-Ray Diffraction (XRD)

The CNC peaks can be observed between  $10^{\circ}$  -  $25^{\circ}$  with characteristic phases of (110) at  $17^{\circ}$  and (200) at  $26^{\circ}$ , a zoomed version of this area can be observed in Figure 5.2.<sup>102-103</sup> The nHAp characteristic phases are observed at  $32^{\circ}$ ,  $39^{\circ}$  and  $49^{\circ}$  with peaks corresponding to the phases of (311), (410) and (313) respectively (COD ID 2300273).<sup>103</sup> As a qualitative observation, the intensity of the CNC peaks is much lower than those of the nHAp due to the high crystallinity of nHAp in comparison to CNC but this does not mean that the CNC loses crystallinity. As can

be observed, all diffraction patterns showed the same behavior leading to the conclusion that the crystallinity of the sample was not compromised after sol-gel reaction with polysaccharide network. It is important to note that as the crystallinity of the cellulose decreases, the level of water absorption and biodegradability increases because with decreasing crystallinity cellulose fibers start losing their organization and become more susceptible to degradation processes.<sup>104</sup> Because of this, the CNC in the synthesized composite will not degrade which sustains the initial purpose of using CNC that can serve as a hardening agent due to its high Young's modulus and reinforcing the strength of the composite material adjacent to the natural bone. It is also possible that this polymer network formed by cellulose may prevent the mineralization of HAp and deposition in the intraarticular and periarticular locations.

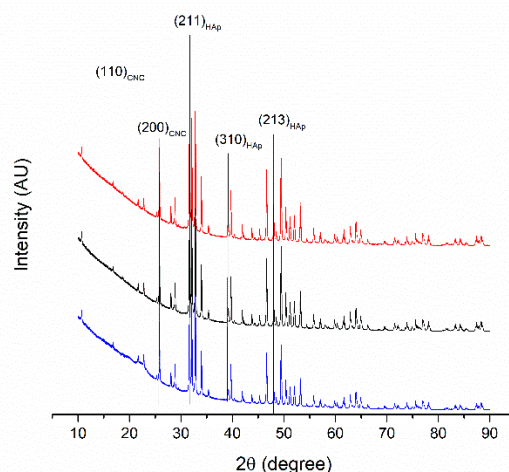


**Figure 5.2** Powder XRD Patterns of nHAp>CNC (red), nHAp=CNC (black), nHAp<CNC (blue)

### 5.1.3. Fourier Transform Infrared Spectroscopy (FT-IR)

FTIR was carried out from 400 to 4000  $\text{cm}^{-1}$  (Figure 5.3) and the presence of CNC is confirmed by the band at around 3400  $\text{cm}^{-1}$  due to OH-stretching, a band at 1640  $\text{cm}^{-1}$  likely due to the OH-bending vibration of adsorbed water and the band

at  $2889\text{ cm}^{-1}$  assigned to C-H aliphatic stretching. Other noticeable bands are from C-O-C (ether) at  $1200\text{ cm}^{-1}$  and  $\text{CH}_2$  (alkaline) at  $692\text{ cm}^{-1}$  are also worth noting. It is important to observe that even though nHAp is an ionic compound, its anions ( $\text{PO}_4^{2-}$ ) are present at  $1020\text{ cm}^{-1}$  and  $559\text{ cm}^{-1}$ . The peaks around  $2000\text{ cm}^{-1}$  are attributed to the presence of  $\text{CO}_2$  in the samples so these were discarded for the analysis of the spectrum.

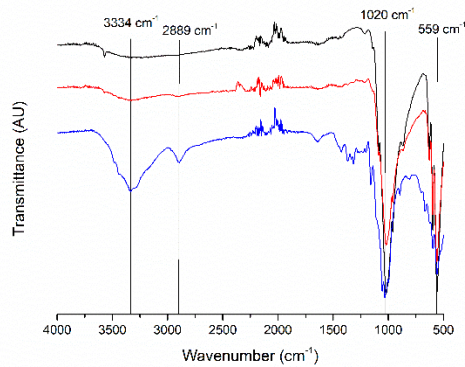


**Figure 5.3** FTIR of nHAp>CNC (red), nHAp=CNC (black), nHAp<CNC (blue)

#### 5.1.4. Dynamic Light Scattering (DLS)

It has been noted that the composite size and homogeneity of the particles can influence the adherence of tissue to the host implant. As a strategy to account for the composite size, DLS analyses were conducted and are shown in Table 5.1. First, the size for natural HAp and CNC was determined and then the analysis of the particle size and distribution for the composites was carried out. As can be observed for the Z-Average ( $R_H$ ) results, most particles fluctuated between 289 to 311nm. The results showed that the size for the nanoparticles were 311 nm for the nHAP>CNC, 289 nm for the nHAP=CNC and 307 nm for the nHAP< CNC composites. The polydispersive index (PDI) for the nHAP>CNC and nHAP=CNC

samples were the lowest with a value of 0.21 which indicates a good size uniformity of the particles, a factor that is notably missing in the nHAp<CNC. The average reduction of particle size from starting natural HAp with an average size of 2061 nm is approximately 85.7%, which proves that the polymer network was a determining factor in this size reduction; a representation of this interaction can be observed in Scheme 1.

<b>Sample*</b>	<b>Z-average (nm)</b>	<b>PDI</b>
<b>nHAp&gt;CNC (3.2%)</b>	311 ± 7	0.21 ± 0.02
<b>nHAp=CNC (3.2%)</b>	289 ± 3	0.21 ± 0.01
<b>nHAp&lt;CNC (3.2%)</b>	307 ± 5	0.43 ± 0.00
<b>Natural HAp</b>	1965 ± 170	0.29 ± 0.04
<b>CNC</b>	142.3 ± 0.72	0.30 ± .007

*Table 5.1 DLS analyses for HAp, CNC and nHAp-CNC at a 1% w/v*

#### 5.1.5. SEM

To further verify this, SEM was carried out to correlate the size and homogeneity of the composites and are presented in Figure 5.4. From these images it can be observed that the nHAp>CNC sample presents a high porosity while the nHAp=CNC showed a better uniformity in the spherical shape, distribution, and particle size and the nHAp<CNC showed neither of these. Also, in agreement with DLS, the sizes of the particles are between 150-300nm with few particles whose size is over 300 nm. The presences of submicron particles are attributed to the aggregation factor that occurs when the solution is in suspension; nevertheless, the formation of smaller nanoparticles is present. Upon discussion, the biological experiments were proceeded with samples nHAp>CNC and nHAp=CNC.

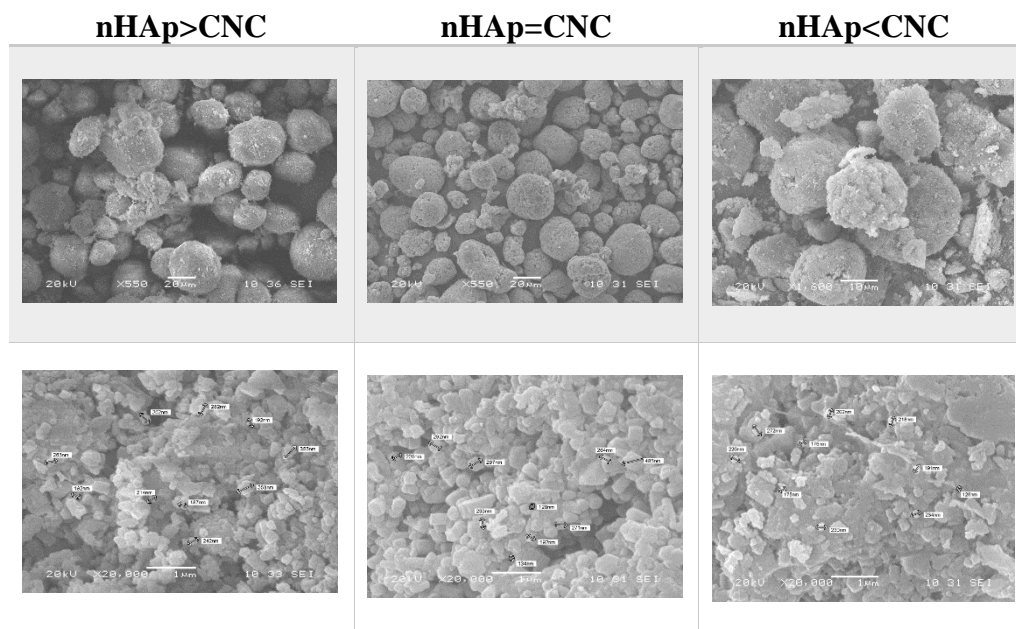


Figure 5.4 SEM Images of Varying Ratios of nHAp:CNC Composites

## 5.2. Inclusion of BMP-2 to nHAp

The incorporation of the BMP-2 to the composites was made by firstly diluting 10  $\mu\text{g}$  of BMP-2 in 1000  $\mu\text{L}$  of PBS. Afterwards, two solutions of 0.01 g of nHAp>CNC and nHAp=CNC were prepared in 900  $\mu\text{L}$  of PBS and 100  $\mu\text{L}$  of the solution containing the BMP-2 were added to each.

### 5.2.1. DLS

DLS was also carried out for the BMP-2 protein alone and with its incorporation to the composites, a representation of this interaction can be observed in Scheme 2. The BMP-2 size was found to be 59.97 nm and for the nHAp<CNC and nHAp=CNC composites with the protein, it was observed that the size of the nanoparticles remained around 349 nm which is still in the range of our composites without the protein with a PDI of 0.24 (Table 5.2).

Sample*	Z-average (nm)	PDI
<b>nHAp&gt;CNC (3.2%) + BMP-2</b>	333.4 ± 11	0.18 ± 0.01
<b>nHAp=CNC (3.2%) + BMP-2</b>	364.6 ± 2	0.30 ± 0.02
<b>BMP-2</b>	59.97 ± 0.9	0.46 ± 0.04

*Table 5.2 DLS analyses for BMP-2, nHAp>CNC and nHAp=CNC composites with protein at 1% w/v*

### 5.2.2. Zeta Potential

After thorough characterization of the composites, Z-Potential was performed to determine the overall charge of the nHAp>CNC and nHAp=CNC composites with and without the BMP-2 (Table 5.3). The analyses were run in PBS to understand how the composites would behave under physiological conditions. The overall charge of the HAp alone was found to have an average charge of -19.36 mV. The isoelectric point of the BMP-2 is 8.5 and therefore below this value the BMP-2 will be positively charged.<sup>105</sup> When the Z-potential measurement was performed with the protein alone, the charge resulted to be -12.8 mV, which indicates that there is in fact an interaction occurring between the protein and composite. A recent study about thermodynamics studies on the BMP-2 adsorption onto different hydroxyapatite surfaces conducted by Zhiwei Lu and team have reported that the process of adsorption is by physisorption where the initial driving force is governed by an electrostatic interaction between the HAp (negatively charged at pH=7.2) and BMP-2 (positively charged at pH=7.2). They report that this process has a positive  $\Delta H$  corresponding to an endothermic process and negative  $\Delta G$  corresponding to a spontaneous and energetically favored process.<sup>106</sup> The composites alone had an average charge of -11.4 and -18.1 mV for the nHAp>CNC and nHAp=CNC respectively and the charges with the BMP-2 were lowered to -11.0 and -17.3 mV,

respectively. Several studies have already shown that the incorporation of BMP-2 result in an initial burst release followed by a stable sustained release of the protein.<sup>107</sup> This slight decrease in the overall charge suggests that there is in fact an interaction between the composites and the protein although this does not provide any inquiry over the stability of the construct.

Sample	Zeta Potential (mV)
Natural HAp	-20 ± 2
BMP-2	-11.4 ± 0.7
nHAp>CNC	-18 ± 1
nHAp=CNC	-11.0 ± 0.6
nHAp>CNC & BMP-2	-17.3 ± 0.6
nHAp=CNC & BMP-2	-20 ± 2

*Table 5.3 Zeta Potential measurements of nHAp>CNC and nHAp=CNC with BMP-2*

### 5.2.3. Biocompatibility of Composites with Bone Progenitor Cells

To examine the effect in cell viability of the nHAP:CNC composites, osteoblasts cells were exposed to 5 mg/mL of nHAp, CNC, nHAp>CNC, nHAp=CNC, nHAp>CNC+BMP-2 and nHAP=CNC+BMP-2 for 24 hrs and afterwards used MTS CellTiter 96 ® AQueous Solution Cell proliferation Assay (Promega). Cells were plated at  $7.5 \times 10^4$  cells/mL in 96 well plates (Falcon) in contact with 5 mg/mL of the different nanocomposites and incubated for 24 hrs. Then, 20 µL of MTS reagent was added and cells were incubated for 1 hr. Thereafter, the 96 well plates were centrifuged at 1000 rpm for 10 min to avoid any further light scattering from the nanomaterials. Then, 100 µL of the supernatant were transferred to a new 96 well plate and absorbance was measured at 490 nm using a Synergy H1 Hybrid



Microplate Reader from BioTek. Results shown in Figure 5.5 and demonstrate that neither of the compounds compromised the osteoblast cell viability. As can be noted, the nHAp>CNC+BMP-2 composite had the highest growth of osteoblast in comparison to the others. The plotted values represent average  $\pm$  standard error from four replicates and the asterisk indicates statistical significance against untreated samples ( $p < 0.05$ ). This result was expected given the fact that one of the reasons HAp was chosen is because of its high porosity in which the pore size of these scaffolds as long as it is equal or bigger than 20  $\mu\text{m}$  will permit the growth of cells.<sup>108</sup>

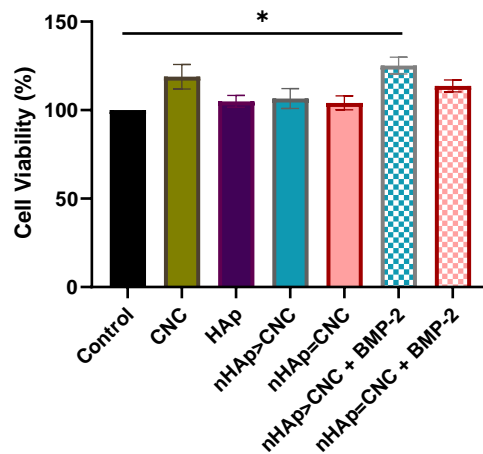


Figure 5.5 Cell Viability Against nHAp:CNC composites.

### 5.3. CNC biopolymer potential

After noticing an elevated cell viability result in the CNC sample, an increase in CNC percentage on the composites was evaluated while maintaining the ratio constant. Following the same procedure of the previous work, composites were evaluated biologically using 0.125g HAp and 2.5 g of variable CNC percentages of 3, 6, and 9 %.

#### 5.3.1. SEM

The composites were spin coated onto glass discs and the cells were seeded at 10,000 cells/ well in a 24 well plate containing the discs. Cells were allowed to grow

for 24 hours after which they were fixed with glutaraldehyde, dehydrated in a series of EtOH solutions beginning at 10% until 100% and dehydrated with HMDS in a 1:3 HDMS:EtOH, 1:1 and 3:1 ratio. The glass discs were gold coated (10 nm) and the cell morphology was analyzed in SEM. Few cells can be observed in Figure 5.6 possibly due to the small number of cells seeded, or to a detachment of the adsorbed HAp-CNC layer on the glass discs while performing the pipetting involved in the fixation and dehydration procedures. There are some protruded structures that are questionable whether belonging to the composite coated or to the cells; but, samples e) HAp-CNC (6%) and f) HAp-CNC (9%), clearly depict the cytoskeleton of the cells where filopodia can be observed. A BrdU proliferation assay was performed afterwards increasing the number of cells seeded.

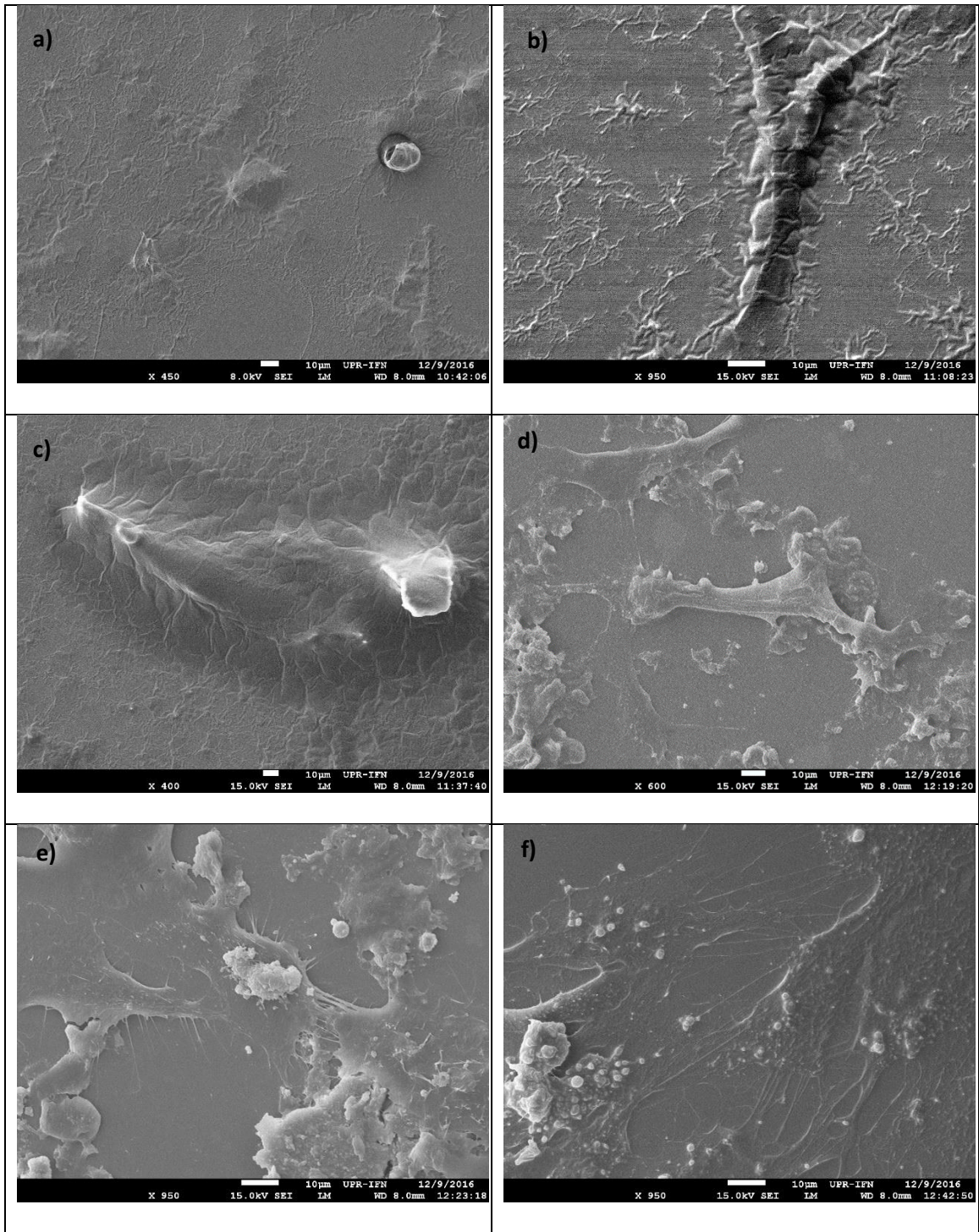


**Figure 5.6** SEM Images of hFOB 1.19 Morphology at a) control, b) HAp, c) CNC, d) HAp-CNC (3%), e) HAp-CNC (6%) and f) HAp-CNC (9%)

### 5.3.2. BrdU Proliferation Assay

Just like in the previous SEM experiment, the composites were spin coated onto glass discs and the cells were seeded at 50,000 cells/well in a 24 well plate containing the samples (Figure 5.7). The procedure for this experiment is the same as in Chapter 4 with a difference in the image acquisition process. The images were taken with a fluorescence microscope in the black and white channels. The images were colored using ImageJ software from FIJI with contrasting red and green colors representing the nuclei and BrdU positive nuclei respectively. The images demonstrate that there were cells proliferating in all samples; but the CNC biopolymer alone had an agglomeration effect on the cells. Possibly due to the lack of bioactivity from the CNC, that does not stimulate osteoconduction. The total amount of cells counted was plotted for each of the samples as can be seen in Figure 5.8. Even though the highest number of cells were found to be in the HAp sample, to fill a defect with HAp alone is not possible without a hardening agent present. The CNC biopolymer had much less cells than any other sample, including the control; but when incorporated into the composite with HAp, was an anchoring site for the cells. Between the 3 formulations tested with varying CNC percentages, the HAp-CNC (6%) presented an 18.1% increase in cell attachment against the HAp-CNC (3%). This assay was complimented with an MTS assay to evaluate cellular viability against each composite.

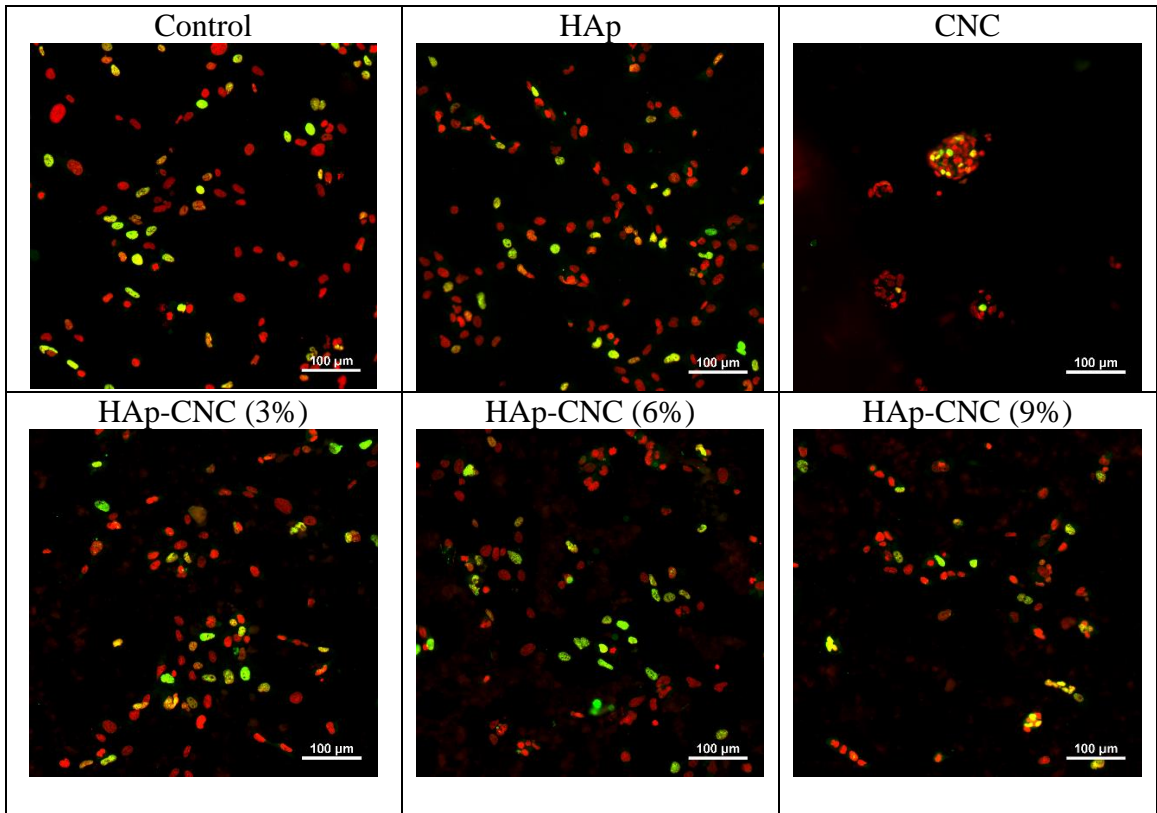


Figure 5.7 BrdU Images for HAp-CNC Samples

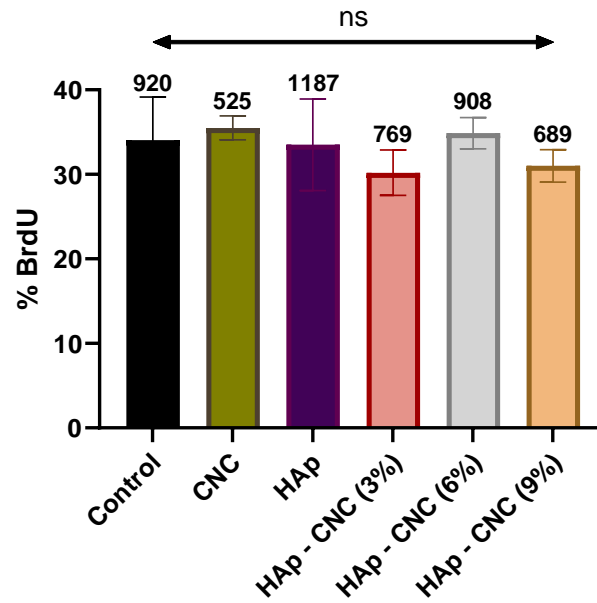


Figure 5.8 BrdU Positive Cells Expressed as Percentages with Total Number of Cells over each Sample

### 5.3.3. MTS Cell Viability Assay

MTS assay was carried out using the same procedure as depicted previously (see section 5.2.3). Results in Figure 5.9 indicate that cells are viable in all the experimental samples and there is an increase in viability against untreated control cells. We can see statistically significant differences against the control with the 6% formulation without the protein and with both 9% composites. The difference between groups of 6% was statistically significant as well indicating this 6% formulation does not need the BMP-2 protein for the cells to be viable. There is some discrepancy between the composite formulations and the inclusion of the protein; but focusing solely on the composites with the BMP-2 protein, an increase in cell viability can be observed with increasing CNC concentration. This could be explained by considering other physicochemical properties of the composite that promote osteoblastic adhesion such as wettability or higher hydrophilicity that CNC can promote or considering the surface chemistry of the composites. According to previous research by Keselowsky et al., osteoblasts adhesion to a surface with differently chargeable functional groups follow the trend:  $\text{OH} > \text{COOH} = \text{NH}_2 > \text{CH}_3$ .<sup>109</sup>

However, these experiments were performed in a 2 dimensional material that is not necessarily indicative of the cellular behavior that would be expressed in a three dimensional material. To assert the previous statement about the percentage of the CNC biopolymer being sufficient without the incorporation of a bioactive agent, more experiments can be further done. The cells could be seeded in different physical surfaces (i.e. nanotubes) or in aerogels, microfluidic devices coated with the composites and it will be crucial to extend the culture times enough to measure maturation and new tissue formation by ICC assays. Also, further work with these composites could include

comparisons between covalent coupling of the protein to the composite or using the BMP-2 peptide explored in Chapter 4.

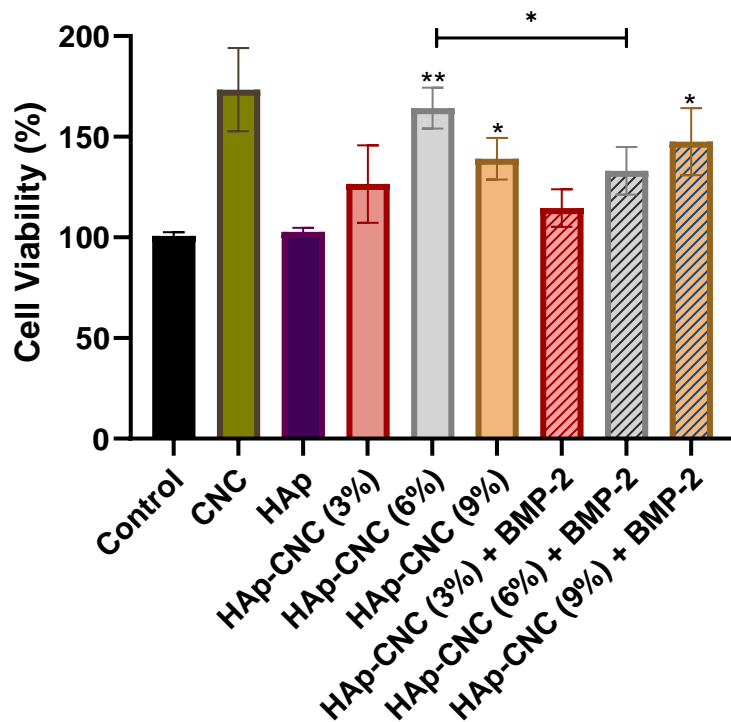


Figure 5.9 Cell Viability Assay of hFOB's 1.19 Against HAp-CNC (3, 6, 9)% and with BMP-2 Inclusion

## CONCLUSION

The potential of using cellulose nanocrystals (CNC) biopolymer with suspended Hydroxyapatite (HAp) proved to be a viable approach to explore as composite materials in the field of Bone Tissue Engineering (BTE). These developed composites can be used as coating for bone implants to promote osteoconduction and decrease implant failure. The proportion of the nHAp=CNC ratio appeared to be the most suitable ratio for the sol-gel methodology as it provides homogeneity of the particle's size and distribution that was shown by the DLS and SEM analyses. The CNC did work as expected by the sol gel method to include HAp in its network without affecting its degree of crystallinity, as shown by the

XRD analyses, or the thermal stability as shown by the TGA analyses. Neither of the properties of either CNC or HAp changed due to the chemical interaction between them. The inclusion of BMP-2 does not appear to have a negative effect on the particle size and the charge reduction indicates that there is an interaction between the protein and the composite. The cell proliferation and viability assays demonstrated that all our composites promoted an increased cell growth but the nHAp>CNC ratio with BMP-2 had a higher growth percentage than the other composites as well as the HAp-CNC (6%). However, statistical comparison between viability percentages of same composite samples with and without the BMP-2 showed no correlation between the viability and inclusion of BMP-2. These findings can be further supplemented with comparisons between the inclusion of the BMP-2 peptide versus the whole protein and they can also be studied by immunocytochemistry for the expression of other cellular proteins that will provide more information about the cellular responses towards the material as those seen in Chapter 4.



## GENERAL CONCLUSIONS

The purpose of this research was to test the potential applicability of different biopolymers prepared by different fabrication methods in the field of Bone Tissue Regeneration (BTR). As previously mentioned, cell-based approaches in Bone Tissue Engineering (BTE), have focused on using pre-calcified materials or simulated body fluid (SBF) treated models that are not able to reproduce either the complexity of the bone's three-dimensional (3D) microenvironment or the nanoscale characteristics of mineralized bone collagen.<sup>66</sup> As exposed in Chapter 1, scaffolds must be structures providing void spaces for matrix deposition, biocompatible, and bioactive.

In this work we explored three different biopolymers, fabricated with different methodologies as potential scaffolds to aid in BTR. Beginning with Sodium Alginate and incorporating an organic-inorganic coordination approach to recover catechol from wetland sources, the fabricated membrane did not meet the physical requirements to favor osteoblastic adhesion. The adhered catechols were not driving osteoconduction, much less rendering the prepared material bioactive as it was seen in Figure 3.12. In the interest of providing a proven bioactive surface with void space for matrix deposition we incorporated an organic-biological approach by fabricating an electrospun biopolymeric Cellulose Acetate (CA) fiber mat and coupling bioactive peptides that would favor osteoblastic adhesion. Not only was this approach proven to be osteoconductive; but also, showed osteoinductive behavior as seen in the maturation assessments (Figure 4.11 and Figure 4.14) demonstrating the ability of osteoprogenitor cells to differentiate and produce new extracellular matrix (ECM) tissue (i.e. Collagen formation). In the last approach, we used an inorganic-organic approach with proven bioactive Hydroxyapatite (HAp) and Cellulose

Nanocrystal (CNC) biopolymer. Cellular proliferation was achieved as well as cellular viability, proving the biocompatibility of the composite; but statistical analysis did not evidence a preference towards a specific formulation and to determine bioactivity other assays need to be performed.

The electrospinning (ES) technique utilized in this work for scaffold fabrication is not necessarily indicative of the bioactivity of biomaterials. As shown in Chapter 3, even though we achieved high surface areas with biocompatible alginate, no evidence of cellular adhesion, much less proliferation was found; and, the AlgFe sample that did contain some cell nuclei did not exhibit cytoskeletal extension (filopodia). Yet, using the same technique with a different biopolymer, CA, scaffolds with porous structures that favored osteoblastic adhesion even without the addition of bioactive molecules were obtained as was seen in Chapter 4. The success of scaffold fabrication using the electrospinning technique will be highly dependent on the biopolymer used, the parameters and achieved structures as well as chemical treatments of the resulting material. The sol-gel approach, although much simpler in terms of synthesis and fabrication, resulted in a difficult to handle product requiring a physical substrate in which the product could be deposited and used. Between the three explored approaches, the organic-biological approach in Chapter 4 was proven to favor natural osteoblastic responses required for osseointegration. The inorganic-biological approach in Chapter 5 also showed potential; but more work needs to be done to evaluate its bioactivity and future applicability to the field.

A factor that was not discussed thoroughly throughout this work was the models of the cellular systems studied. We cultured cells in both 2D and 3D environments; but neither one of these provided external stimuli that are present in the reality of the osteoblastic cell

lines and affect their mechanotransduction. Even though most of the physical sensing is done by osteocytes (differentiated osteoblasts that become embedded within the bone matrix), osteoblast behavior can also be influenced by environmental strain, pressure, and fluid flow and these conditions are difficult to include in cell culture systems. Nevertheless, including them would be as close as possible as one could get to mimicking bone load bearing activities. The findings resulting from this work contribute and expand the knowledge of polysaccharides used in the biomedical field for applications in BTE as tissue regeneration materials.

## APPENDIX I: SCIENCE COMMUNICATION

Scientists have a responsibility to bridge the gap between the public and science. Throughout a scientist's academic career, they have been constantly exposing their proposals, experimental results, and engaging in collaborations. It is critical for a scientist to develop good communication skills; and due to this, Simara has engaged in science communication throughout her academic career pursuit. Beginning as an incoming graduate student in Dr. Nicolau's lab, she was present in open houses and poster sessions to recruit new students to the lab and also developed these skills in her Research Assistant role to teach General Chemistry Laboratory Sections as part of her academic requirements. She presented her research in numerous scientific meetings and while participating in the Global Solutions Program, she was exposed to the entrepreneurial environment in which communicating adequately was crucial to attract attention from investors and engage in collaborations. Upon her return she continued to develop her science communication (SciCom) skills through volunteer experiences with different organizations. **She engaged in SciCom during her participation with the organizations below by:**

a. PRatian LLC

Pitching for funding at Kinesis organization



Conducting spectroscopy workshop at Luis Llorens Torres School



Representing PRatian at the Aerospace Startup Conference



b. EcoExploratorio: Museo de Ciencias de Puerto Rico

Conducting a Build your own rocket hands-on workshop for the Solar eclipse event.



c. Ciencia Puerto Rico

a. Semillas de Triunfo

Offering talks about women pursuing careers in science, exposing my work and sharing my experiences.



b. Puerto Rico Science Policy Action Network (PR-SPAN)

Publishing blogs on CienciaPR network, hosting a webinar involving Science Community with Policy Making and advocating for science.



d. Center for Innovation, Research and Education in Environmental Nanotechnology (CIRE<sup>2</sup>N)

Published a magazine called NanoAmbiente in collaboration with other fellows, developed a Problem Based Learning (PBL) approach in water remediation for school students, creating and editing several educational videos involving environmental policy and water polarity, working in science blog translations and participating in numerous outreach activities in schools and events.



## REFERENCES

1. Bilezikian, J. P.; Raisz, L. G.; Martin, T. J., *Principles of bone biology*. Academic press: 2008.
2. Florencio-Silva, R.; Sasso, G. R. d. S.; Sasso-Cerri, E.; Simões, M. J.; Cerri, P. S.; Rigo, Biology of Bone Tissue: Structure, Function, and Factors That Influence Bone Cells. *BioMed Research International* **2015**, *2015*, 17.
3. Roux, S.; Amazit, L.; Meduri, G.; Guiochon-Mantel, A.; Milgrom, E.; Mariette, X., RANK (Receptor Activator of Nuclear Factor kappa B) and RANK Ligand Are Expressed in Giant Cell Tumors of Bone. *American Journal of Clinical Pathology* **2002**, *117* (2), 210-216.
4. Simonet, W. S.; Lacey, D. L.; Dunstan, C. R.; Kelley, M.; Chang, M. S.; Lüthy, R.; Nguyen, H. Q.; Wooden, S.; Bennett, L.; Boone, T.; Shimamoto, G.; DeRose, M.; Elliott, R.; Colombero, A.; Tan, H. L.; Trail, G.; Sullivan, J.; Davy, E.; Bucay, N.; Renshaw-Gegg, L.; Hughes, T. M.; Hill, D.; Pattison, W.; Campbell, P.; Sander, S.; Van, G.; Tarpley, J.; Derby, P.; Lee, R.; Boyle, W. J., Osteoprotegerin: A Novel Secreted Protein Involved in the Regulation of Bone Density. *Cell* **1997**, *89* (2), 309-319.
5. Benjamin, B.; Benjamin, M. A.; Swe, M.; Sugathan, S., Review on the comparison of effectiveness between denosumab and bisphosphonates in post-menopausal osteoporosis. *Osteoporosis and Sarcopenia* **2016**, *2* (2), 77-81.
6. Campana, V.; Milano, G.; Pagano, E.; Barba, M.; Cicione, C.; Salonna, G.; Lattanzi, W.; Logroscino, G., Bone substitutes in orthopaedic surgery: from basic science to clinical practice. *Journal of materials science. Materials in medicine* **2014**, *25* (10), 2445-61.
7. García-Gareta, E.; Coathup, M. J.; Blunn, G. W., Osteoinduction of bone grafting materials for bone repair and regeneration. *Bone* **2015**, *81*, 112-121.
8. Polymeric Scaffolds in Tissue Engineering Application: A Review. *International Journal of Polymer Science* **2011**, *2011*.
9. Balakrishnan, B.; Banerjee, R., Biopolymer-based hydrogels for cartilage tissue engineering. *Chemical reviews* **2011**, *111* (8), 4453-74.
10. Lee, J.-W.; Lee, K.-B.; Jeon, H.-S.; Park, H.-K., Effects of Surface Nano-Topography on Human Osteoblast Filopodia. *Analytical Sciences* **2011**, *27* (4), 369-369.
11. Campbell, I. D.; Humphries, M. J., Integrin Structure, Activation, and Interactions. *Cold Spring Harbor Perspectives in Biology* **2011**, *3* (3), a004994.
12. Olivares-Navarrete, R.; Rodil, S. E.; Hyzy, S. L.; Dunn, G. R.; Almaguer-Flores, A.; Schwartz, Z.; Boyan, B. D., Role of integrin subunits in mesenchymal stem cell differentiation and osteoblast maturation on graphitic carbon-coated microstructured surfaces. *Biomaterials* **2015**, *51*, 69-79.
13. George, A.; Sanjay, M. R.; Srisuk, R.; Parameswaranpillai, J.; Siengchin, S., A comprehensive review on chemical properties and applications of biopolymers and their composites. *International Journal of Biological Macromolecules* **2020**, *154*, 329-338.
14. Newsom, J. P.; Payne, K. A.; Krebs, M. D., Microgels: Modular, tunable constructs for tissue regeneration. *Acta Biomaterialia* **2019**, *88*, 32-41.
15. Morelli, S.; Salerno, S.; Piscioneri, A.; De Bartolo, L., 4.12 Membrane Approaches for Liver and Neuronal Tissue Engineering. In *Comprehensive Membrane Science and Engineering (Second Edition)*, Drioli, E.; Giorno, L.; Fontananova, E., Eds. Elsevier: Oxford, 2017; pp 248-271.

16. Laurienzo, P.; Malinconico, M.; Motta, A.; Vicinanza, A., Synthesis and characterization of a novel alginate-poly (ethylene glycol) graft copolymer. *Carbohydrate Polymers* **2005**, *62*, 274-282.
17. Pawar, S. N.; Edgar, K. J., Alginate derivatization: A review of chemistry, properties and applications. *Biomaterials* **2012**, *33* (11), 3279-3305.
18. Gauss, C.; Pickering, K. L.; Muthe, L. P., The use of cellulose in bio-derived formulations for 3D/4D printing: A review. *Composites Part C: Open Access* **2021**, *4*, 100113.
19. Liu, C.; Bai, R., Preparation of chitosan/cellulose acetate blend hollow fibers for adsorptive performance. *Journal of Membrane Science* **2005**, *267* (1-2), 68-77.
20. Vega-Figueroa, K.; Santillán, J.; García, C.; González-Feliciano, J. A.; Bello, S. A.; Rodríguez, Y. G.; Ortiz-Quiles, E.; Nicolau, E., Assessing the Suitability of Cellulose-Nanodiamond Composite As a Multifunctional Biointerface Material for Bone Tissue Regeneration. *ACS Biomaterials Science & Engineering* **2017**, *3* (6), 960-968.
21. Chen, H., 5 - Lignocellulose biorefinery product engineering. In *Lignocellulose Biorefinery Engineering*, Chen, H., Ed. Woodhead Publishing: 2015; pp 125-165.
22. Niaounakis, M., 1 - The Problem of Marine Plastic Debris. In *Management of Marine Plastic Debris*, Niaounakis, M., Ed. William Andrew Publishing: 2017; pp 1-55.
23. Domingues, R. M. A.; Gomes, M. E.; Reis, R. L., The Potential of Cellulose Nanocrystals in Tissue Engineering Strategies. *Biomacromolecules* **2014**, *15* (7), 2327-2346.
24. Salam, A.; Lucia, L. A.; Jameel, H., A Novel Cellulose Nanocrystals-Based Approach To Improve the Mechanical Properties of Recycled Paper. *ACS Sustainable Chemistry & Engineering* **2013**, *1* (12), 1584-1592.
25. George, J.; Sabapathi, S. N., Cellulose nanocrystals: synthesis, functional properties, and applications. *Nanotechnol Sci Appl* **2015**, *8*, 45-54.
26. Zhou, C.; Wu, Q., *Recent Development in Applications of Cellulose Nanocrystals for Advanced Polymer-Based Nanocomposites by Novel Fabrication Strategies*. 2012.
27. Obotey Ezugbe, E.; Rathilal, S., Membrane Technologies in Wastewater Treatment: A Review. *Membranes* **2020**, *10* (5), 89.
28. Skuse, C.; Gallego-Schmid, A.; Azapagic, A.; Gorgojo, P., Can emerging membrane-based desalination technologies replace reverse osmosis? *Desalination* **2021**, *500*, 114844.
29. Miller, D. J.; Dreyer, D. R.; Bielawski, C. W.; Paul, D. R.; Freeman, B. D., Surface Modification of Water Purification Membranes. *Angewandte Chemie International Edition* **2017**, *56* (17), 4662-4711.
30. Pandey, J., Biopolymers and Their Application in Wastewater Treatment. In *Emerging Eco-friendly Green Technologies for Wastewater Treatment*, Springer: 2020; pp 245-266.
31. Sinha Ray, S., 4 - Techniques for characterizing the structure and properties of polymer nanocomposites. In *Environmentally Friendly Polymer Nanocomposites*, Sinha Ray, S., Ed. Woodhead Publishing: 2013; pp 74-88.
32. S. Nair, S.; Mathew, A. P., Porous composite membranes based on cellulose acetate and cellulose nanocrystals via electrospinning and electrospraying. *Carbohydrate Polymers* **2017**, *175*, 149-157.
33. Pavia, D. L.; Lampman, G. M.; Kriz, G. S.; Vyvyan, J. A., *Introduction to spectroscopy*. Nelson Education: 2014.
34. Barron, P. M. V. R.; Andrew, R., *UV-Visible Spectroscopy*. 2020.



35. Mitsch, W. J., *Wetlands Fifth Edition*. 2015; Vol. 91, p 721-721.
36. Lugo, A. E.; González, O. M. R.; Pedraza, C. R., The Río Piedras Watershed and its Surrounding Environment. **2011**, (June), 46-46.
37. Safety, U. S. C.; Hazard Investigation, B., Caribbean Petroleum Tank Terminal Explosion and Multiple Tank fires. **2015**, 99-99.
38. Subramanian, R.; Ellis, A.; Torres-Delgado, E.; Tanzer, R.; Malings, C.; Rivera, F.; Morales, M.; Baumgardner, D.; Presto, A.; Mayol-Bracero, O. L., Air Quality in Puerto Rico in the Aftermath of Hurricane Maria: A Case Study on the Use of Lower Cost Air Quality Monitors. *ACS Earth and Space Chemistry* **2018**, 2 (11), 1179-1186.
39. Soto Hidalgo, K.; Cabrera, C. R. C. Core-Shell of Fe<sub>0</sub>/Fe<sub>x</sub>O<sub>y</sub> Nanoparticles and Avicennia Germinans for Phytonanoremediation of Cadmium, Lead, and Arsenic Metals in Wetland Soil and Reusability in Photoelectrochemical Solar Cells Applications. 2016.
40. Anku, W. W.; Mamo, M. A.; Govender, P. P., Phenolic Compounds in Water: Sources, Reactivity, Toxicity and Treatment Methods. In *Phenolic Compounds - Natural Sources, Importance and Applications*, Soto-Hernandez, M.; Palma-Tenango, M.; Garcia-Mateos, M. d. R., Eds. InTech: Rijeka, 2017; p Ch. 17.
41. Stevens, J. F.; Maier, C. S., The chemistry of gut microbial metabolism of polyphenols. *Phytochemistry Reviews* **2016**, 15 (3), 425-444.
42. Lee, B. P.; Messersmith, P. B.; Israelachvili, J. N.; Waite, J. H., Mussel-inspired adhesives and coatings. *Annual review of materials research* **2011**, 41, 99-132.
43. Zhang, H.; Zhao, T.; Newland, B.; Liu, W.; Wang, W.; Wang, W., Catechol functionalized hyperbranched polymers as biomedical materials. *Progress in Polymer Science* **2018**, 78, 47-55.
44. Đudarić, L.; Fužinac-Smojver, A.; Muhvić, D.; Giacometti, J., The role of polyphenols on bone metabolism in osteoporosis. *Food Research International* **2015**, 77, 290-298.
45. Lee, H.; Scherer, N. F.; Messersmith, P. B., Single-molecule mechanics of mussel adhesion. *Proceedings of the National Academy of Sciences* **2006**, 103 (35), 12999-13003.
46. Zhang, W.; Wang, R.; Sun, Z.; Zhu, X.; Zhao, Q.; Zhang, T.; Cholewinski, A.; Yang, F.; Zhao, B.; Pinnaratip, R.; Forooshani, P. K.; Lee, B. P., Catechol-functionalized hydrogels: biomimetic design, adhesion mechanism, and biomedical applications. *Chemical Society Reviews* **2020**, 49 (2), 433-464.
47. Ejima, H.; Richardson, J. J.; Liang, K.; Best, J. P.; van Koeverden, M. P.; Such, G. K.; Cui, J.; Caruso, F., One-Step Assembly of Coordination Complexes for Versatile Film and Particle Engineering. *Science* **2013**, 341 (6142), 154-157.
48. Wurm, F.; Rietzler, B.; Pham, T.; Bechtold, T., Multivalent Ions as Reactive Crosslinkers for Biopolymers-A Review. *Molecules* **2020**, 25 (8), 1840.
49. Leite, D.; Peres, G.; Silveira, N., Biopolymer-metal complexes: recent advances and applications. 2016.
50. Ulbricht, J.; Jordan, R.; Luxenhofer, R., On the biodegradability of polyethylene glycol, polypeptoids and poly(2-oxazoline)s. *Biomaterials* **2014**, 35 (17), 4848-4861.
51. Zhao, K.; Zhang, X.; Wei, J.; Li, J.; Zhou, X.; Liu, D.; Liu, Z.; Li, J., Calcium alginate hydrogel filtration membrane with excellent anti-fouling property and controlled separation performance. *Journal of Membrane Science* **2015**, 492, 536-546.
52. Petla, R. K.; Vivekanandhan, S.; Satyanarayana, N.; Mohanty, A.; Misra, M., Nanofibers: Effective Generation by Electrospinning and Their Applications. *Journal of nanoscience and nanotechnology* **2012**, 12, 1-25.

53. Łabowska, M. B.; Michalak, I.; Detyna, J., Methods of extraction, physicochemical properties of alginates and their applications in biomedical field—a review. *Open Chemistry* **2019**, *17* (1), 738-762.
54. Steenken, S.; Neta, P., Electron transfer rates and equilibria between substituted phenoxide ions and phenoxyl radicals. *Journal of Physical Chemistry* **1979**, *83* (9), 1134-1137.
55. Oxidative Stress in Cell Culture. <https://www.sigmaaldrich.com/life-science/cell-culture/learning-center/media-expert/oxidative-stress.html> (accessed April, 27).
56. Schweigert, N.; Zehnder, A. J.; Eggen, R. I., Chemical properties of catechols and their molecular modes of toxic action in cells, from microorganisms to mammals: minireview. *Environmental microbiology* **2001**, *3* (2), 81-91.
57. Krähenbühl, S., Mitochondria: important target for drug toxicity? *Journal of hepatology* **2001**, *34* (2), 334-336.
58. Lee, W.-C.; Guntur, A. R.; Long, F.; Rosen, C. J., Energy Metabolism of the Osteoblast: Implications for Osteoporosis. *Endocr Rev* **2017**, *38* (3), 255-266.
59. Terada, H., Uncouplers of oxidative phosphorylation. *Environmental health perspectives* **1990**, *87*, 213-218.
60. Borciani, G.; Montalbano, G.; Baldini, N.; Cerqueni, G.; Vitale-Brovarone, C.; Ciapetti, G., Co-culture systems of osteoblasts and osteoclasts: Simulating in vitro bone remodeling in regenerative approaches. *Acta Biomaterialia* **2020**, *108*, 22-45.
61. Andersen, T.; Auk-Emblem, P.; Dornish, M., 3D Cell Culture in Alginate Hydrogels. *Microarrays* **2015**, *4* (2), 133.
62. Brogini, N.; Tosatti, S.; Ferguson, S. J.; Schuler, M.; Textor, M.; Bornstein, M. M.; Bosshardt, D. D.; Buser, D., Evaluation of chemically modified SLA implants (modSLA) biofunctionalized with integrin (RGD)- and heparin (KRSR)-binding peptides. *Journal of Biomedical Materials Research Part A* **2012**, *100A* (3), 703-711.
63. Knight, C. G.; Morton, L. F.; Peachey, A. R.; Tuckwell, D. S.; Farndale, R. W.; Barnes, M. J., The Collagen-binding A-domains of Integrins  $\alpha 1\beta 1$  and  $\alpha 2\beta 1$  Recognize the Same Specific Amino Acid Sequence, GFOGER, in Native (Triple-helical) Collagens. *Journal of Biological Chemistry* **2000**, *275* (1), 35-40.
64. Luo, Z.; Yang, Y.; Deng, Y.; Sun, Y.; Yang, H.; Wei, S., Peptide-incorporated 3D porous alginate scaffolds with enhanced osteogenesis for bone tissue engineering. *Colloids and Surfaces B: Biointerfaces* **2016**, *143*, 243-251.
65. Zhou, X.; Feng, W.; Qiu, K.; Chen, L.; Wang, W.; Nie, W.; Mo, X.; He, C., BMP-2 Derived Peptide and Dexamethasone Incorporated Mesoporous Silica Nanoparticles for Enhanced Osteogenic Differentiation of Bone Mesenchymal Stem Cells. *ACS Applied Materials & Interfaces* **2015**, *7* (29), 15777-15789.
66. Mansoorifar, A.; Subbiah, R.; Balbinot, G. d. S.; Parthiban, S. P.; Bertassoni, L. E., Embedding cells within nanoscale, rapidly mineralizing hydrogels: A new paradigm to engineer cell-laden bone-like tissue. *Journal of Structural Biology* **2020**, *212* (3), 107636.
67. Przekora, A., The summary of the most important cell-biomaterial interactions that need to be considered during in vitro biocompatibility testing of bone scaffolds for tissue engineering applications. *Materials Science and Engineering: C* **2019**, *97*, 1036-1051.
68. Tunprapa, S.; Puangparn, T.; Weerasombut, M.; Jangchud, I.; Fakum, P.; Semongkhon, S.; Meechaisue, C.; Supaphol, P., Electrospun cellulose acetate fibers:

- effect of solvent system on morphology and fiber diameter. *Cellulose* **2007**, *14* (6), 563-575.
69. He, X., Optimization of Deacetylation Process for Regenerated Cellulose Hollow Fiber Membranes. *International Journal of Polymer Science* **2017**, *2017*, 8.
70. Tang, Z.; Li, X.; Tan, Y.; Fan, H.; Zhang, X., The material and biological characteristics of osteoinductive calcium phosphate ceramics. *Regenerative Biomaterials* **2017**, *5* (1), 43-59.
71. Wu, W.-H.; Thomas, P.; Hume, P.; Jin, J., Effective Conversion of Amide to Carboxylic Acid on Polymers of Intrinsic Microporosity (PIM-1) with Nitrous Acid. *Membranes* **2018**, *8* (2), 20.
72. Weiss, I. M.; Muth, C.; Drumm, R.; Kirchner, H. O. K., Thermal decomposition of the amino acids glycine, cysteine, aspartic acid, asparagine, glutamic acid, glutamine, arginine and histidine. *BMC biophysics* **2018**, *11*, 2.
73. Huang, H.-L.; Hsing, H.-W.; Lai, T.-C.; Chen, Y.-W.; Lee, T.-R.; Chan, H.-T.; Lyu, P.-C.; Wu, C.-L.; Lu, Y.-C.; Lin, S.-T.; Lin, C.-W.; Lai, C.-H.; Chang, H.-T.; Chou, H.-C.; Chan, H.-L., Trypsin-induced proteome alteration during cell subculture in mammalian cells. *Journal of Biomedical Science* **2010**, *17* (1), 36.
74. Zhang, L.; Webster, T., 17 - Nanotopography of biomaterials for controlling cancer cell function. In *Biomaterials for Cancer Therapeutics*, Park, K., Ed. Woodhead Publishing: 2013; pp 461-488e.
75. Chen, Q.; Zhang, D.; Zhang, W.; Zhang, H.; Zou, J.; Chen, M.; Li, J.; Yuan, Y.; Liu, R., Dual mechanism  $\beta$ -amino acid polymers promoting cell adhesion. *Nature Communications* **2021**, *12* (1), 562.
76. Hennessy, K. M.; Clem, W. C.; Phipps, M. C.; Sawyer, A. A.; Shaikh, F. M.; Bellis, S. L., The effect of RGD peptides on osseointegration of hydroxyapatite biomaterials. *Biomaterials* **2008**, *29* (21), 3075-3083.
77. Li, S.; Nih, L. R.; Bachman, H.; Fei, P.; Li, Y.; Nam, E.; Dimatteo, R.; Carmichael, S. T.; Barker, T. H.; Segura, T., Hydrogels with precisely controlled integrin activation dictate vascular patterning and permeability. *Nature Materials* **2017**, *16* (9), 953-961.
78. Gautschi, O. P.; Cadosch, D.; Zellweger, R.; Joesbury, K. A.; Filgueira, L., Apoptosis induction and reduced proliferation in human osteoblasts by rhBMP-2, -4 and -7. *Journal of musculoskeletal & neuronal interactions* **2009**, *9* (1), 53-60.
79. Saito, A.; Suzuki, Y.; Ogata, S.-i.; Ohtsuki, C.; Tanihara, M., Activation of osteoprogenitor cells by a novel synthetic peptide derived from the bone morphogenetic protein-2 knuckle epitope. *Biochimica et Biophysica Acta (BBA)-Proteins and Proteomics* **2003**, *1651* (1-2), 60-67.
80. Kechagia, J. Z.; Ivaska, J.; Roca-Cusachs, P., Integrins as biomechanical sensors of the microenvironment. *Nature Reviews Molecular Cell Biology* **2019**, *20* (8), 457-473.
81. Pouwels, J.; Nevo, J.; Pellinen, T.; Ylännä, J.; Ivaska, J., Negative regulators of integrin activity. *Journal of Cell Science* **2012**, *125* (14), 3271-3280.
82. Kadry, Y. A.; Calderwood, D. A., Chapter 22: Structural and signaling functions of integrins. *Biochimica et Biophysica Acta (BBA) - Biomembranes* **2020**, *1862* (5), 183206.
83. Bachmann, M.; Kukkurainen, S.; Hytönen, V. P.; Wehrle-Haller, B., Cell Adhesion by Integrins. *Physiological Reviews* **2019**, *99* (4), 1655-1699.

84. Teckchandani, A.; Toida, N.; Goodchild, J.; Henderson, C.; Watts, J.; Wollscheid, B.; Cooper, J. A., Quantitative proteomics identifies a Dab2/integrin module regulating cell migration. *Journal of Cell Biology* **2009**, *186* (1), 99-111.
85. Blair, H. C.; Larrouture, Q. C.; Li, Y.; Lin, H.; Beer-Stoltz, D.; Liu, L.; Tuan, R. S.; Robinson, L. J.; Schlesinger, P. H.; Nelson, D. J., Osteoblast Differentiation and Bone Matrix Formation In Vivo and In Vitro. *Tissue Eng Part B Rev* **2017**, *23* (3), 268-280.
86. Brånemark, P.-I., *A method for vital microscopy of mammalian bone marrow in situ*. CWK Gleerup: 1958.
87. Gratton, A.; Buford, B.; Goswami, T.; Kurten, D. G.; Suva, L., Failure modes of biomedical implants. *Journal of the Mechanical Behavior of Materials* **2002**, *13* (5-6), 297-314.
88. He, D.-H.; Wang, P.; Liu, P.; Liu, X.-K.; Ma, F.-C.; Zhao, J., HA coating fabricated by electrochemical deposition on modified Ti6Al4V alloy. *Surface and Coatings Technology* **2016**, *301*, 6-12.
89. Liu, H.; Peng, H.; Wu, Y.; Zhang, C.; Cai, Y.; Xu, G.; Li, Q.; Chen, X.; Ji, J.; Zhang, Y.; OuYang, H. W., The promotion of bone regeneration by nanofibrous hydroxyapatite/chitosan scaffolds by effects on integrin-BMP/Smad signaling pathway in BMSCs. *Biomaterials* **2013**, *34* (18), 4404-4417.
90. Amini, A. R.; Laurencin, C. T.; Nukavarapu, S. P., Bone Tissue Engineering: Recent Advances and Challenges. *Critical reviews in biomedical engineering* **2012**, *40* (5), 363-408.
91. Pramanik, N.; Mishra, D.; Banerjee, I.; Maiti, T. K.; Bhargava, P.; Pramanik, P., Chemical Synthesis, Characterization, and Biocompatibility Study of Hydroxyapatite/Chitosan Phosphate Nanocomposite for Bone Tissue Engineering Applications. *International Journal of Biomaterials* **2009**, *2009*, 8.
92. Hayes, C. W.; Conway, W. F., Calcium hydroxyapatite deposition disease. *Radiographics : a review publication of the Radiological Society of North America, Inc* **1990**, *10* (6), 1031-48.
93. Ea, H. K.; Liote, F., Advances in understanding calcium-containing crystal disease. *Current opinion in rheumatology* **2009**, *21* (2), 150-7.
94. Garcia, G. M.; McCord, G. C.; Kumar, R., Hydroxyapatite crystal deposition disease. *Seminars in musculoskeletal radiology* **2003**, *7* (3), 187-93.
95. Nguyen, C.; Lieberherr, M.; Bordat, C.; Velard, F.; Côme, D.; Lioté, F.; Ea, H. K., Intracellular calcium oscillations in articular chondrocytes induced by basic calcium phosphate crystals lead to cartilage degradation. *Osteoarthritis and Cartilage* **2012**, *20* (11), 1399-1408.
96. Facca, S.; Lahiri, D.; Fioretti, F.; Messadeq, N.; Mainard, D.; Benkirane-Jessel, N.; Agarwal, A., In Vivo Osseointegration of Nano-Designed Composite Coatings on Titanium Implants. *ACS Nano* **2011**, *5* (6), 4790-4799.
97. Hyland, L. L.; Taraban, M. B.; Hammouda, B.; Bruce Yu, Y., Mutually reinforced multicomponent polysaccharide networks. *Biopolymers* **2011**, *95* (12), 840-851.
98. Chao, S. C.; Wang, M. J.; Pai, N. S.; Yen, S. K., Preparation and characterization of gelatin-hydroxyapatite composite microspheres for hard tissue repair. *Materials science & engineering. C, Materials for biological applications* **2015**, *57*, 113-22.
99. Dufresne, A., Nanocellulose: a new ageless bionanomaterial. *Materials Today* **2013**, *16* (6), 220-227.

100. Monreal Romero, H. A.; Mora Ruacho, J.; Martínez Pérez, C. A.; García Casillas, P. E., Synthesis of Hydroxyapatite Nanoparticles in Presence of a Linear Polysaccharide. *Journal of Materials* **2013**, *2013*, 1-5.
101. Wang, T.; Dorner-Reisel, A.; Müller, E., Thermogravimetric and thermokinetic investigation of the dehydroxylation of a hydroxyapatite powder. *Journal of the European Ceramic Society* **2004**, *24* (4), 693-698.
102. Echeverria, C.; Almeida, P. L.; Feio, G.; Figueirinhas, J. L.; Godinho, M. H., A cellulosic liquid crystal pool for cellulose nanocrystals: Structure and molecular dynamics at high shear rates. *European Polymer Journal* **2015**, *72*, 72-81.
103. Tang, Y.; Shen, X.; Zhang, J.; Guo, D.; Kong, F.; Zhang, N., Extraction of cellulose nano-crystals from old corrugated container fiber using phosphoric acid and enzymatic hydrolysis followed by sonication. *Carbohydr Polym* **2015**, *125*, 360-6.
104. de Araujo Junior, A. M.; Braido, G.; Saska, S.; Barud, H. S.; Franchi, L. P.; Assuncao, R. M.; Scarel-Caminaga, R. M.; Capote, T. S.; Messaddeq, Y.; Ribeiro, S. J., Regenerated cellulose scaffolds: Preparation, characterization and toxicological evaluation. *Carbohydr Polym* **2016**, *136*, 892-8.
105. Macdonald, M. L.; Samuel, R. E.; Shah, N. J.; Padera, R. F.; Beben, Y. M.; Hammond, P. T., Tissue integration of growth factor-eluting layer-by-layer polyelectrolyte multilayer coated implants. *Biomaterials* **2011**, *32* (5), 1446-53.
106. Lu, Z.; Huangfu, C.; Wang, Y.; Ge, H.; Yao, Y.; Zou, P.; Wang, G.; He, H.; Rao, H., Kinetics and thermodynamics studies on the BMP-2 adsorption onto hydroxyapatite surface with different multi-morphological features. *Materials science & engineering. C, Materials for biological applications* **2015**, *52*, 251-8.
107. Ventura, M.; Boerman, O. C.; Franssen, G. M.; Bronkhorst, E.; Jansen, J. A.; Walboomers, X. F., Monitoring the biological effect of BMP-2 release on bone healing by PET/CT. *Journal of controlled release : official journal of the Controlled Release Society* **2014**, *183*, 138-44.
108. Kong, L.; Gao, Y.; Cao, W.; Gong, Y.; Zhao, N.; Zhang, X., Preparation and characterization of nano-hydroxyapatite/chitosan composite scaffolds. *Journal of Biomedical Materials Research Part A* **2005**, *75A* (2), 275-282.
109. Keselowsky, B. G.; Collard, D. M.; García, A. J., Surface chemistry modulates fibronectin conformation and directs integrin binding and specificity to control cell adhesion. *Journal of Biomedical Materials Research Part A* **2003**, *66A* (2), 247-259.